

Old Dominion University

ODU Digital Commons

Electrical & Computer Engineering Theses & Dissertations

Electrical & Computer Engineering

Spring 2021

Electrostatic Design and Characterization of a 200 keV Photogun and Wien Spin Rotator

Gabriel G. Palacios Serrano

Old Dominion University, lyx.anzahl@gmail.com

Follow this and additional works at: https://digitalcommons.odu.edu/ece_etds



Part of the [Computer Engineering Commons](#), [Electrical and Computer Engineering Commons](#), and the [Physics Commons](#)

Recommended Citation

Palacios Serrano, Gabriel G.. "Electrostatic Design and Characterization of a 200 keV Photogun and Wien Spin Rotator" (2021). Doctor of Philosophy (PhD), Dissertation, Electrical & Computer Engineering, Old Dominion University, DOI: 10.25777/mf9f-r453
https://digitalcommons.odu.edu/ece_etds/224

This Dissertation is brought to you for free and open access by the Electrical & Computer Engineering at ODU Digital Commons. It has been accepted for inclusion in Electrical & Computer Engineering Theses & Dissertations by an authorized administrator of ODU Digital Commons. For more information, please contact digitalcommons@odu.edu.

**ELECTROSTATIC DESIGN AND CHARACTERIZATION OF A 200 keV PHOTOGUN
AND WIEN SPIN ROTATOR**

by

Gabriel G. Palacios Serrano
B.S. August 2014, Universidad Autónoma Metropolitana, Mexico
M.S. May 2017, Old Dominion University

A Dissertation Submitted to the Faculty of
Old Dominion University in Partial Fulfillment of the
Requirements for the Degree of

DOCTOR OF PHILOSOPHY

ELECTRICAL AND COMPUTER ENGINEERING

OLD DOMINION UNIVERSITY
May 2021

Approved by:

Helmut Baumgart (Director)

Carlos Hernández (Member)

Linda Vahala (Member)

Mohammad Obeid (Member)

Gon Namkoong (Member)

ABSTRACT

ELECTROSTATIC DESIGN AND CHARACTERIZATION OF A 200 keV PHOTOGUN AND WIEN SPIN ROTATOR

Gabriel G. Palacios Serrano
Old Dominion University, 2021
Director: Dr. Helmut Baumgart

High-energy nuclear physics experiments at the Jefferson Lab Continuous Electron Beam Accelerator Facility (CEBAF) require high spin-polarization electron beams produced from strained super-lattice GaAs photocathodes activated to negative electron affinity in a high voltage photogun operating at 130 kV dc. A pair of Wien filter spin rotators in the injector provides precise control of the electron beam polarization at the end station target. An upgrade of the CEBAF injector to better support the upcoming Moller experiment requires increasing the electron beam energy to 200 keV, resulting in better transmission through injector apertures and improved photocathode lifetime. In addition, the energy increase is expected to reduce unwanted helicity correlated intensity and position systematics. These requirements led to the design of a shielding electrode described in this work, which minimizes the electric field at the triple-point junction and linearizes the potential along the insulator, thus reducing the risk of field emission induced insulator arcing. The Wien spin rotator design was modified for increasing the electric field from 1.6 to 2.7 MV/m and the magnetic field from 9.1 to 13 mT. The upgrades required detailed modeling in Solidworks, electrostatic simulations using CST, beam dynamics using GPT, device implementation, and in situ high voltage characterization of the world's first 200 keV polarized photoelectron gun and compatible Wien filter spin rotator.

Copyright, 2021, by Gabriel G. Palacios Serrano, All Rights Reserved.

ACKNOWLEDGMENTS

“It is in the knowledge of the genuine conditions of our life that we must draw our strength to live and our reason for acting.”

- Simone de Beauvoir

The only reason why I have been able to surmount any challenge life posed at me, is because my entire existence has been surrounded with love, support, and companionship. My work is especially dedicated to my beloved Mia. Thank you for sharing the pep of freshly-opened eyes with this old mind of mine. I hope to survive long enough to see you fulfill your wildest dreams, and I hope this work encourages you to keep looking for the light that only knowledge can bring to us earthly creatures. Remember: You can always count on me. Always.

My eternal gratitude to my mother, Hilda “Lili” Serrano Velazquez. I hope to reciprocate with my actions the love you have shown to me since my eyes saw the first light. Thank you for your patience, your understanding, and your teachings. Thank you for the freedom, and for helping me become a true human being.

I am deeply grateful to my grandmother, Judith “mamá Judith” Velazquez Rojas. You truly are the foundation of our family. You built it on strength, you taught us collectivity. You showed me that through commitment and hard work I could achieve whatever I wanted, you were so right.

My deep gratitude goes also to my uncle Rafael “Tito” Serrano Velazquez, for caring about me. Thank you for providing for our family. Thank you for your teachings, and for sharing your cosmogony. You truly convinced me that I could one day become a scientist.

My gratitude extends equally to all my family members: Heidi, Chiquis, Vic, Yosh, Rafo, Pish, Quet, Piwi, Chino, Carlitos, Karla, Yoshi, Ada, Ame, Bellis, Leo, Atzin, Ale, Dani, and Mike. Thank you all for the love and for the sisterhood. No words can express how grateful I am to all of you.

I have been lucky to have the opportunity to experience amazing human interactions along the path. I am profoundly grateful to Jaime Grabinsky, Salvador Arellano, Arturo Robledo, Alejandro Kunold, J. A. Roa Neri, Adrian Espíndola, Cesareo García, Felipe Monroy, and the late Jaime Cruz “Sam” Sampedro; my professors and mentors at the Universidad Autónoma Metropolitana – Azcapotzalco. Your teachings, mentorship, and your friendship allowed me to build the necessary abilities and courage to pursue my academic goals. It seems like yesterday when Sam pulled money out of his wallet for me to be able to go to my internship at Jefferson Lab. You believed in me guys. You believed in me Sam. This happened thanks to you, this is for you.

For the opportunity of following my dream to work in accelerator science, and for stoking the flame that lead me to fully commit to it, I extend my gratitude to Carlos Hernández García, Matt Poelker, and Helmut Baumgart. Thank you for pouring a never-ending stream of knowledge into my mind, for pushing me to do better, for patiently waiting for me to pick up the ball when I have dropped it, and thank you for making me feel like I am part of something bigger than ourselves. You guys are amazing human beings, and outstanding mentors. My gratitude extends to Jefferson Lab’s Injector group: Marcy, Phil, Joe, Bubba, John, Alicia, Fay, Jim, Steve, Yan, and Mamun. You and all Jefferson Lab personnel make work feel like a home,

This work would be incomplete without mentioning my friends, since life is only worth living when you share it. Galgany: love is too small a word. Thank you for standing by me when things get rough, and thank you for the years of conversations. You truly bring the light back to the darkest days. Vics, Sal, Junki, and Mark: we shared a battlefield, we surpassed the vicissitudes, we will always. Thanks for being there, *I gotchu fam*. Carlos, Scarlet, Sofa, Emilio, and Chucho: thank you for sharing the warmth of your household with me, you changed my life and I will never forget that, my heart goes to you. Grex, Chuka, Isma, Abraham, Dan, Luisa, Joe, Omar, Masato, Gabo, Yancy, Fredy, Anna, Annie, Yael, Christine, Arita, Picho, Sajini, Dilini, Nilanga, Chio, Max, Lula, Lauren, Alok, Héctor, Mariana, Gio, Esly, Herre, Alex, Eli, and whoever I am forgetting: even if our roads split along the way or we are far away, I have been lucky to share the path with all of you and you impacted my life. For that I am very grateful. Your friendship brings color to my life and renews my hope in mankind.

This work would not have been possible without the contribution of each and every person that goes unnoticed while allowing our institutions to function. I want to thank all the personnel at mi *alma mater* the Universidad Autónoma Metropolitana – Azcapotzalco, to the organizers of the Summer Internships Abroad contest of the Mexican Physical Society Division of Particles and Fields for opening the doors to Mexican Students allowing us to fulfill our dreams, to Old Dominion University, specially to Lisa Okun, Delgerjargal "Degi" Betcher, Kasie Reyes, and everyone at the Office of Visa and Immigration Service Advising for their outstanding job, to Jefferson Science Associates and Thomas Jefferson National Accelerator Facility for giving me the opportunity to contribute to the body of knowledge in a great work environment. My sincere gratitude to

the members of my doctoral committee: Dr. Helmut Baumgart, Dr. Carlos Hernández García, Dr. Linda Vahala, Dr. Mohammad Obeid, and Dr. Gon Namkoong for their time, effort and genuine concern in helping me achieve this milestone.

For all of those we left behind in the arduous road towards academic success, I will continue to fight for a world in which we all have equal opportunities.

TABLE OF CONTENTS

	Page
LIST OF TABLES	ix
LIST OF FIGURES	x
Chapter	
1. INTRODUCTION	1
1. 1 Photoelectron gun	1
1. 2 Wien filter	3
1. 3 Motivation.....	4
1. 4 Problem statement.....	5
1. 5 Photoelectron gun and Wien filter review	7
1. 6 Achievements.....	11
2. BACKGROUND AND RELATED WORK	14
2. 1 Photoelectron guns.....	14
2. 2 Wien filter	28
2. 3 Simulations in accelerator physics.....	32
3. METHODS AND RESULTS	35
3. 1 Proposed system.....	35
3. 2 Methodology	36
3. 3 Modelling and design.....	38
3. 4 Simulations	48
3. 5 Hardware implementation.....	89
3. 6 High voltage characterization	94
3. 7 Data processing and analysis	98
4. DISCUSSION AND FUTURE WORK.....	111
4. 1 Summary and conclusions	114
4. 2 Outlook and future work.....	115
4. 3 Publications.....	116
REFERENCES	118
VITA.....	139

LIST OF TABLES

Table	Page
1: Trajectory deviation factor at first beam position monitor	74
2 : Trajectory deviation factor at second beam position monitor	74
3: Electric and magnetic field magnitudes needed for $\pi/2$ + 10% maximum spin rotation for the present injector energy (130 keV) and for the upgrade injector energy (200 keV)	84
4: Voltage per plate values corresponding to each inter-plate gap distance, calculated using the theoretical framework described in Appendix A. 4	86

LIST OF FIGURES

Figure	Page
1. Longitudinal cross-section of the current CEBAF photogun with un-doped ceramic insulator. Vacuum chamber with (A) anode structure, (B) tapered ceramic insulators with (C) cathode electrode attached. HV conductor surrounded with (D) vulcanized rubber, (E) grounded non-evaporable getter vacuum pumps.....	9
2. Longitudinal cross-section of the CEBAF 130 keV Wien filter with (A) vacuum chamber, (B) electrode plates, (C) mounting insulators, (D) magnetic shield, (E) spring guide, (F) HV feedthrough, and (G) magnetic end plates.....	10
3. Schematic diagram of the first photoelectron gun [1].	14
4. High intensity polarized electron source for SLAC [10].....	17
5. The MIT-Bates gun chamber [2].	18
6. Johannes Gutenberg Universitaet Mainz polarized electron source [3].	20
7. First (left) and second (right) CEBAF polarized electron sources [5].....	23
8. First inverted insulator photoelectron gun design for CEBAF [6].	26
9. MAMI accelerator Wien filter cross section [15].	31
10. Workflow methodology for electrostatic device development.....	38
11. Longitudinal cross section of the existing CEBAF -130 kV photoelectron gun. The inset shows an outline close-up of one of the proposed electrostatic shield modifications.	43
12. Longitudinal cross section of the cathode electrode shapes. The existing CEBAF photogun t-cathode (left), the first iteration shield (center), and the second iteration shield (right). Dimensions shown in inches.....	44
13. Proposed 40 kV rated HV feedthrough with 2 ¾ flange (left), proposed MACOR long mounting insulator (middle), proposed HV spring guide contact compatible with new feedthrough (right).....	47

14. Longitudinal cross section false color plot of CEBAF existing -130 kV photoelectron gun. The insets show close-up to the bottom and top triple points..... 51

15. False-color lateral cross-section views of the electrostatic field strength within two photoguns: (top) the present day CEBAF photogun with un-doped alumina insulator, and (bottom), the new photogun that includes a triple-point-junction shield electrode and doped alumina insulator. Potential (left) and electric field maps (right) are for both photoguns biased at -200 kV. The white arrows are proportional to the electric field normal to the equipotential lines. Horizontal axis scale in meters. The color scale corresponds to the potential in V (left) and electric field norm in MV/m (right). 52

16. (Top) Electric field strength and, (bottom) the potential along the rubber plug-ceramic insulator interface for two photoguns: (blue) the present day CEBAF photogun with un-doped alumina insulator, and (red) the new photogun that includes a triple-point-junction shield electrode and doped alumina insulator. Both photoguns biased at -200 kV. The dotted gray lines represent positions along the insulator (see inset)..... 54

17. False-color lateral cross-section views of the electrostatic field strength within three photoguns biased at -200 kV: (left) the present day CEBAF photogun with un-doped alumina insulator, (middle) the first iteration photogun that includes a triple-point-junction shield electrode and doped alumina insulator, and (right) second iteration photogun with smaller triple-point junction shield. The color scale corresponds to the electric field norm in V/m..... 55

18. Transverse electric field within the cathode-anode gap, along the centerline of the photogun as shown by the red line in the inset detail. Orange, blue and gray data points correspond to original, first iteration, and second iteration photogun designs respectively. All produced with -200 kV bias voltage..... 57

19. Lateral cross-section of the present 130 keV CEBAF (top) and proposed 200 keV upgrade (bottom) Wien filter models in Solidworks. 58

20. False color plot of electric field magnitude on a lateral cross section of the feedthrough-nipple gap for the present 130 keV CEBAF (left) and proposed 200 keV upgrade (right) Wien filters..... 60

21. CAD of the proposed HV spring guide with adapted dimensions to match the proposed 40 kV feedthrough. 61

22. False color of electric field magnitude of a lateral cross section focusing on Rogowski profile tip for the present 130 keV CEBAF (top) and proposed 200 keV upgrade (bottom) Wien filters..... 61

23. Simulated trajectories of electrons emitted from the mounting tab cusp, Rogowski profile tip, plate strong back rib, and electrode bottom surface. Color gradient corresponds to energy in eV. The electrode plates are biased at ± 20 kV respectively. 63
24. False color surface electric field of the mounting setup, showing the mounting spring-insulator-mounting tab assembly (left side), and the same assembly with transparent mounting spring and insulators. The results show all metal (top), insulator and metal (middle), and all insulating (bottom) fixing material simulation results. The electrode plates are biased at ± 20 kV respectively. 64
25. Lateral view of mounting tab showing dimensions (left). False color surface electric field isometric view of mounting tab (right side) with original (top) and double thickness (bottom). The electrode plates are biased at ± 20 kV respectively. 66
26. Lateral view of mounting tab showing dimensions (left). False color surface electric field isometric view of mounting tab (right side). 67
27. False color electric field plot showing a lateral view of HV electrode plates, insulators and HV spring guides. The electrode plates are biased at ± 20 kV respectively. 68
28. Location of the first and second beam position monitors used in the simulation. The inset shows an example of electron launch positions along the vertical axis on the photocathode surface. 72
29. Simulated position of individual electrons on the first (top) and second (bottom) beam position monitors (BPMs). The color code corresponds to each launch position on the vertical axis of the photocathode surface, being $y=2$ mm (orange), 0 mm (gray), -2 mm (yellow), and -4 mm (blue). 73
30. Simulated trajectories of individual electrons from three launch locations along the vertical axis on the photocathode surface: (left) $y=-2$ mm, (middle) $y=0$, and (right) $y=2$ mm. The color code corresponds to the (orange) existing CEBAF T-cathode, (gray) First iteration, and (blue) second iteration of shielded cathodes. 75
31. Transverse vertical average beam position results of beam dynamics simulations. The color code corresponds to existing T-cathode (orange), first iteration model (gray), and second iteration (blue). 77
32. Beam dynamics simulation results of normalized transverse emittance (top) and spot size growth (bottom). The color code corresponds to the (orange) existing CEBAF T-cathode, (gray) First iteration, and (green) second iteration of shielded cathodes. 78

33. Transverse vertical (top) and longitudinal (bottom) electrostatic forces. 79
34. Vertical position readings at a simulated BPM at 39.5 cm from the photocathode face for the existing CEBAF (orange) and second iteration (blue) models. 80
35. Simulated electric (blue) and magnetic (red) fields. The theoretical values of the electric field result in an asymmetric total force (purple), while reducing the electric field restores its symmetry (green). All plots are normalized to their maximum values. ... 82
36. Beam dynamics GPT results for the 130 keV CEBAF (orange) and 200 keV upgrade (blue). Based on the great digest shown in [4]. 85
37. Beam dynamics GPT results for the 200 keV proposed upgrade for 15 mm (blue), 13 mm (yellow), and 11 mm (green) gaps. Based on the digest shown in [3]. 88
38. Beam dynamics GPT results for the 200 keV proposed upgrade for symmetric bias (orange), and asymmetric bias (blue). Based on the digest shown in [3]. 89
39. -200 kV photoelectron gun cathode electrodes with electrostatic shield. The first iteration (top left), second iteration (top right), and 200 keV Wien filter (bottom). .. 92
40. Example of HV characterization of cathode electrode (top) and Wien filter (bottom) showing raw epics monitor. On the top figure the relevant signals are the first and second trace show the cathode bias voltage and the power supply current draw. The third to seventh traces show radiation monitor response On the bottom figure the relevant traces are the first and second showing the bias voltage applied to the electrode plates, the third and fourth showing ion pump current response, and the fifth and sixth showing radiation monitor response. 97
41. High voltage conditioning history of CEBAF 130 kV T-cathode electrode showing bias voltage (blue), and the signal from one of the Geiger-Müller x-ray monitors near the photogun (green). 100
42. High voltage conditioning history of the second iteration electrode with triple-point-junction shield showing bias voltage (blue), and the signal from one of the Geiger-Müller x-ray monitors near the photogun (green). 101
43. Example of a HV characterization of the Wien filter vacuum response as a function of applied voltage at both electrode plates at unison. 103
44. Wien filter HV characterization after device re-assembly. As each plate is energized by keeping the opposite plate at ground (left), and as both electrode plates are biased together (right), the device presents practically no vacuum degradation. 103

45. Beam position readings from a BPM located at 90.74 cm from the photocathode surface as a function of magnetic field strength. 105
46. Vertical position on a BPM as a function of beam source position on the photocathode. The t-cathode simulated (orange trace) and raw experimental data (red trace), and the second iteration simulated (turquoise) and raw experimental data (blue trace) are shown. 106
47. Vertical position on a BPM as a function of beam source position on the photocathode for the t-cathode. Simulated original (orange), 1.5 mm emission location offset (green), 3 mm emission location offset (black), matched offset experimental (red) and raw experimental data (blue) are shown. 108
48. Vertical position on a BPM as a function of beam source position on the photocathode for the second iteration cathode. Simulated original (orange), 1.5 mm emission location offset (green), 3 mm emission location offset (black), matched offset experimental (red) and raw experimental data (blue) are shown. 109

CHAPTER 1

INTRODUCTION

The interest of the scientific community on the study of the spin structure in nucleons and asymmetry in particle scattering processes prompted a worldwide collaboration to create a device capable of producing a high-quality beam of spin-polarized electrons.

1. 1 Photoelectron gun

Beginning in 1970 in Yale University for the Stanford Linear Accelerator Center (SLAC) [1], the first device of this type, referred to as a “photoelectron gun”, was developed. The substitution of the electron source in a thermionic gun by a III-V GaAs semiconductor crystal mounted on a biased cathode, allowed the production of a beam of longitudinally polarized electrons when illuminated with circularly polarized light in ultra-high vacuum conditions. The success of SLAC’s design motivated the accelerator community from Massachusetts Institute of Technology (MIT) Bates [2], the Mainz Racetrack Microtron (MAMI) [3], the Superconducting Darmstadt Linear Accelerator (S-DALINAC) [4], and Jefferson Laboratories’ Continuous Electron Beam Accelerator Facility (CEBAF) [5] to build upon the design, successfully fulfilling the strict operation and beam quality parameters of the experimental programs of the following decades.

As the initial section of an accelerator, photoelectron gun construction requires the use of sophisticated design, manufacturing and assembling techniques aimed to generate keV-level beam energy necessary to satisfy the requirements in beam quality and to extend the operation lifetime of the photocathode crystal. Multiple gun designs have been

developed and tested by international collaborations based on the experimental findings of each photoelectron source generation. The state-of-the-art photoelectron gun [6] is based on an “inverted” design, where high voltage (HV) is fed by a short hollow conical insulator that extends into the ultra-high vacuum vessel and acts as a mechanical holding structure for a cathode electrode. The metallic cathode is hollow with internal components that secure a GaAs semiconductor crystal mounted on a cylindrical puck behind the electrode aperture. The puck additionally permits the manipulation of the photocathode in a preparation vacuum chamber connected to the high voltage vessel with a gate valve. The GaAs semiconductor crystal is heat-cleaned in the preparation chamber and negative electron affinity activated by depositing cesium (Cs) and an oxidizer on its surface. The later implementation of strained lattice GaAs photocathodes allowed successful production of higher polarization electron beam compared to bulk GaAs, nevertheless the sensitivity of these novel materials to degradation of vacuum conditions and subsequent loss of electron yield impose even more stringent requirements on modern day photoelectron sources. It has been demonstrated [7] that electrons emitted from the biased metallic cathode surface through the process known as “field emission”, degrade vacuum by desorbing gas from the high voltage vacuum chamber walls. Additionally, field emission near the insulator-metal-vacuum interface “triple-point” is also related to arcing and insulator failure, which can lead to complete loss of photocathode electron yield (also referred to as quantum efficiency or QE). Moreover, it has been observed that in the presence of residual gas in the cathode-anode gap region the electron beam can create ions through scattering, which having a positive charge are then accelerated towards the photocathode surface, further degrading QE by desorbing the surface cesium layer [8].

Therefore, advances in cathode design that reduce the likelihood of arcing and field emission, thus preventing vacuum degradation and subsequent photocathode lifetime loss, are highly valuable for the accelerator community, enabling the fulfillment of existing and future nuclear experiment programs.

1. 2 Wien filter

Since Wilhelm Wien invented the device that carries his name in 1898, its simple design yet robust working principle has allowed researchers to utilize it in a variety of experiments, from its initial use for measuring particle charge-mass ratio to electron microscopy as monochromator and energy analyzer [9]. The Wien filter finds applications in accelerator physics as a spin angle rotator. Initially implemented at SLAC [10], the benefits from its compact design were subsequently reproduced and improved in MIT-Bates [2], CEBAF [11], MAMI [12], and S-DALINAC [4].

Its working principle relies on the interaction of charged particles with independently generated homogeneous electric and magnetic static fields in an ultra-high vacuum chamber. An electron traveling with a velocity vector perpendicular to mutually orthogonal electric and magnetic fields has its spin vector angle rotated proportionally to the field magnitudes [13]. Moreover, if those magnitudes fulfill the so-called “Wien condition”, where the forces exerted by the fields are in equilibrium, the incoming particle trajectory would remain unchanged upon exiting. These characteristics made the Wien filter an excellent candidate for its implementation along with photoelectron guns to control the spin of high polarization electron beams for nuclear physics experiments at laboratories around the world.

To be used as a spin rotator, the operation and construction parameters of the Wien filter must be tailored to the energy of the electron beam that traverses it. Therefore, any subsequent increase in beam energy requires modifications to the design to ensure proper operation. Geometrical constraints in parallel-plate Wien filters where the electric field is generated inside a vacuum chamber surrounded by magnetic field generating coils lead to violation of the Wien condition at the fringe region [12], where the contributions to the total electromagnetic force would lead to undesired deviations in the beam trajectory. These deviations have been reported to be present in existing 100 keV compatible Wien filters [12], [4]. Although at those parameters the deviation has been simple to manage, the increasing energy requirements of existing and future experiments would greatly benefit from a detailed description of beam dynamics (trajectory, energy, beam size) of the electron assemble as it traverses the device.

1. 3 Motivation

The Jefferson Lab Continuous Electron Beam Accelerator Facility utilizes a 130 keV polarized photoelectron source with compatible spin rotator to provide a polarized electron beam for nuclear physics experiments and has been in operation since 2010. As part of the recently conducted accelerator energy upgrade program, the Moller experiment requires reductions of the injector beam's systematic errors (intensity, position, spot size) in addition to 1% level control of beam polarization, leading to a requirement of 75 μ A current with 80% polarization beam [21]. The increase in current leads to an exacerbation in beam space charge effects, leading to emittance dilution that in turn can result in beam loss, resulting in an increase in systematics. To mitigate these effects, and meet the

stringent specifications, the injector upgrade requires increasing the generated beam energy to 200 keV. Such energy increase requires operating the electron beam source at 53.8% higher bias, which results in cathode regions with an undesirably high electric field. This often leads to field emission degrading the ultra-high vacuum environment required by the delicate strained-super lattice GaAs photocathode resulting in poor lifetime, severely affecting the precious amount of beam time available for the physics users' program. Electric fields in excess of 10 MV/m at the triple point (where the insulator joins with the metal cathode and the vacuum environment) often lead to catastrophic insulator surface flashover [23] delaying the experimental physics program by weeks. It is therefore imperative for the upgrade photoelectron source to operate reliably and without field emission at the higher bias voltage. Similarly, the Wien filter requires 62.9% higher bias and 42.8% stronger magnetic field to provide 100° spin rotation in the 200keV electron beam. An implementation of an electrostatic shield was originally designed using 2-dimensional simulations tools and tested as the means to linearize the potential across the insulator on a spherical cathode photoelectron gun with inverted geometry, designed to reduce the likelihood of arcing during insulator experimental tests [16]. The results yielded by that study kindled interest in the development of electrostatically shielded cathode electrodes for these types of photoguns and identified the need for in-depth research and development efforts to implement them in future photoelectron sources.

1. 4 Problem statement

The necessary electron beam current imposed by the upcoming Moller experiment and the associated technical and scientific challenges regarding space charge phenomena

leading to emittance dilution and subsequent increase in systematics, require an increase to the energy of the electron beam produced by the photoelectron gun at the accelerator injector section. The energy rise, and thus bias voltage operation of the photogun, could lead to field emission from sites on the cathode electrode that are subjected to high electric fields, resulting in arcing and vacuum deterioration that significantly reduce photocathode lifetime and can even result in catastrophic device failure. Therefore, in order to enable the existing CEBAF 130 kV photoelectron gun to increase its operational capabilities, the objective of this work is to address these scientific and engineering challenges facing the CEBAF upgrade and the planned Moller Experiment by demonstrating solutions for two required accelerator physics electrostatic devices specifically.

The goal is to devise, implement and demonstrate solutions to two accelerator physics electrostatic devices:

1. A -200 kV bias voltage photoelectron gun cathode electrode with electrostatic shield compatible with the current CEBAF -130kV inverted gun design considering the following constraints:
 - Maximum surface gradient $<10\text{MV/m}$ to reduce risk of field emission.
 - Limit changes to electrode shape for:
 - Minimizing impact on delivered electron beam quality,
 - Minimizing additional surface area to preserve ultra-high vacuum environment,
 - Minimizing additional weight to maintain mechanical stability of the insulator-electrode assembly.

2. A 200 keV energy compatible Wien filter spin rotator capable of 100° spin rotation based on the existing 130 keV existing design with the following constraints:

- Maximum surface gradient <10MV/m to reduce the risk of field emission.
- Limit changes to the original design for:
 - Minimizing changes to electric field profile,
 - Minimizing impact on electron beam quality,
 - Maintaining a 15 mm electrode gap.

1. 5 Photoelectron gun and Wien filter review

A cross section view of a 3D model of the existing CEBAF photoelectron gun is shown in Figure 1. The photogun is based on an inverted insulator design, consisting of a cylindrical stainless steel vacuum chamber (35.6 cm diameter) with a flat front plate that accommodates the anode structure and a dish-head back plate. The top ConFlat® flange (25.4 cm diameter) supports the insulator and cathode electrode. The hollow interior of the ceramic insulator is tapered to accommodate a commercial high voltage connector commonly known as R28 in the X-Ray high voltage industry, consisting of an inner conductor surrounded by vulcanized rubber. Photocathodes attached to molybdenum pucks are held in place within the cathode electrode using sapphire rollers attached to leaf springs, which press the photocathode surface against a Pierce focusing electrode (25-degree angle). Photocathode pucks can be removed and inserted using a magnetic sample manipulator (not shown in Figure 1). There are Kovar™ rings brazed to each end of the

insulator. At the ground open end, the Kovar™ ring is welded to the 25.4 cm ConFlat® flange. At the high voltage closed narrow end, the collar is brazed to a short molybdenum cylinder, to which the cathode electrode is bolted.

The photogun has an array of non-evaporable getter (NEG) cartridges (SAES WP-1250-ST707) that line the bottom of the vacuum chamber. The entire inner surface of the vacuum chamber was NEG coated with an in-house plasma-sputtering process. A grounded wire mesh (not shown in the simulation) placed just above the NEG cartridges defines the ground plane and helps to prevent the charging of particulate matter that NEG pumps often produce.

The lower voltage -130 kV CEBAF photogun employs an un-doped insulator composed of 97.7% alumina. It is 12.9 cm long with an outer diameter tapering from 6.9 to 4.9 cm. The insulator for the higher voltage -200 kV photogun has slightly different dimensions at the Kovar™ braze joints, in part to accommodate the addition of the electrostatic triple-point-junction shield. This insulator is 94.4% alumina and doped with a vendor-proprietary substance that serves to reduce the insulator bulk resistivity to drain away accumulated charge that might accrue on the insulator, for example, as a result of field emission, or ion bombardment [29].

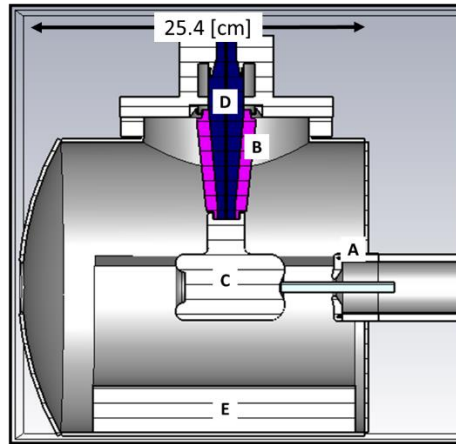


Figure 1: Longitudinal cross-section of the current CEBAF photogun with undoped ceramic insulator. Vacuum chamber with (A) anode structure, (B) tapered ceramic insulators with (C) cathode electrode attached. HV conductor surrounded with (D) vulcanized rubber, (E) grounded non-evaporable getter vacuum pumps.

The present CEBAF Wien filter designed to be compatible with a 130 keV beam energy is based on the original SLAC design and later adapted by MIT/Bates, S-DALINAC and MAMI accelerators. Mutually orthogonal homogeneous electric and magnetic fields are induced inside an ultra-high vacuum chamber to manipulate the spin polarization angle of the electrons that traverse the device longitudinally, with a velocity vector that is orthogonal to the applied fields. As shown in the longitudinal cross section 3D model in Figure 2, it consists of two stainless steel electrode plates with a Rogowski profile based on SLAC's design but modified to match as best as possible the magnetic field profile particular to the CEBAF 130 keV Wien. The electrodes are held in place inside a rectangular profile vacuum chamber maintaining a 1.5 cm gap along their length with +/- 0.01 cm tolerance by means of four MACOR insulator standoffs that couple to mounting tabs on the electrode's end and to a semi-flexible nickel alloy frame on the opposite (ground potential) end. The frame is secured to the body of the vacuum chamber with silver-plated

bolts. Inside the vacuum chamber, each electrode is connected with a spring and guide to high voltage feedthroughs mounted on 6.985 cm (2- $\frac{3}{4}$ in) ConFlat flanges (SHV-20 by Kurt J. Lesker). High voltage is applied via cables from a 15 kV dual polarity direct current (DC) power supply.

To produce $90^\circ + 10\%$ spin rotation angle with 1.5 cm electrode gap, orthogonal field magnitudes of $B = 9.1$ mT and $E = 1.6$ MV/m are required along the beam path. The electric field is produced by applying +12.4 kV to one of the electrodes and -12.4 kV to the opposite electrode. The corresponding magnetic field profile is defined by the coil characteristics, in addition to the steel yokes and nickel magnetic mirror endplates that comprise the magnetic shield surrounding the vacuum chamber, and it is induced by applying a current of 14.8 A to a set of window frame coils located between the vacuum chamber and the magnetic shield.

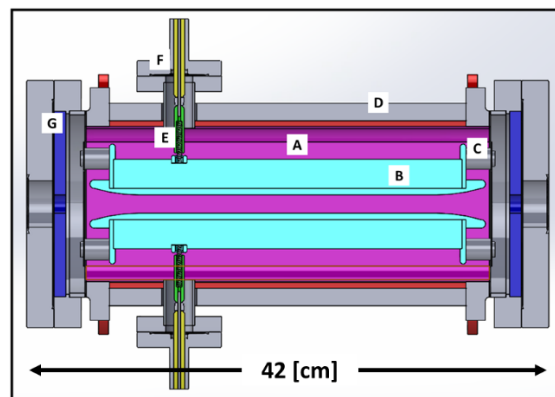


Figure 2: Longitudinal cross-section of the CEBAF 130 keV Wien filter with (A) vacuum chamber, (B) electrode plates, (C) mounting insulators, (D) magnetic shield, (E) spring guide, (F) HV feedthrough, and (G) magnetic end plates.

1. 6 Achievements

A cathode electrode with unique electrostatic shield for robust operation at the required -200kV bias voltage and an energy compatible Wien filter with the highest known operating voltage capable of rotating the spin by 100° were developed as a result of this work. The subsequent implementation and high voltage characterization of the photoelectron gun in an experimental test bed at Jefferson Laboratory enabled production of 200 keV polarized electron beam for a nuclear physics test of a solid hydrogen target (HDIce) in more than 500 cumulative hours, making it the highest voltage polarized source known to deliver production beam. The combined use of the devices is hypothesized to provide lower beam emittance, improved transmission through injector apertures, and improved photocathode lifetime, with 1% level of control on the spin polarization angle. The results presented in this work including the characterization of the beam trajectory deviations to validate electrostatics and beam dynamics simulations, along with the developed work methodology, are expected to provide valuable information to the accelerator physics community necessary for the development of higher energy photoelectron sources and spin rotators for future nuclear physics programs such as the Electron Ion Collider (EIC) [18] and the International Linear Collider (ILC) [17]. More specifically, this work aims to contribute in three aspects explained in the following sections.

1.6.1 Beam deflection-cathode geometry correlation

The first contribution to the body of knowledge resulting from this project is demonstrating a correlation between the geometry of the triple point shielding the electrode

and the beam deflection along the anode-cathode gap. This correlation motivates future work and research to conduct an optimization study for arriving at the best electrode shape (within a set of constraints described below) to minimize electron beam deflection and provide the highest operating voltage without field emission and without insulator arcing.

1.6.2 Framework for Cathode development

A second contribution, in particular for the design of future photoelectron guns at Jefferson Lab, is the development of a methodology used to devise a new single piece cathode electrode design that includes a carefully engineered electrostatic shield to allow for operation at -200 kV bias adhering to three main principles: no field emission to ensure long photocathode lifetime, optimal shape for minimizing beam deflection across the anode-cathode gap, and robust operation without electrical breakdown. The methodology developed in this work includes creating 3D models from manufacturing drawings as the backbone for electrostatic simulations; optimization of the 3D models consisting in an iterative process guided by the results of the simulations based on the principles described above was developed. Prototype manufacture with the aid of designer updated drawings was mechanically polished to a mirror-like surface finish and tested under high-vacuum conditions for high voltage performance qualification in terms of robustness (no arcing along the insulator) and no measurable field emission at -200 kV. Additionally, an extensive beam dynamics simulation phase is used to study beam deflection across the anode-cathode gap as a function of electrode shape. Lastly, the effect of the electrode shape on beam trajectory was evaluated by surveying the beam trajectory deviation without using beam line optics elements.

1.6.3 Framework for Wien filter upgrade

The third contribution from this work consists of developing and implementing a methodology to upgrade the CEBAF Wien filter design for the required higher beam energy. The methodology describes tasks such as electrostatic simulations, testing under vacuum conditions to qualify higher voltage performance, and simulations to understand the beam dynamics resulting from the electron interaction with the static electric and magnetic fields as it traversed the Wien filter for qualifying beam transport. Additionally, the dynamics that lead to trajectory deviations correlated to electromagnetic fields mismatch at the fringe regions and are described in this methodology

CHAPTER 2

BACKGROUND AND RELATED WORK

2.1 Photoelectron guns

Electron sources have been historically used in laboratories around the world to perform nuclear physics experiments [5]. The interest in studying spin-dependent physical properties of nuclei and asymmetry in scattering processes motivated the construction of the first photoelectron gun in the 1970s. It was created at Yale University to be used at Stanford Linear Accelerator Center (SLAC) to test the spin structure of protons [1], as shown in Figure 3.

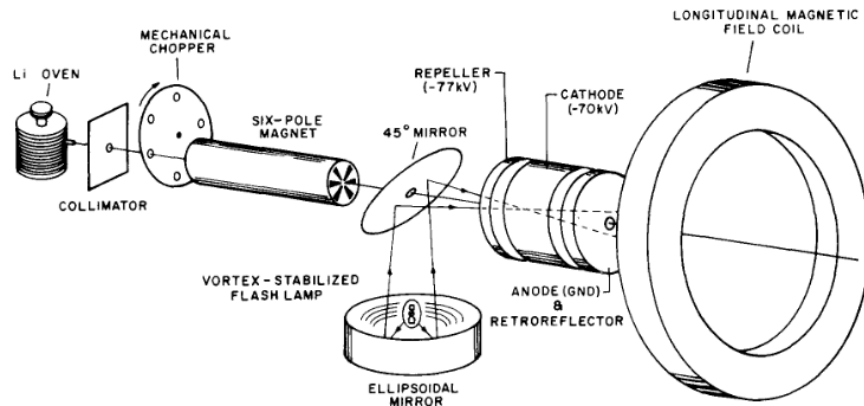


Figure 3: Schematic diagram of the first photoelectron gun [1].

Several techniques were investigated to produce electron sources with a long life time, which is the time it takes for electron yield to decay to $1/e$ of its initial value, high polarization, and high current. The most prevalent sources produce photoemission of longitudinally polarized electrons from III-V gallium arsenide (GaAs) photocathodes. The

electrons are produced by illuminating the surface of the photocathode using circularly polarized laser light with a wavelength of 780 nm, slightly over the semiconductor band gap. To produce a large number of electrons per incident photons (electron yield or quantum efficiency) from the semiconductor photocathode, its surface is subjected to an activation to negative electron affinity [10] by high temperature cleaning followed by intermittent vapor deposition of cesium (Cs) and nitrous tri-fluoride (NF₃) as an oxidant. The resultant monolayer produces a dipole field that bends the conduction and valence band and lowers the vacuum energy level below the conduction band, creating the conditions for increased electron yield. The work function is the minimum energy needed to remove an electron from a solid material to a point immediately outside the solid surface or, in other words, the energy needed to move an electron from the Fermi energy level into vacuum. The electron affinity is the energy difference between the GaAs semiconductor conduction band edge and the vacuum level.

SLAC's first source was developed in 1976 [10], and it was later used at other research institutions as a working template for GaAs photoelectron sources (Figure 4). It was based on an existing thermionic gun design that used a large bore ribbed insulator, with a concentric cathode stalk mounted on the inside to hold molybdenum pucks used as holders for the semiconductor crystal. To produce the beam characteristics required by SLAC's experimental program, the GaAs photocathode was mounted in substitution of the thermionic tip, allowing the gun to produce much higher polarization beam than that from thermionic sources when illuminated by a near band-gap laser light with the cathode biased at -120 kV. Even though the design had a separated load-locked deposition chamber where the semiconductor surface was activated to negative electron affinity, the design's original

operation bias of -150 kV had to be lowered due to insulator flashover and field emission from the metal cathode surface. This was related to the presence of Cs in the gun chamber, used to replenish electron yield and extend photocathode lifetime which suffered degradation between beam production operations. Additionally, the design required a sulfur hexafluoride (SF₆) tank enclosing the gun large bore insulator and connection to the high voltage power supply to prevent corona discharges. Even though the gun was successfully operated for years achieving never before seen polarization [10], the increasing high current and higher polarization requirements for increased statistics and higher resolution for nuclear physics experiments motivated groups around the world to improve on SLAC's design.

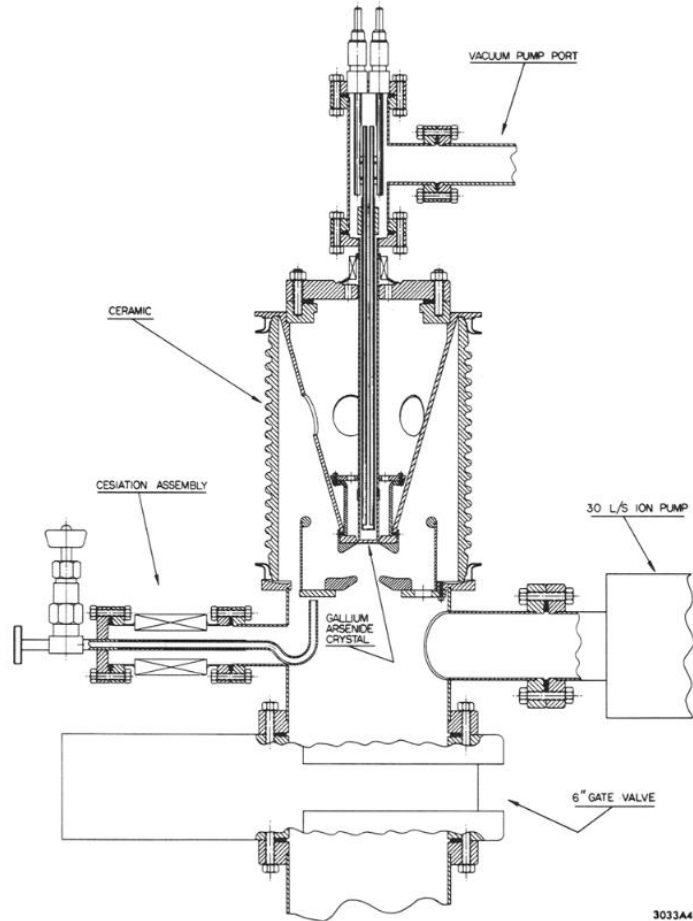


Figure 4: High intensity polarized electron source for SLAC [10].

The Massachusetts Institute of Technology (MIT) developed a similar photoelectron source for the Bates Linear accelerator center, publishing its findings in 1989 [2]. Developed also by Yale University and based on SLAC's thermionic gun design, it used a Faraday cage surrounding a -300 kV accelerator column that naturally required an SF6 environment to prevent arcing. The design included a separate deposition chamber with capacity for 4 puck holders for the GaAs photocathodes. The gun also functioned as a holder for one of the photocathodes, while another one was activated to negative electron

affinity inside the adjacent load-locked deposition chamber. It also included a cesium dispenser in the gun vacuum chamber, used to extend cathode lifetime. Since field emission current is inversely proportional to the emitter work function [14], the drawback of this design is that cesium was unintentionally sprayed on the gun electrodes leading to field emission, as Cs has a work function of 2.1 eV compared to 4.5 eV from stainless steel (electrode material). The Bates source was successfully operated and satisfied the necessities of MIT's research program, yet the team recognized that the accelerating gap needed to be shorter to manage space charge effects that affected beam quality and recognized the complexity of some of the inherent design characteristics [2].

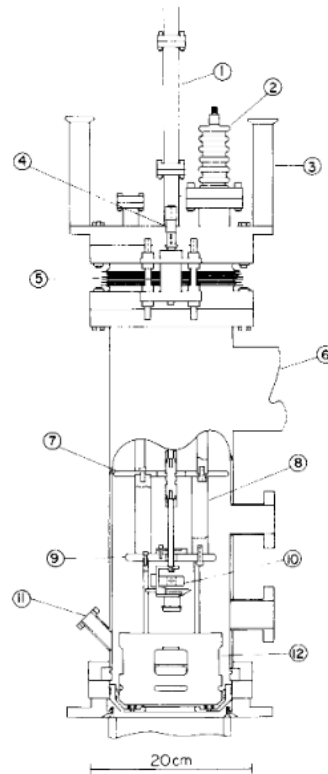


Figure 5: The MIT-Bates gun chamber [2].

In 1990 at the Johannes Gutenberg Universitaet in Mainz, Germany, the Mainz racetrack microtron cascade (MAMI) project followed SLAC's design for their own nuclear physics and parity-violation experiments [3]. In order to prevent previously reported deterioration of the photocathode negative electron affinity, it was proposed using a modest -100kV bias voltage in combination with a modification in the laser characteristics to produce rectangular current pulses to prevent energy variation contributions to systematic errors. It used the same design as SLAC's with an attached deposition chamber but increased its capacity of housing up to 6 puck holders in a rotary platform. Even though the electrode shape was modified to maintain less than 3 MV/m at the cathode, avoiding high voltage processing at the operating bias, the photogun showed beam-induced photocathode degradation, reducing the operation to about one week before requiring electron yield replenishing by cesium re-activation of the semiconductor surface [15]. This behavior was related to the use of a strained GaAsP photocathode that produces higher polarization yet is more sensitive to vacuum deterioration. A lower lifetime was also noticed and co-related to gas poisoning from possible desorption of oxygen from metallic surfaces as an effect of undesired electrons emitted during unintentional beam scraping. Regardless of these setbacks, the source was adequate enough for experiments at MAMI, and the use of the load-locked deposition chamber allowed them to improve lifetime, operating reliably for long periods of time.

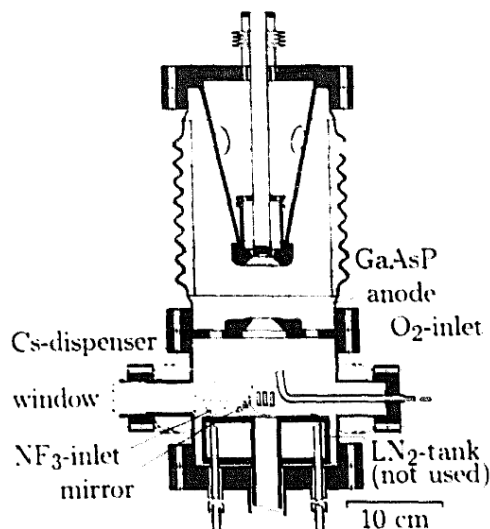


Figure 6: Johannes Gutenberg Universitaet Mainz polarized electron source [3].

The success of the nuclear physics programs utilizing GaAs photoemission to produce polarized electron beams was not overshadowed by the limitations, yet it was clear by then that the challenges related to relatively short photocathode quantum yield lifetimes and high voltage breakdown persisted. In order to fulfill the strict demands of the nuclear physics experiments program at the Jefferson Lab Continuous Electron Beam Accelerator Facility (CEBAF) a polarized photoelectron gun was developed around 1993 [5], based on the original SLAC design. The gun included a Z-spin manipulator that proved to be problematic due to beam transmission problems related to asymmetries in the transport optics. In order to address the latter, a series of solenoids were introduced to control trajectory, which proved to be a cumbersome solution. The space to locate the added control devices was limited, and it took considerable time to correct and restore beam trajectory. Correlated to the beam transport problems that led to beam scraping during initial tests, the photocathode lifetime was poor and required repeated quantum yield

replenishing by Cs deposition, which was solved by activation of a smaller photocathode surface region. The improvements to the design resulted in achievement of higher beam currents, longer photocathode lifetimes, and simultaneous beam delivery to two experimental halls.

As the original gun was operating, a second version was being developed, which delivered the beam at three experimental halls simultaneously later in 1998 [5]. In order to reduce transport obstacles, the optics were modified and the cumbersome Z-spin manipulator was eliminated. To improve photocathode lifetime substantial pumping was added by means of non-evaporable getter (NEG) pumps. In place of the Z-spin manipulator a Wien filter compatible with 100 keV based on SLAC's original design was added, resulting in a significant reduction of distance through which the beam drifts, related to beam quality loss induced by space charge effects. Bulk GaAs photocathodes were substituted with strained lattice GaAs-GaAsP to improve polarization as demonstrated by experiments conducted at MAMI [15]. These modifications fulfilled the required characteristics for parity-violation experiments at Jefferson Lab.

Stepping up the successful implementation of CEBAF's second generation of photoelectron guns, a third iteration was in development and a set of two new sources were installed in 1999 [5]. To further improve the optics of the device the design was modified to be installed horizontally allowing further removal of the electrostatic bends used for beam transport. The photoelectron guns were placed at 15 degrees from the beamline centerline to allow the laser to strike the photocathode at normal incidence, a critical feature to take full advantage of the circularly polarized light to produce the highest possible number of polarized electrons.

Cold metallic surfaces emit electrons through the process known as field emission, in which electrons quantum-tunnel through lowered triangular potential barriers in the presence of high electric fields, in addition to surface work function reductions by contaminants or surface morphology variations [7]. These field emitted electrons can lead to arcing, produce gas desorption as they impact the vacuum chamber walls, and create x-rays that result in unwanted photoemission. The subsequent ionization of residual gas along the electron beam path further deteriorates vacuum and can produce positively charged particles that are accelerated towards the photocathode in a process referred to as ion back-bombardment. These phenomena were identified as the main obstacles in obtaining long photocathode lifetime: ion back bombardment desorbs the cesium layer on the photocathode thus depleting electron yield, and field emission deteriorates vacuum conditions leading to reduced photocathode lifetime due to chemical poisoning (unintentional residual traces of hydrocarbons bind to Cs on the photocathode surface destroying the negative electron affinity, and thus the quantum yield). Thus, the pumping capacities were improved in the new design by installation of NEG modules on the vacuum chamber walls. Record breaking lifetime was achieved with these new sources, but the need for photocathode re-activation was still a challenge.

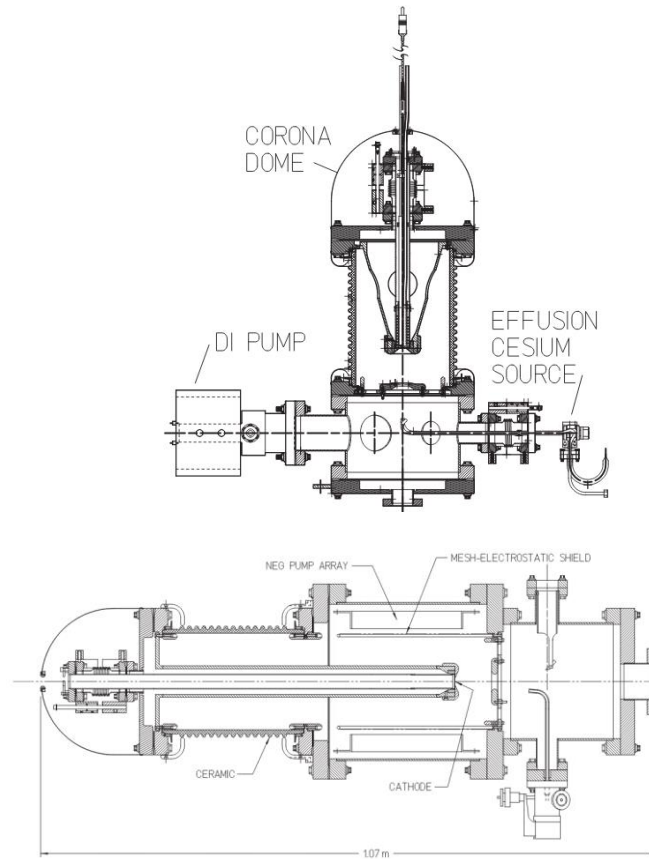


Figure 7: First (left) and second (right) CEBAF polarized electron sources [5].

The photogun design with the large bore insulator is known as a vent-bake style, in which the gun vacuum chamber had to be vented, the photocathode stalk removed to replace the GaAs substrate, and a vacuum bake performed at 200 degrees Celsius for several days. This was a very laborious and time-consuming process with significant detrimental effects on the beam time available for users. A solution was devised by implementing a photocathode storage/preparation chamber behind the gun high voltage chamber and separated by a gate valve. Such a chamber is known as a load-lock chamber and used for these two photoelectron sources. During commissioning in 2006 the load-lock

chamber gun design showed a satisfactory performance at an experimental test bed. Nevertheless, after installation in the CEBAF accelerator initial tests where field emission was present, resulted in a photocathode lifetime below expectations [6]. At the time, the large metallic stalk used to hold and bias the cathode inside the large bore cylindrical insulator was identified as a possible source of field emission, due to the surface area subjected to high electric field in combination with the proximity to the grounded NEG pump modules. The third iteration of CEBAF guns were successfully implemented and delivered a record-breaking highly polarized beam [5]; however, challenges remained and proposed experiments required increasing the high voltage and lifetime, setting the conditions for further improvements.

It is noticeable at this point that a great multilateral collaboration between laboratories accelerated the evolution of photoelectron sources. As a direct result of this collaboration the first inverted-geometry photo electron gun utilizing a conical shape, commercial ceramic insulator was developed for CEBAF in 2007. Building upon an original design from SLAC, a new approach was implemented, substituting the large bore insulator and long metallic cathode holder stalk for a “small” ~13 cm inverted geometry conical insulator that served also as a cathode holding structure. The new insulator represented a cheaper and more readily available option, with the additional benefit of compatibility with commercially available high voltage feed cable used in the x-ray industry. In order to further improve vacuum conditions that lead to longer photocathode lifetime, the new design significantly reduced the amount of metal surface area that contributes to outgassing and is prone to field emission, also resulting in less time used in polishing. The new design allowed for an increase in the distance between the biased

cathode and grounded vacuum chamber components thus decreasing the overall gradient [6]. The design additionally eliminated the need for exposed high voltage leads that previously required corona shield using SF₆ tanks or faraday cage. The cathode was manufactured from two parts using vacuum-arc re-melt stainless steel without welding to minimize field emission from imperfections created at welding points. Additional design changes included the use of thin wall, when possible, at the vacuum chamber to reduce hydrogen outgassing. The inverted photoelectron source design operated for months with excellent 85% polarization and typical electron yield (or quantum efficiency) of around 1% from a strained super lattice GaAs/GaAsP photocathode. It showed good lifetime comparable to previous sources. One of the drawbacks of the inverted geometry gun design is that the insulator-cathode column is perpendicular to the anode-cathode accelerating gap. This results in an asymmetry of the radial electric field along the beam path inducing a vertical deflection of beam trajectory. In addition, even though there was no measurable field emission during these tests, the photocathode showed a degradation correlated with ion back bombardment. Electrostatics simulations performed at the time showed undesirably high electric field of $\sim 7\text{Mv/m}$ at -100 kV located at the cusp of the region where cathode and inverted insulator meet, near the so-called triple-point junction, which have been correlated to high voltage breakdown events.

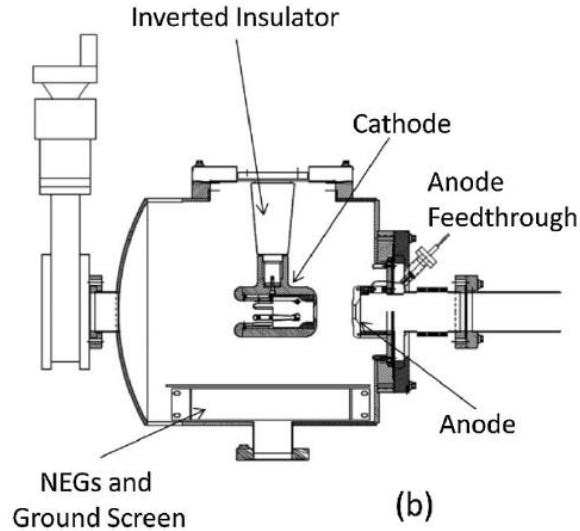


Figure 8: First inverted insulator photoelectron gun design for CEBAF [6].

To further study the bias response of the design, a second setup with the same inverted gun design characteristics was produced for aggressive high voltage testing in 2011. In this case, the option of niobium as a cathode material was explored, since it was desired to operate at -200 kV and niobium showed no field emission at surface gradient > 30 MV/m in low temperature superconducting radio frequency cavities employed for beam acceleration. Additionally, the material was selected due to the possibility of implementing chemical polishing in lieu of labor-intensive mechanical polishing of stainless-steel electrodes using progressively finer silicon carbide paper and finishing with 1 micron grain-size diamond paste. Initial tests showed poor lifetime and the presence of field emission at -140 kV; moreover, high voltage discharge events that resulted in the elimination of electron yield (QE) were present. Subsequent tests with additional polishing allowed for operation with no measurable field emission at -225 kV. The source was successfully operated with the same GaAs/GaAsP photocathodes as CEBAF, yet an

interest developed in further studying the shape of the holding fixture for reducing the gradient at higher operating voltage.

As part of another photo electron beam production program at an experimental test bed in Jefferson Lab, a -350 kV gun was built based on the inverted insulator geometry [16]. In support of CEBAF photogun development, the setup was also used to investigate insulator-cable gap breakdown phenomena, and it implemented the use of an electrostatic triple-point junction screening electrode as an additional part attached to the cathode. It was clear by the time that biasing a cathode at voltages near -300 kV without field emission and high voltage breakdown along this new insulator presented a challenge. Therefore, a spherical stainless-steel cathode was fabricated and mounted on a similar yet longer version of the insulator used in the previous iteration of the inverted insulator gun design, in order to accommodate the larger cathode and higher bias voltages. For the described tests, no photocathode was used due to the main focus on the high voltage response. Several combinations of alumina insulators were used in order to study the introduction of a surface coating or slightly conductive proprietary bulk dopant to provide a degree of drainage of accumulated surface charge. The setup using unaltered alumina with spherical cathode was able to reach -329 kV until insulator failure resulted in a perforation of the insulator. This was attributed to the nonlinearity of the potential along the insulator-connector surface deduced from electrostatic simulations. Implementing the use of a triple-point junction shield cathode the test showed no high voltage breakdown up to -375kV (there was no foreseen need at the time to test at higher voltages), which meant that a robust insulator-cathode-cable solution was found, but field emission was present at undesired levels even though there was no high voltage breakdown. The implementation of the screening cathode

was further studied by means of simplified cylindrical symmetry electrostatics simulations using SuperFish Poisson software [29]. The simulations showed that the screening electrode improved linearization of the potential at the insulator-plug surface but also demonstrated a high gradient at the cusp which was correlated to the increased field emission response. The results [16] proved to be of great value and acknowledged that improved engineering of the screening shield would serve to reduce field emission, correlated with vacuum deterioration and loss of the precious photocathode lifetime and performance while keeping the observed benefits of potential linearization and triple-point electrostatic screening that proved essential to prevent catastrophic electrical breakdown across the inverted insulator.

2. 2 Wien filter

Wilhelm Wien invented the device that carries his name in 1898, based on the application of mutually perpendicular homogeneous electromagnetic fields in a vacuum chamber, and he was able to measure the charge to mass ratio of the electron with this device. Even though his measurement succeeded that of the famous J.J. Thomson, it increased its accuracy and was deemed to be “more elegant” due to the simultaneous application of independent electric and magnetic static fields. The historic literature regarding Wien filters is vast, yet it is hard to surpass the compendium work from Tsuno & Ioanoviciu [9], from which most of the information presented in the following is found. It is interesting to notice that several years went by after Wien was recognized and quoted for the invention, and it is still unclear if subsequent publications that made use of similar devices were the product of independent discovery. It was not until 1934 that R. Herzog and W. Henneberg quoted the inventor in publications that describe the dynamics of

charged particles and the trajectory deflections in the presence of Wien-type homogeneous fields.

It's simple design yet robust working principle has allowed researchers to utilize it in a variety of experiments. Werner Legler modified the Wien filter by substituting the homogeneous electric field for a cylindrical shape thus creating a quadrupole field in order to use the filter as an electron monochromator at 100 eV energy. Hans Boersch and collaborators produced a series of papers in which they implemented the Wien filter as an energy analyzer and monochromator resulting in a significant increase in the energy resolution of the device by implementing retarding and accelerating electrostatic lenses at the entrance and exit apertures of the filter. It was the work by Boersch and collaborators that paved the way for subsequent development and implementation of the Wien filter in electron microscopy. Yet another outstanding application was developed by Matti Salomaa and Harald Enge [19], in which they implemented the Wien filter in 1977 as a velocity selector at Brookhaven National Laboratory in order to analyze the energy and mass of heavy ions generated as fusion products.

The Wien filter finds applications in accelerator physics as a spin angle rotator. During the development of the first polarized photoelectron source at SLAC described previously, it was necessary to analyze the polarization of electrons produced from the GaAs photocathode. To achieve this, a Wien filter was used for rotating the spin to obtain transverse polarization and analyzed by means of a Mott polarimeter [10]. The design used at SLAC was later reproduced during the development of MIT-Bates source for the same purpose; however, the polarization of electrons for the parity-violation experiments was analyzed using a Compton polarimeter at the target [2]. The compact design developed by

SLAC would once again propagate through the accelerator community in need of high polarization photoelectron sources, and as experienced with the development of the electron sources themselves, the Wien filter would prove its value, yet design challenges stemmed from ever increasing beam energy requirements would open opportunities for improvement.

The Wien filter design from SLAC was later reproduced at CEBAF [20], MAMI [12] (shown in Figure 9), and S-DALINAC [4] for operation at 100 keV beam energy for spin angle manipulation, in combination with Mott, Compton and Moller polarization analyzers. The introduction of the compact Wien filter design allows reduced drift lengths that result in loss of beam quality due to space-charge forces. Moreover, the possibility of producing the electric field by means of parallel plate electrodes in an ultra-high vacuum chamber in combination with an external magnetic field induced using window frame coils rendered the device a perfect candidate for implementation with the aforementioned photoelectron sources. The adoption of the Wien filter resulted in record breaking beam energy resolution measurements of the order of 10^{-4} at CEBAF [20], which was paramount for the highly demanding parity-violation experiments that took place at the time. Nevertheless, a previously encountered mismatch between theoretical Wien filter models and experimental results was found, regarding undesired trajectory deviations that impacted beam quality. These deviations have been correlated to the unequal contributions of the electromagnetic forces at the fringe field regions and have been reported in previous experimental findings [4], [12]. Moreover, the higher energy requirements of upcoming experiments at CEBAF and proposed international collaborations where polarized

photoelectron sources are planned to be used, requires modifying the Wien filter design, as it is inherently energy dependent.

While the CEBAF injector Wien filter has been reliably in operation since 1995 configured for 130 keV beam energy, the upcoming Moller parity violation experiments [21] will require increasing the injector beam energy to 200 keV. Motivating the necessity for modifications to the existing Wien filter design for higher electric field across the electrode plates (higher applied voltage per electrode) and higher magnetic field (higher coil current), demand new components capable of robust operation at higher voltage without perturbing the ultra-high vacuum conditions in the injector beam line. Additionally, it is in the interest of the community to obtain relevant information about the electron beam dynamics, as these modifications are implemented, to ensure proper device operation.

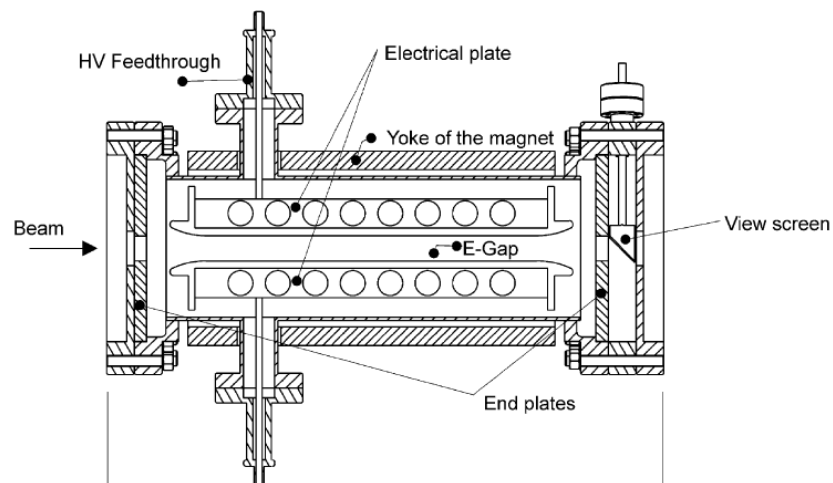


Figure 9: MAMI accelerator Wien filter cross section [15].

2. 3 Simulations in accelerator physics

The discovery of the electron by J. J. Thomson in 1897 motivated more research on cathode rays by means of analytic tools to explain the behavior of charged particles and their interaction with electromagnetic fields, based on Maxwell's equations. By the end of the 1930's the onset of World War II brought a significant impulse to the development of optical and electronic devices [34]. Relevant to this work is the exploration of electron flow in the presence of cathodes with different geometries by J. R. Pierce in 1940, developed using a theoretical framework based on solving Poisson's equation with known boundary conditions determined by the electrode shapes [35], in order to obtain rectilinear particle motion in electron guns. Similarly in the context of Wien filter high voltage plates, attempts were made [Jones, 1956] to obtain analytical solutions to optimize the shape, specifically the Rogowski profile, of cylindrically symmetric electrodes in order to aid in the homogenization of the electric field and to reduce the deviation from ideality in the fringe regions. These efforts to describing and optimizing the shape of such electrodes had a significant advance with the development of sophisticated computational tools, where, for example, the so-called Algol procedure was used to solve Laplace's equation in cylindrical coordinates for the named electrode configuration [36].

The field of accelerator physics naturally benefited from the development of sophisticated computational tools dedicated to calculating electromagnetic fields and particle interactions with them, such as SLAC's EGUNS developed by Bill Herrmannsfeldt for dedicated numerical simulation of electron guns in 1988 [37], and Poisson/Superfish developed for Los Alamos National Laboratory by R. Holsinger and K. Halbach and published in 1992 [30]. Accompanied by simulation codes, the crucial development of

modeling tools that allowed for the creation of geometrical shapes representing device components also benefited from the sharp increase in availability of computational tools, as Reinard Becker's POLYGON, that was used in combination with EGUNS to simplify the creation of boundary files [38].

Electron guns were and are still used in a variety of applications: old television sets, oscilloscopes, microscopy, radars, x-ray machines, and in fundamental research. As described in sections 2.1 and 2.2, the successful implementation of a device tends to be adopted and subsequently improved, following the continuous evolution of technical and scientific tools. The initial limitations of computational codes that used 2-dimensional representations and relied on symmetry have been tackled, leading to increased capabilities that allow for full 3-dimensional modeling [22], simulations [24], and fabrication methods. The optimization processes of accelerator physics devices and components has also been widely established, becoming indispensable [39] in the development of these instruments. Goal-oriented practices have been implemented historically with software to analyze and optimize electron gun components and Wien filter characteristics that benefit from highly symmetric device geometries, for example: [3], [4], [5], and [6]. Relevant efforts have been made with respect to the optimization of a thermionic electron gun geometrical parameters [40] and its effects on the produced electron beam and more recently in the optimization of a cathode shape to minimize field emission of an inverted insulator photoelectron gun [41]. However, the inherent asymmetry of the CEBAF photoelectron gun, the necessity of assessing the impact of proposed modifications not only on the cathode but also the internal surface of the inverted insulator that serves as a holding structure, and the beam dynamics

on the cathode-anode gap region, motivated the development of the work presented in this document.

CHAPTER 3

METHODS AND RESULTS

The methodology described in this chapter is part of an iterative process, in which the results are used as inputs that guide the proposed modifications, thus creating the necessity of presenting the content as a single section. Moreover, as the same methodology was used in the development of both the photogun and Wien filter, each subsection is separated accordingly to highlight the particularities of each device.

3. 1 Proposed system

The inverted insulator photoelectron source and Wien filter based on SLAC's design adaptations became widespread in other laboratories such as Mainz, Darmstadt, CEBAF, and have even been proposed as a very strong choice for future projects as the International Linear Collider (ILC) [17] and the Electron Ion Collider (EIC) [18]. The requirements for higher electron beam energy and higher polarization continue then to pose serious challenges. Biasing the existing inverted insulator photoelectron gun design at 200kV subjects regions of the cathode to high electric field that have been observed to correlate with insulator failure. To retain the benefits of using the inverted insulator gun design, it becomes necessary to shield the location where ceramic, electrode and vacuum meet using an additional cathode structure known as a triple junction shield that significantly reduces the gradient. The shape of the triple junction shield strongly influences beam dynamics across the anode-cathode gap, the electric potential along the insulator, and finally undesired field emission stemming from high gradient surfaces.

This work focuses on an iterative modeling, design and simulations approach with subsequent high voltage characterization of two Jefferson Lab CEBAF injector components:

- a) an inverted insulator photoelectron gun with a single piece cathode-electrode that includes a methodically engineered electrostatic shield, designed to reduce the likelihood of insulator arcing by controlling its geometrical characteristics, while maintaining the potential linearization benefits described in [16], and
- b) a Wien filter spin rotator upgrade compatible with the photoelectron source energy increase, as it is necessary to provide spin rotation angle control.

The results presented in this document include the use of electrostatic and beam dynamics simulation tools to validate the merit of the proposed modifications and evaluate the impact on the dynamics of the electron beam. This system is anticipated to fulfill the requirements of a 200keV beam energy operation for Jefferson Lab's CEBAF injector nuclear physics experimental program and improve the capability of inverted insulator photoelectron guns for future experiments.

This work was carried under the tutelage and close supervision of Jefferson Lab staff scientists and pioneers in the operation and development of photoelectron guns.

3. 2 Methodology

Paramount to the existing electron gun and Wien filter designs and their function is the relation between the necessity of operation at high voltage and its impact on vacuum conditions, which directly affects beam quality and lifetime of the photocathode. The

methodology is based on implementing design and simulation tools to generate electrostatic field maps that allow the identification of regions where the electric field magnitude might result in undesired field emission, and to analyze the impact of proposed design solutions on beam quality and operational reliability. Once the desired gradients were achieved, relevant simulation data files are generated to use in combination with particle tracking software to study the beam dynamics of the proposed device. The methodology relies heavily on a feedback process, resulting from iterations of the various proposed design solutions. When the design results in satisfactory electrostatics and beam dynamics, the manufacturing drawings were updated with the proposed changes. Finally, prototypes are manufactured and evaluated by studying the vacuum response to high voltage and by characterizing the electron beam. Figure 10 shows a workflow diagram that summarizes the methodology developed in this work.

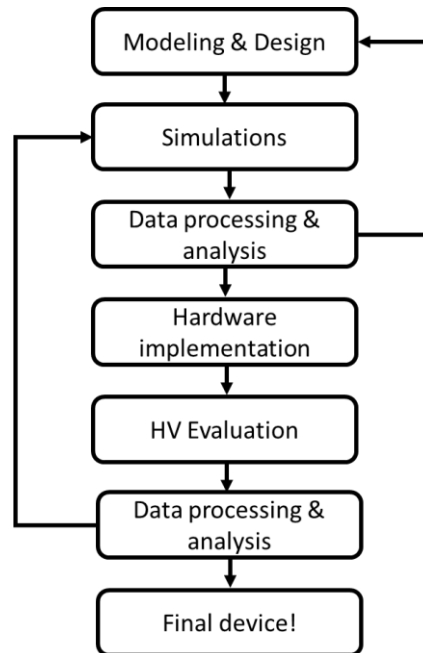


Figure 10: Workflow methodology for electrostatic device development

3. 3 Modelling and design

Manufacturing drawings of the existing 130 keV electron gun and Wien filter are used to produce baseline and proposed 3D models using *Dassault Systemes Solidworks* software [22]. A total of 9 CAD drawings were used for the modeling of the electron gun, and 11 drawings were used for the Wien filter. The models are then used as inputs in the simulations section, and the results are part of the iterative process that leads to the implementation of design changes. These changes are then implemented again in the Solidworks model, and the process is repeated until a satisfactory model is achieved.

3.3.1 Modelling

Using the 3D modeling software Solidworks, four separate models were produced. Two corresponding to the existing and proposed photoelectron gun and two corresponding to the existing and proposed Wien filter designs. It is relevant to mention that the methodology allows for multiple intermediate iterations that result in the four final models.

Initially, original construction CAD design drawings are obtained, reviewed to correspond to the existing designs, and classified. Each device corresponds to a CAD assembly separated in components referred to as parts. Given that these are construction drawings that show the devices in full detail (such as screw threads, for example), the classification is made based on the relevance of each separate part on the device electrostatics. Once the CADs are classified each device is modeled separately. Since the results of the electrostatics simulations were used in beam dynamics simulation software as inputs, it was relevant that all simulations share a common, well defined coordinate system. In the case of the electron gun, the origin of the coordinate system was defined at the center of the cylindrical cathode electrode; in the case of the Wien filter, it was defined at the center of the vacuum chamber.

The parts corresponding to each assembly are modeled and stored in individual files with well-defined part names. This allows for proper identification and organization of the assemblies, and it has proven to be very beneficial to the Injector group, since the models are consulted and used by different group sections (i.e. design, survey and alignment, simulations, construction). During the part modeling, additional considerations must be made regarding the impact of geometrical details on the device electrostatics in a “defeaturing process”, where minute details as screw threads, flange coupling grooves and

atmosphere-side features are intentionally removed from the model to save computational time and prevent meshing issues during the simulation process. Additionally, parts that contain geometrical features with dimensions $<5\text{mm}$ are subdivided to enable fine control of mesh size during the simulation process. For modeling and simulation purposes, the constituting parts of each device are listed below, where some are grouped for readability even though in the final models they were separated in subparts.

Electron gun

- Cathode electrode
- Alumina insulator with Kovar rings
- Rubber cable with internal HV conductor
- Anode and beam line
- Non evaporable getter (NEG) pump
- Cylindrical vacuum chamber with (25.4 cm diameter)10 in ConFlat® flange

Wien filter

- HV electrode plates with mounting tabs and Rogowski profile
- HV spring guide contacts with spring coils
- HV electrical feedthroughs with alumina insulators
- MACOR mounting insulators
- Vacuum chamber with electrode mounting springs
- Magnet coils
- Magnetic field clamping endplates with apertures,

- Pole plates and return yokes

Once all the parts are generated, the device is assembled in Solidworks by means of the “mating” feature that creates spatial relations between part regions (i.e. points, edges, faces). It is imperative to create the final assembly in this manner, as alignment of the parts using transform operations might result in meshing mismatch issues preventing the electrostatic simulation to resolve. Figure 1 shows a cross section of the 130 keV photoelectron gun with pink insulator and dark blue rubber plug; Figure 2 shows a cross section of the Wien filter with pink vacuum chamber, light blue HV electrode plates, green HV spring guides, dark blue magnetic mirror end plates, and red magnet coils. In some cases, an additional vacuum region was added to the assemblies to provide further control of mesh size, in order to produce field maps of the necessary resolution to be compatible with the beam dynamics software.

3. 3. 2 Design

3. 3. 2. 1 Cathode electrode

The inverted geometry ceramic insulator extends into the photogun vacuum chamber positioning the cathode electrode at the center and electrically isolating it from the vacuum chamber at ground potential. When the electrode is biased, high gradient at the triple-point junction, where metal from the ceramic insulator braze joint, alumina and vacuum intersect, often leads to surface flashover triggering arcing and consequently catastrophic insulator damage [23]. These phenomena are correlated to cathode electrode design features [16], so reducing the field strength at this location is essential for reliable

operations. The transverse component of the electric field near the triple-point junction is especially important due to its tendency to drag charged particles towards the insulator surface, likely inducing secondary electron emission avalanche and/or electron cascades within a thin layer near the surface, that in turn might desorb gas that once ionized can lead to breakdown along the insulator surface. Furthermore, charge accumulation on the insulator surface can lead to breakdown by changing the electric field distribution near the insulator surface [32]. The proposed electrode modifications addresses these challenges by shielding the triple-point junction. In the existing CEBAF cathode, referred to in the following as T-cathode due to its shape, this region has ~ 3 MV/m gradient, as the original design provides some degree of triple-point junction shielding. However, the gradient on the shield cusp is ~ 29 MV/m thus making it prone to field emission. It is also well known that pure alumina insulators suffer from charge accumulation, leading to insulator punctures in inverted insulator tests [16]. The proposed implementation of a cathode electrode with electrostatic shield aims to mitigate these phenomena by shielding the triple-point junction and by increasing the cusp radius to reduce electric field on the metal surface. Various possibilities to achieve this were explored and led to a prototype where the electrostatic shield height serves to significantly reduce the gradient at the triple-point while the cusp tapers away from the insulator surface following its curvature to provide linearization of the potential along the internal insulator surface. As is further explained in the following sections, the geometrical properties of the shield (i.e. curvature, height, length) shown in the inset of Figure 11 should be controlled to prevent detrimental impact on the electric field at the cathode-anode gap. This region is paramount to the gun design, since modifications to it can result in lower electron beam quality.

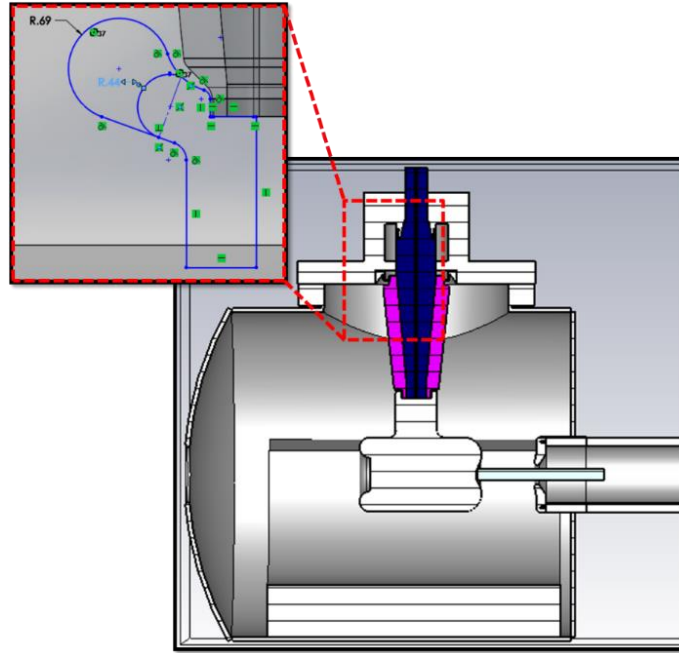


Figure 11: Longitudinal cross section of the existing CEBAF -130 kV photoelectron gun. The inset shows an outline close-up of one of the proposed electrostatic shield modifications.

The aforementioned modifications must be realized within the constraints of surface area prone to field emission, and weight that represents additional gas load and to prevent overstressing the holding structure joints and fasteners. Other considerations include the use of a simple structure with minimal amount of geometrical variations and transitions between geometrical features that results in a part that could be machined within the projected time and budgetary restrictions of the project.

The present CEBAF 130 kV T-cathode is mounted on a pure alumina insulator, but upgrades to 200 kV required the use of a different shape and the use of doped alumina insulator to accommodate the proposed electrostatic shielding electrode, and to provide some degree of charge drainage, respectively. As shown in Figure 12 the radius of the cusp

of the CEBAF 130 kV T-cathode was increased from 0.30 cm (~0.12 in) to 1.75 cm (~0.69 in) for the first iteration and to 1.11 cm (~0.44 in) for the second iteration in the electrode models. The height and length of the first iteration shield were kept to 7.59 cm (~2.99 in) and 4.06 cm (1.60 in) to maintain sufficient distance to the top grounded flange, thus keeping a low electric field magnitude at the “cusp” of the shield. The interior perimeter of the shield was tapered away from the insulator, decreasing the field on its inner surface. Overall, the contour of the shield was designed to keep the maximum value of the field around the cusp below 10 MV/m at -200 kV, to prevent field emission and minimize the amount of cathode electrode material added to the vacuum chamber, which represents an additional gas load.

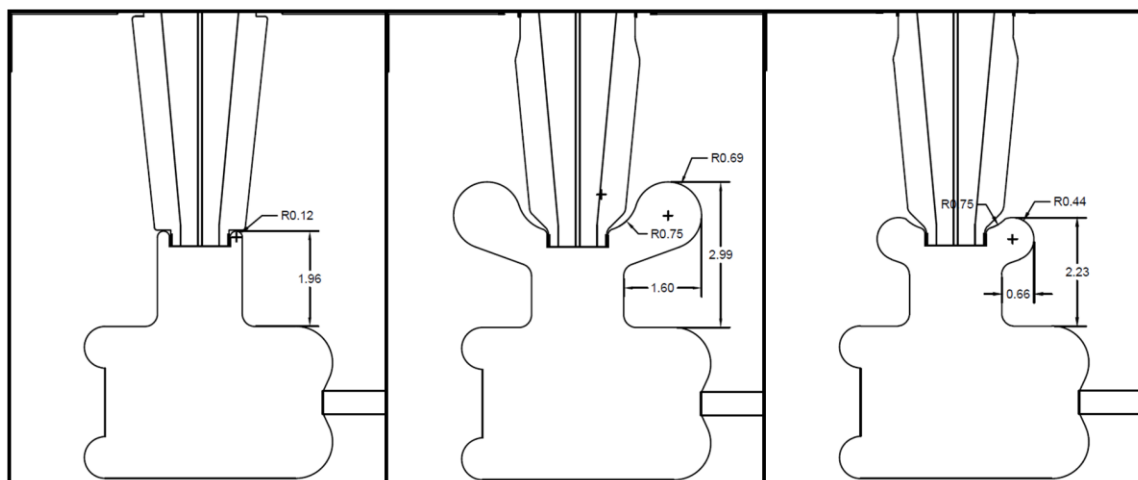


Figure 12: Longitudinal cross section of the cathode electrode shapes. The existing CEBAF photogun t-cathode (left), the first iteration shield (center), and the second iteration shield (right). Dimensions shown in inches.

As part of the iterative process, it was found and later published as part of reference [26] that the first iteration shield introduced an undesirably high vertical beam deflection by increasing the magnitude of the transverse vertical component of the electric field at the cathode-anode gap. Therefore, a second iteration design was produced as a result of seven shield design tests with different geometries that resulted in a height and length reduction to 5.91 cm (~2.33 in) and 1.67 cm (~0.66 in).

3. 3. 2. 2 Wien filter

The Wien filter is used in Jefferson Lab as an electron spin rotator by applying independent and mutually orthogonal homogeneous electric and magnetic fields. The electric field is generated by applying high voltage to two identical but opposing electrode plates in ultra-high vacuum conditions, while the external magnetic field is produced with direct current through a set of window-frame coils that surround the vacuum chamber. The Thomas-Bargmann-Michel-Telegdi equation that is used to describe the dynamics of a longitudinally propagating electron beam at relativistic energy, subjected to the named field configuration, can be simplified to a commonly used [12] proportionality relation between the fields and the beam kinetic energy, as shown in Appendix. A. 4. The resulting mathematical formalism is used to define the electric and magnetic fields magnitude and profile that determine beam dynamics, while modeling is utilized to integrate the mechanical, electrical and magnetic designs.

To upgrade the existing CEBAF Wien filter from 130 keV beam energy to 200 keV, the electric field must be increased from 1.6 to 2.7 MV/m, and the magnetic field from 9.1 to 13 mT, surpassing the capabilities of the existing device. The specific parameter values

are discussed in detail in section 3.4. As in the previous case, the modifications must be realizable within the time and budgetary constraints on the project. In addition to the obvious increment in high voltage and magnet power supplies outputs, an increase from 20kV to 40 kV rated HV feedthroughs was proposed in this work, which needed communication with manufacturing vendors to obtain technical data for feedthrough designs to ensure those were geometrically compatible with the existing setup. The obtained design information was then used to model the corresponding part using Solidworks per the process described in the previous section and substituted in the baseline model assembly. Implementing this methodology, the following components were re-designed.

The existing parts that provide electrical contact between the HV feedthrough and the electrodes, referred to as HV spring guides, are too short and lack the proper geometry to mate with the feedthrough. This requires modifications to the metallic HV spring guide to allow compatibility with the new feedthrough, while maintaining the dimensions that minimize the electric field on the surface to prevent field emission. The modification to the HV spring guide was a two-stage process; first the chosen 40 kV commercial feedthrough connector detail had to be measured to sub-mm precision since the vendor could not release proprietary information; then a model was constructed to match as close as possible the physical feedthrough. Figure 13 shows the 40 kV rated feedthrough with alumina insulator in yellow, the HV spring guide in green, and the long version of MACOR mounting insulator in gray.

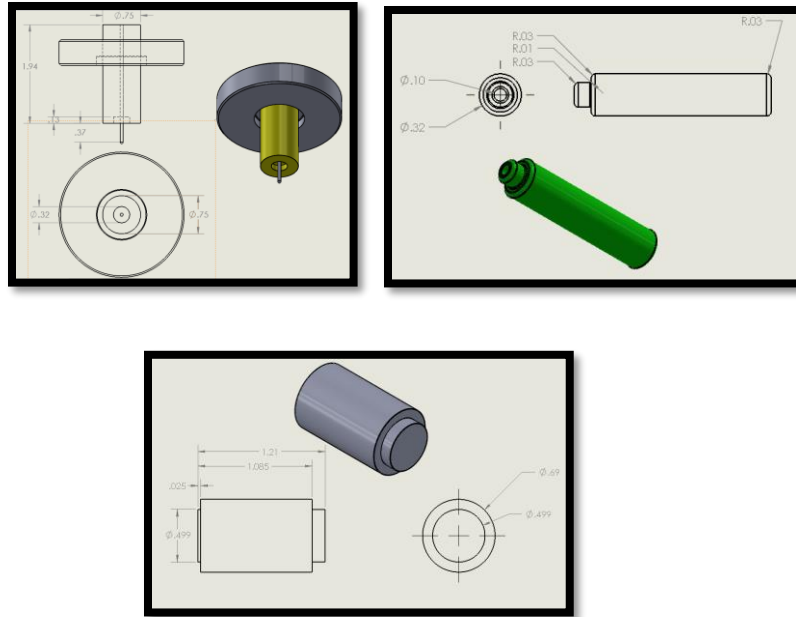


Figure 13: Proposed 40 kV rated HV feedthrough with 2 $\frac{3}{4}$ flange (left), proposed MACOR long mounting insulator (middle), proposed HV spring guide contact compatible with new feedthrough (right).

In addition, the longer versions of the mounting insulators that function as fixtures to hold the electrode plates in place are implemented. The resultant increased gap between the biased electrodes and grounded components aims to reduce the gradient between the electrode plate tip Rogowski profile and mounting fixtures, thus reducing the risk of producing unwanted field emitted electrons that can potentially be accelerated towards the vacuum chamber or to the beam line passing through the magnetic mirror endplates apertures.

Due to previously available manufacturing processes, the existing electrode plates were manufactured using three separate pieces welded together, namely: electrode plate profile with Rogowski tips, strong back rib and mounting tabs. These were designed and

manufactured using splines in order to provide the metal surface with a shape that allows for a smooth transition from the homogeneous electric field region to the Rogowski profile tip after polishing. Since the upgrade device modifications involve subjecting the electrodes to a higher bias voltage, and due to recent availability of advanced manufacturing techniques, single-piece electrode plates were revised and manufactured, substituting existing splines giving shape to the Rogowski curvature for smooth curves, thus removing the necessity of welding which could negatively impact vacuum quality by releasing gaseous species or by creating low level field emission from sharp surface protrusions. The modification is also compatible with modern surface preparation techniques by tumbler polishing, reducing the necessity of time consuming hand finishing.

3. 4 Simulations

The implementation of simulation tools is essential for the development of accelerator physics devices and instrumentation. In this work, electrostatic simulations are used to obtain information on the potential and electric field on regions of interest to drive the optimization process of the photoelectron gun cathode electrode and the modifications to the Wien spin rotator, and to produce 3-dimensional field maps which are used as inputs in the beam dynamics tracking software to study the impact of design modifications on the electron beam trajectory and quality in both devices.

The previously obtained 3D models of the electron gun and the Wien filter are used to produce electrostatic field simulations. The CST EM Studio [24] software provides a complete 3-dimensional description of field components that are further implemented to obtain beam dynamics simulations using Pulsar Physics General Particle Tracking software

(GPT) [25]. The resulting files are post processed and analyzed using Python and Excel, as described in section 3.7. This work methodology allows for the multiple iterations that are part of a feedback process that leads to the final device designs being implemented and tested. The use of 3D simulations not only allows the production of a comprehensible summary of a device expected behavior but also provides a multiplatform-compatible data base that can be used and modified by the Injector group in the future.

3. 4. 1 Electrostatics

To generate 3-dimensional electrostatic simulations, the baseline and upgrade models for the photoelectron gun and the Wien filter described in the previous section were imported into CST EM Studio. In this process it is relevant to make sure that the defined reference frame is selected, since several simulations can be run in series. CST EM Studio is a finite element simulation software that solves Maxwell's differential equations system in a 3D volume by representing the geometry with tetrahedral polygons (i.e. mesh) with known boundary conditions that were established by defining the cathode potential as well as surrounding grounded vacuum chamber. At this stage the method used to create assemblies by a "matting" process becomes relevant since mismatches between parts of the assembly will result in overlapping tetrahedral of objects with different material properties, which in turn result in unsolvable differential equation systems, preventing CST to find a solution for the model.

A successful simulation run produces a data file containing the E_x , E_y , E_z components of the electric field in the simulation volume with coordinates x , y , z , that can be read and post-processed by CST, either to create visual representations (i.e. false color and arrow plots) as the one shown in Figure 14, or to obtain worksheet-type files that allow

further analysis and visualization through Excel and implementation in GPT beam dynamics software, as discussed in section 3.7.

The following is a description of the procedure to obtain data on relevant regions used for this methodology:

3. 4. 1. 1 Electron gun

- Insulator inner surface (also known as vacuum side): A line following the internal surface of the longitudinal cross section is obtained by the two-points equation. Subsequently, the coordinates of homogeneously distributed points along the line is obtained with Solidworks and stored in a comma-separated value file (*.csv) that is used in CST as an input, producing the electric field (E_x , E_y , and E_z) components as an output.
- Potential linearity: the same procedure described above is used, using the scalar potential at the coordinates as an output.
- Cathode electrode surface: False color plots are obtained with the CST post-processor using a 10 MV/m as an upper limit on the color scale and 0 MV/m as a lower limit. Additionally, numerical values of the electric field can be obtained on specific locations on the cathode surface using the “field on point” feature. This is used to locate cathode regions prone to field emission.
- Cathode-anode gap volume: The post processing tool is used to interpolate the value of the field components along the volume defined by a 3 mm X 3 mm X 30 cm prism with one face on the photocathode surface and the opposite face past the

anode aperture. Using 1 mm step size, a data file is obtained and used as an input in GPT to generate beam dynamics simulations.

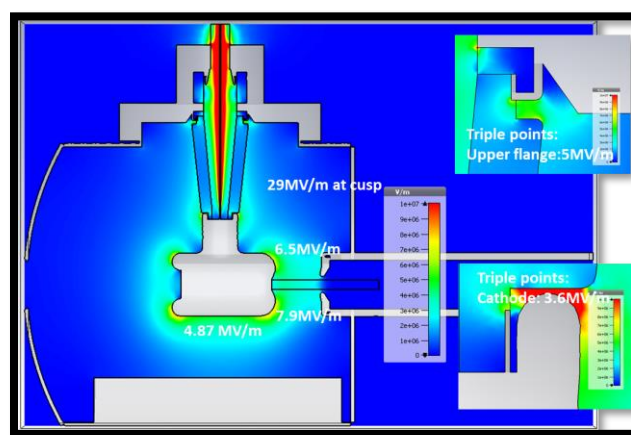


Figure 14: Longitudinal cross section false color plot of CEBAF existing -130 kV photoelectron gun. The insets show close-up to the bottom and top triple points.

For the first iteration of the electrostatic shield and due to the availability of the software package, Comsol simulations were produced, and the results are presented in Figure 15 which provides lateral cross-section views of both photogun designs, with false-color graphics indicating potential (left) and field strength (right). The high field strength values within the rubber plug region do not pose a design concern due to the high dielectric constant of this material. The simulations show a field strength reduction of $\sim 100\%$ near the triple-point-junction: only 172 V/m in the new photogun design, compared to 15 MV/m. The highest field strength in the new photogun design is ~ 7.5 MV/m, at the “cusp” of the trip-point-junction shield, a value deemed acceptable. Other locations of interest are

shown in Figure 2, as these points represent key positions in the photogun where high electric fields might lead to detrimental field emission, arcing or unwanted modifications of the electric field within the cathode-anode gap that could negatively impact beam delivery. The field strength at these locations in the new photogun are comparable or less than values at similar locations within the older gun design.

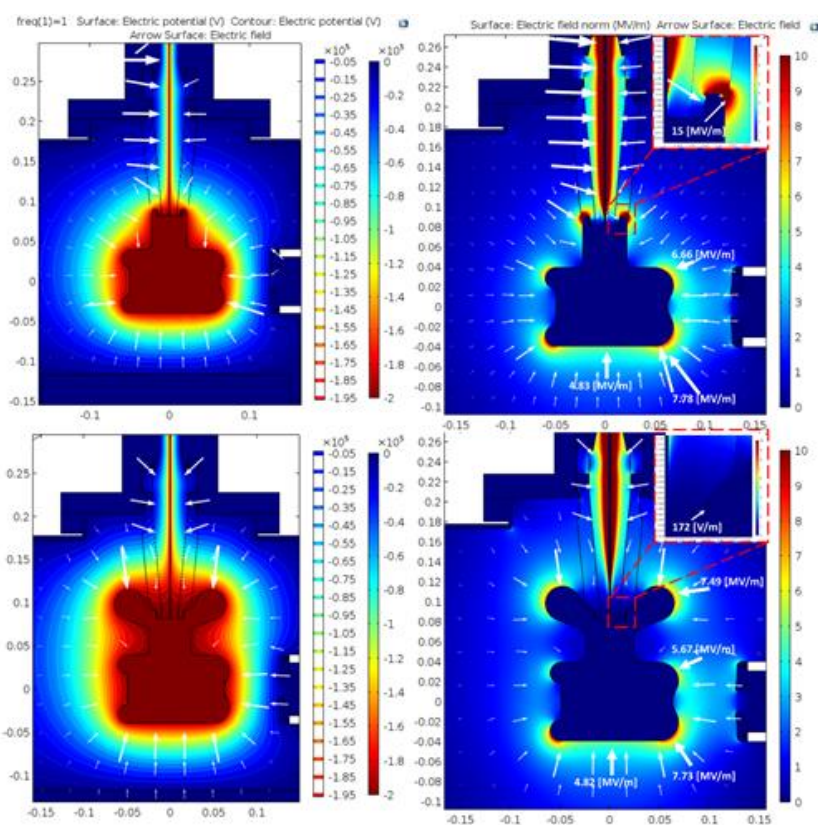


Figure 15: False-color lateral cross-section views of the electrostatic field strength within two photoguns: (top) the present day CEBAF photogun with un-doped alumina insulator, and (bottom), the new photogun that includes a triple-point-junction shield electrode and doped alumina insulator. Potential (left) and electric field maps (right) are for both photoguns biased at -200 kV. The white arrows are proportional to the electric field normal to the equipotential lines. Horizontal axis scale in meters. The color scale corresponds to the potential in V (left) and electric field norm in MV/m (right).

Figure 16 (top) shows the electric field strength (potential gradient) and (bottom) the electric potential plotted along the length of the insulator at the rubber plug-insulator interface, for both photogun designs. Based on literature reports discussed in the previous sections, it is clear that the best electrostatic design provides a relatively small electric field strength near the triple-point-junction and a potential that varies linearly along the length of the insulator. As shown in Figure 16, the new electrostatic design (red) provides considerable improvement over the original design (blue). The electric field strength in the new photogun is very small near the triple-point-junction ($0.08 < y < 0.1$) and gradually increases to ~ 4 MV/m, representing a $\sim 22\%$ reduction overall, compared to the original photogun design. Similarly, the potential along the length of the insulator varies more linearly.

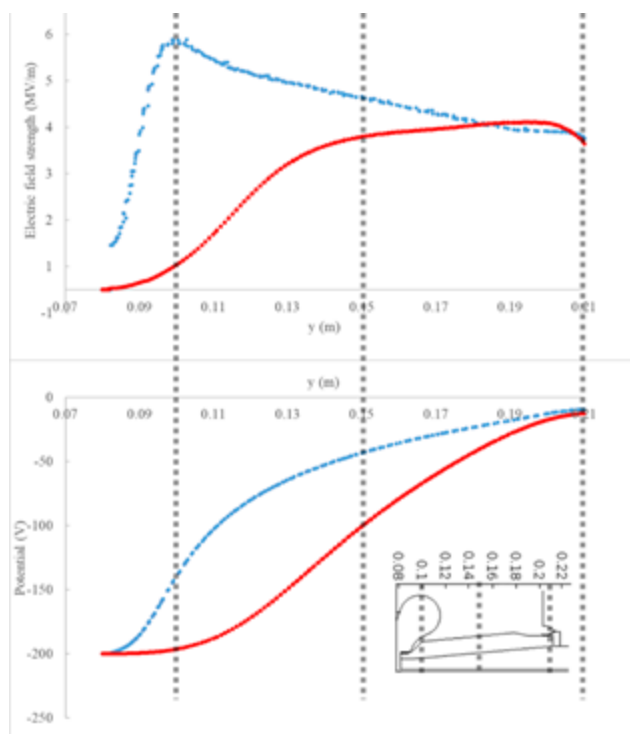


Figure 16: (Top) Electric field strength and, (bottom) the potential along the rubber plug-ceramic insulator interface for two photoguns: (blue) the present day CEBAF photogun with un-doped alumina insulator, and (red) the new photogun that includes a triple-point-junction shield electrode and doped alumina insulator. Both photoguns biased at -200 kV. The dotted gray lines represent positions along the insulator (see inset).

As described in section 3.1., a second iteration of the model was produced in order to reduce the impact of the electric field in the cathode-anode gap region, which translates into unwanted vertical deflection of the electron beam. The electric field simulations were produced this time with CST EM Studio. Naturally, in order to properly compare the models, the simulations for the existing CEBAF photogun and the first iteration models were repeated in CST. Figure 17 shows a comparison of lateral cross-section views of the three photogun designs, with false-color graphics representing the electric field magnitude. The relevant fields in the context of the aforementioned methodology show that the fields

remain within the proposed limits of 10 MV/m. The magnitude of the electric field at the cusp now presents a 72.7% reduction compared to the original model and only an 8% difference with the first iteration, while the fields around the perimeter of the cathode electrode this time remain within 2% difference with the original design as desired. The triple points not shown in the image present a decrease of 66.6% measured at the same point near the metal surface.

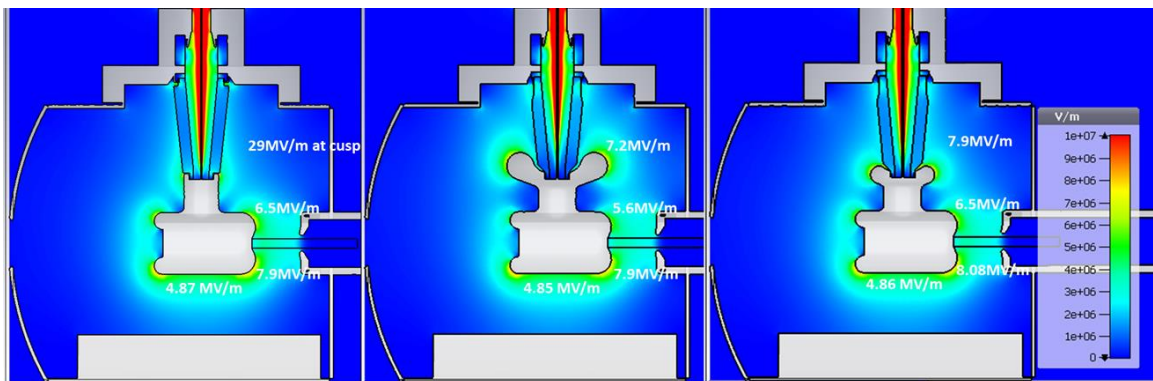


Figure 17: False-color lateral cross-section views of the electrostatic field strength within three photoguns biased at -200 kV: (left) the present day CEBAF photogun with undoped alumina insulator, (middle) the first iteration photogun that includes a triple-point-junction shield electrode and doped alumina insulator, and (right) second iteration photogun with smaller triple-point junction shield. The color scale corresponds to the electric field norm in V/m.

Another key aspect of the photogun electrostatic design is the magnitude of the transverse electric field component along the axis between the photocathode and the anode. Ideally, the transverse electric field in this region should be zero to prevent beam deflection of the trajectory. Photoguns with symmetric cathode/anode designs satisfy this condition [6]. The “side-insulator” design described here provides an important practical advantage

related to photocathode installation within the cathode electrode, but as discussed in section 2.1, it introduces an asymmetry in the electrostatic field within the cathode-anode gap. The simulations in COMSOL indicate that the electrode triple-point-junction shield amplifies this field asymmetry, concurring with the experimental observations. Therefore, the second iteration of the electrode with a smaller electrostatic shield was modeled and the electrostatic fields simulated, this time using CST EM Studio since we lost access to the previous software. The exact design criteria and steps described in section 3.3 were used to produce the electrostatics simulation. Figure 18 shows the transverse vertical electric field component probed along the center line between the photocathode and the anode (shown as a red line in the upper right inset). The transverse component has an increase of 20% for the second iteration model and >50% for the first iteration model, compared with the original CEBAF design. Despite adversely affecting E_y , the second iteration of the shielding electrode was chosen for ensuring robust operations without insulator arcing, since this electrode significantly reduces the gradient at the triple-point junction.

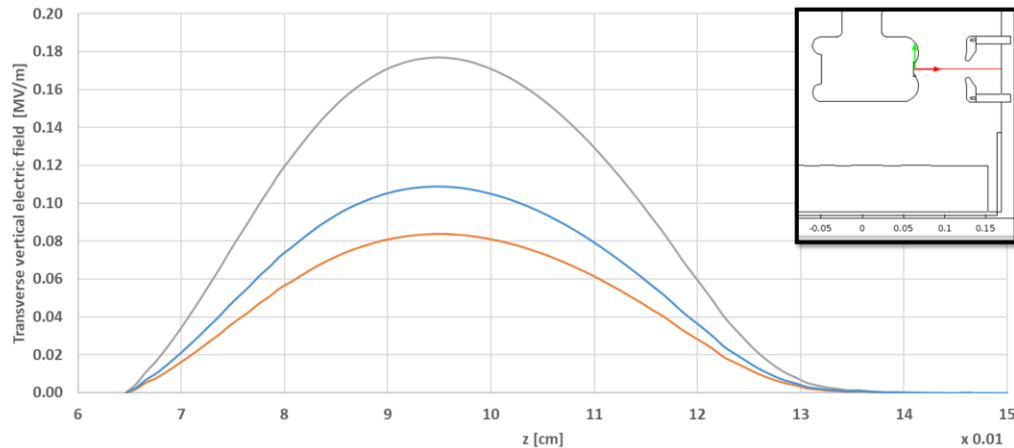


Figure 18: Transverse electric field within the cathode-anode gap, along the centerline of the photogun as shown by the red line in the inset detail. Orange, blue and gray data points correspond to original, first iteration, and second iteration photogun designs respectively. All produced with -200 kV bias voltage.

3. 4. 1. 2 Wien filter

To increase the Wien filter operation energy to 200 keV the implementation of 40 kV rated CeramTech feedthroughs with alumina insulators and 6.985 cm (2 $\frac{3}{4}$ in) ConFlat flanges, compatible HV stainless steel spring guides with springs, and 3.07 cm MACOR “long version” mounting insulators was proposed. Figure 19 shows a lateral cross sectional view of the existing 130 keV CEBAF Wien filter design and the proposed 200 keV upgrade, to denote the suggested modifications which are color coded as follows: the HV feedthroughs with (yellow insulators), HV spring guides (green) and mounting insulators. The evaluation of the suggested modifications by means of electrostatic simulations is discussed below.

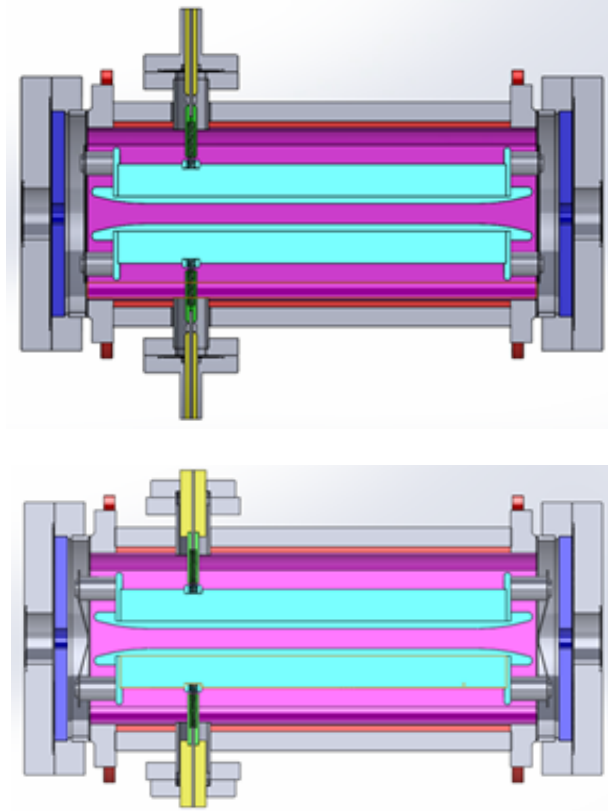


Figure 19: Lateral cross-section of the present 130 keV CEBAF (top) and proposed 200 keV upgrade (bottom) Wien filter models in Solidworks.

The 3D models generated for the 130 keV CEBAF and the 200 keV upgrade version using Solidworks [22] described in section 3.3 were used. Each part was modeled separately; then the pieces were assembled together and exported as a single file for each model. Both models were then imported into CST Electromagnetic (EM) Studio software [24] to generate electrostatic simulations. As in the previous section, after importing the model, the metallic materials are defined as perfect electrical conductors (PEC), the insulators are assigned the characteristics of the corresponding material (alumina, MACOR), open boundary (Neumann) conditions are defined at the feedthroughs and at

flanges that would be connected to the beam line in the physical machine, as these correspond to open ends. Closed boundaries (Dirichlet) are defined for the lateral limits along the x-axis, as these correspond to metallic ground-potential walls. In this case an automatic mesh process was defined, since it proved enough to produce quality results. Finally, the EM solver was used in order to obtain the electric field solution to both existing and upgrade models. A comparison between the results obtained for the 130 keV and the 200 keV Wien filter versions focused on four sectors:

- High voltage feedthrough
- High voltage spring guide
- Electrode Rogowski profile tip
- Electrode mounting tab cusp

Figure 20 shows a false color electric field magnitude plot on a cross section on the insulator and metallic surfaces at the feedthrough-nipple gap region for both 130 keV present CEBAF (left) and 200 keV upgrade (right). The results show that the upgrade feedthroughs maintain acceptable electric field values (below 10 MV/m at maximum operating voltage) with the additional benefit of a smaller metallic surface area exposed to high voltage.

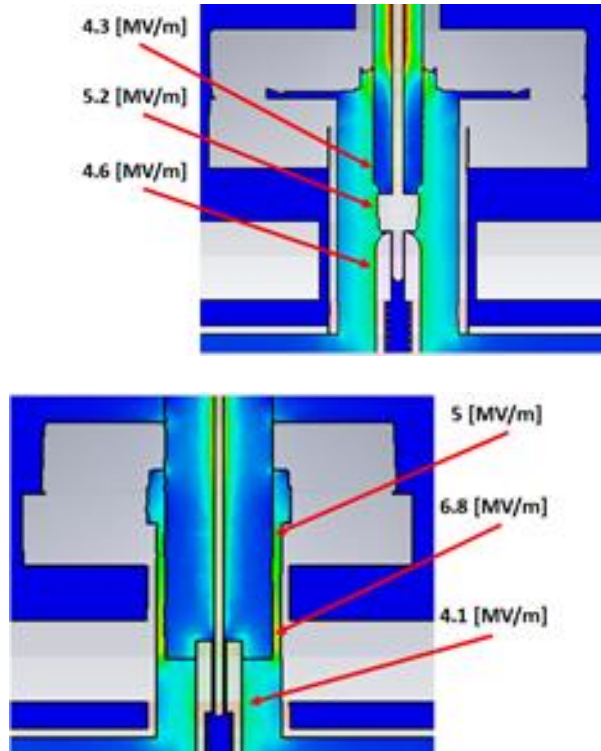


Figure 20: False color plot of electric field magnitude on a lateral cross section of the feedthrough-nipple gap for the present 130 keV CEBAF (left) and proposed 200 keV upgrade (right) Wien filters.

The simulations allowed the identification of the high voltage contact between feedthrough and spring guide as a region of interest due to the curvature of its edges and the presence of triple junction points. The HV Spring guide contact was then modified accordingly to be compatible with the higher voltage feedthrough, while controlling the dimensions that minimize the field on the metallic surface and ensuring smooth curved transition with the feedthrough as shown in Figure 21.

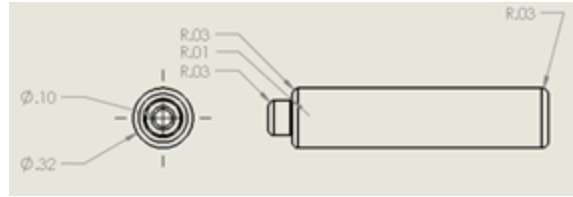


Figure 21: CAD of the proposed HV spring guide with adapted dimensions to match the proposed 40 kV feedthrough.

Since the curvature of the Rogowski profile was designed to improve the equilibrium between the electric and magnetic field contributions to the total force at the fringe regions, modifying it was not an option at this stage. Instead, longer insulator standoffs were simulated with the objective of increasing the gap between the electrodes and grounded metallic support structures for reducing the electric field magnitude at the Rogowski tip and holding structure gap. The red arrow in Figure 22 shows that the gradient at this region is reduced from ~ 3 MV/m to < 1 MV/m when the gap between the electrode mounting tab and the ground electrode mounting frame is increased from 2.12 cm to 2.54 cm by using longer insulators.

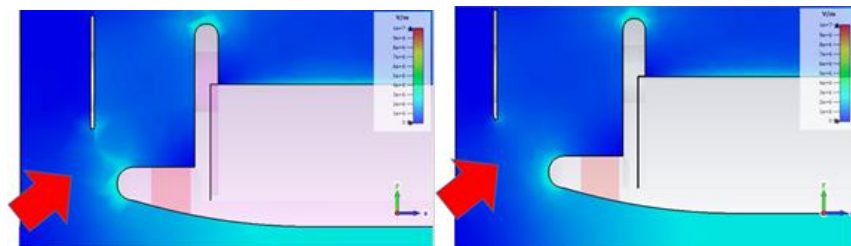


Figure 22: False color of electric field magnitude of a lateral cross section focusing on Rogowski profile tip for the present 130 keV CEBAF (top) and proposed 200 keV upgrade (bottom) Wien filters.

The electrostatic simulations also allowed the identification of locations on the electrodes that could be prone to field emission when increasing the operating voltage of the device, so additional tests using CST Studio Particle Tracking module were performed in order to study the trajectories of electrons generated from these locations. The previously used Solidworks 3D model of the Wien filter upgrade was imported into the Particle Tracking module. After assigning materials to the corresponding assembly parts as described in the previous section, a potential was defined on each electrode plate at -20 kV (top) and +20 kV (bottom). A homogeneous magnetic field of 13 mT, corresponding to the value that preserves the Wien condition, was produced in the simulation volume. The launch locations of field emitted electrons were selected based on the electrostatic results: cusp of the mounting tab, the tip of the Rogowski profile, the top of the rib that runs along the electrode plate, and the bottom surface of the negatively biased plate. The number of emitted particles was defined arbitrarily.

As shown in Figure 23 electrons emitted from the cusp of the negatively biased mounting tab follow trajectories towards the magnetic mirror, mounting spring and vacuum chamber surface at a maximum of 20 keV. Electrons emitted from the back rib of the negatively biased electrode strike mostly the top of the vacuum chamber. And electrons emitted from the electrode Rogowski profile tip are directed towards the magnetic end plate, where it is noticeable that some might actually traverse the magnetic mirror aperture that leads downstream into the beam line.

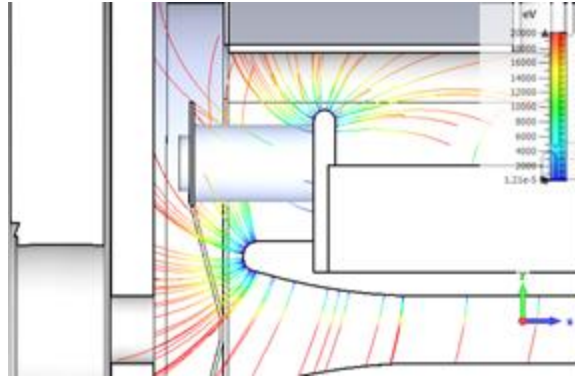


Figure 23: Simulated trajectories of electrons emitted from the mounting tab cusp, Rogowski profile tip, plate strong back rib, and electrode bottom surface. Color gradient corresponds to energy in eV. The electrode plates are biased at ± 20 kV respectively.

These results proved to be useful while diagnosing the vacuum response of the experimental tests discussed in section 3.5. Moreover, those motivated the exploration of additional possible sources for the unexpected vacuum behavior. A previously unnoticed factor was identified, in which an assumption was made about the assembly bolts and washers that held the electrode plates in place by attaching the mounting tabs to the insulators, leading to their removal from the initial simulations. These parts were included in subsequent simulations, and three material possibilities were explored: (i) all metal bolts and washers, (ii) insulator washers with metal bolts, and (iii) all insulator bolts and washers. The left side of Figure 24 shows that at the operating bias of 20 kV, compatible with 200 keV energy beam, the metallic surface of washers remains well below the defined limits for electric field at ~ 1 mV/m, and the bolts show ~ 3.2 MV/m for case (i). Nevertheless, for the case of insulator washers and metal bolts results show that the bolt heads surpass the desired limit of 7MV/m, reaching ~ 11 MV/m. The combination of insulator bolts and washers of case (iii) reduce the electric fields around relevant surfaces below 0.5 MV/m.

The later result was encouraging and implemented experimentally, as described in section 3.6.

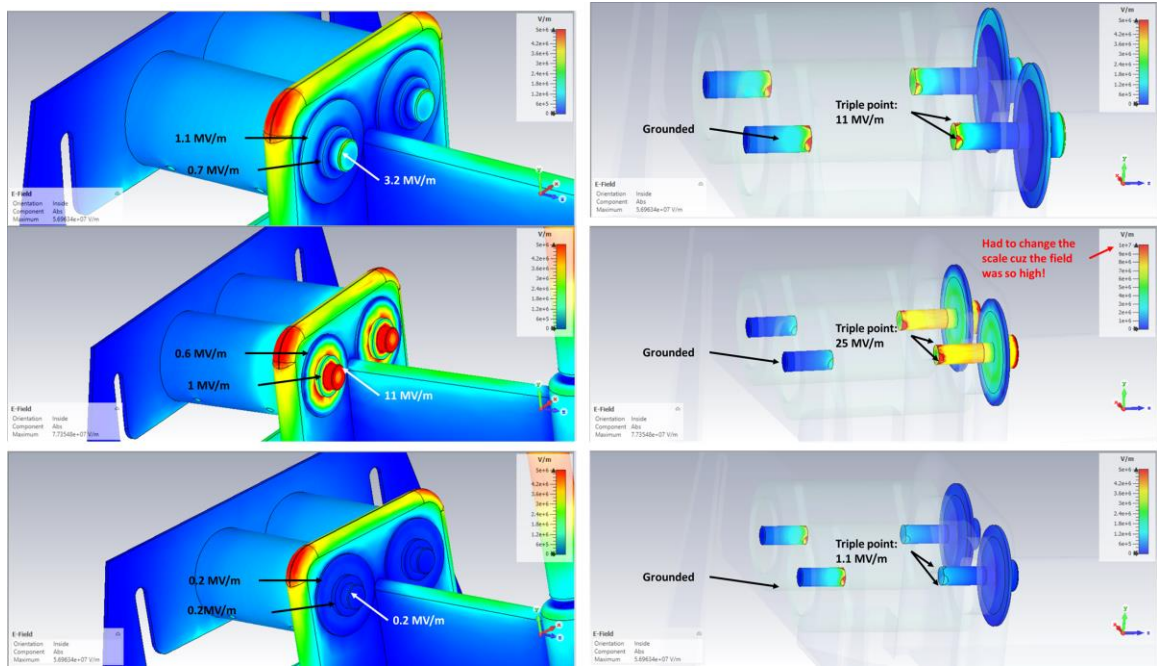


Figure 24: False color surface electric field plots of the mounting setup, showing the mounting spring-insulator-mounting tab assembly (left side), and the same assembly with transparent mounting spring and insulators. The image shows all metal (top), insulator and metal (middle), and all insulating (bottom) fixing material simulation results. The electrode plates are biased at ± 20 kV respectively.

An additional point of interest was located at the region where bolts intersect the cylindrical perforation on the insulators, so-called “venting holes”, used to evacuate the bolt-insulator interface. The perforations that meet the bolts acquire relevance not only for

its triple-point junction characteristics but also because the location and orientation combined with high electric fields (~ 10 MV/m) sets up the conditions for the initiation of surface flashover [23] and further ionization phenomena that could explain the presence of discharge-like vacuum response in our initial HV experimental tests. Simulation results shown on the right side of Figure 24 that at the triple point inside the venting holes cases (i) and (ii) surpass the desired 10 MV/m limit, while case (iii) remains one order of magnitude below it as expected.

Since the device has to be subjected to multiple 200 degree Celsius “vacuum baking” processes to promote water desorption before operation (and thus improve vacuum), a secondary issue arises in the selection of the material for holding components. Due to the different thermal expansion characteristics of the plate body (steel) and MACOR mounting insulators, two additional options to lower the high field gradient regions were considered. Regarding the mounting tab cusp, simulations show that doubling the thickness would reduce the electric field magnitude on its edge surface by 31 % as shown in Figure 25.

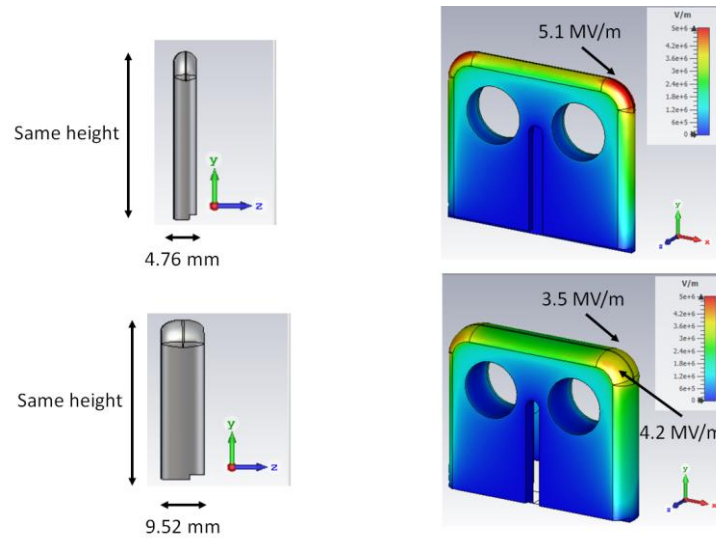


Figure 25: Lateral view of mounting tab showing thickness (left). False color surface electric field isometric view of mounting tab (right) with original (top) and double thickness (bottom). The electrode plates are biased at ± 20 kV respectively.

Additional simulations were implemented to explore the effect of reducing the electrode-electrode gap to lower the field on the aforementioned relevant locations, since smaller gaps allow the device to produce the same spin rotation while operating the electrodes at a lower voltage. In order to produce these simulations, the electrode plate potential corresponding to each gap was calculated per the mathematical framework in Appendix A. 4. Simulation results for 15 mm, 14 mm, and 11 mm electrode gap where the electric field is shown as false color, are compared in Figure 26. The magnitude of the electric field for the HV spring guide cylindrical surface shows a reduction of 13% and 26% for the decreasing gaps. The mounting tab cusp shows a reduction of 11.7% and 27.4%, and the Rogowski profile tip decreases by 11.8% and 23.7% correspondingly.

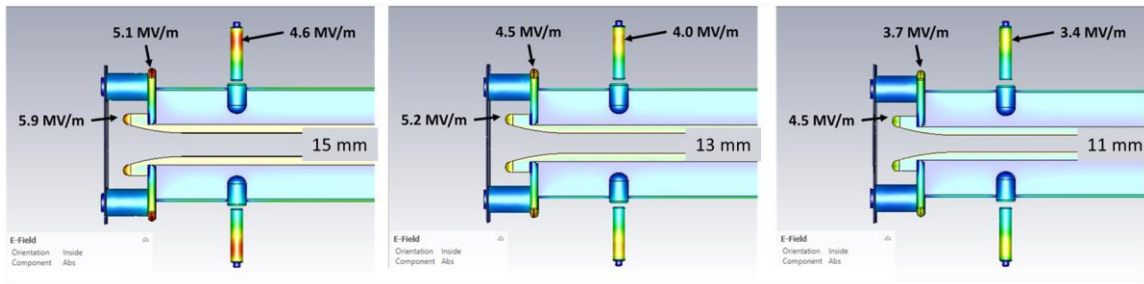


Figure 26: False color electric field plot showing a lateral view of HV electrode plates, insulators and HV spring guides. The plate-plate gaps are 15 mm (left), 13 mm (center), and 11 mm (right).

Yet another alternative that requires no hardware modifications to the device (or can be combined with them) was performed by a simulation where the bias is applied to the HV electrode plates in an asymmetric way, in addition to a reduced electrode-electrode gap (13mm). This produces no changes on the electric field in the homogeneous region of the device compared with the original configuration (and therefore an unmodified spin angle rotation), and allows for the operation of one of the electrodes at a lower voltage, in case it presents imperfections that can result in vacuum degradation. Electrostatic simulations shown in Figure 27 show the values on high curvature regions as usual, where the top electrode was biased at +20 kV and the bottom plate electrode at -15 kV, producing the necessary 2.7 MV/m for the 13 mm gap. To ensure the compatibility of these modifications with adequate beam transport, beam dynamics simulations were performed and are described in the following section.

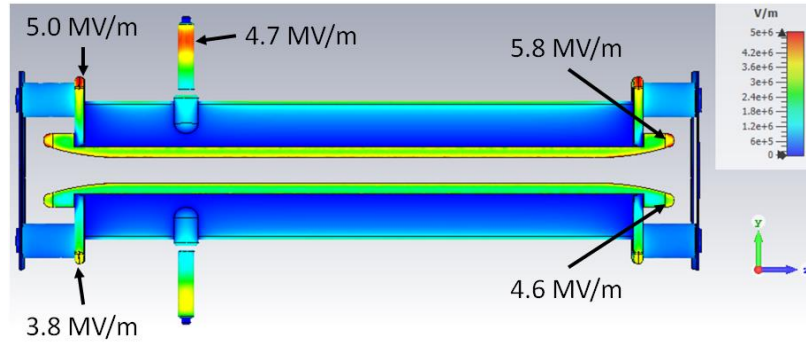


Figure 27: False color electric field plot showing a lateral view of HV electrode plates, insulators and HV spring guides. The image shows the plates biased asymmetrical with the top plate at +20 kV and the bottom plate at -15 kV.

3. 4. 2 Beam dynamics

GPT is a group of codes that solve the system of ordinary differential equations given by the equations in Appendix A. 2 in three dimensions that describe the motion of charged particles in the presence of external electromagnetic fields. In order to do so, it uses a 5th Order Runge-Kutta mathematical method. The software is comprised of four main files: an *.ini file that contains the main code, an *.mr file that contains variables and multiple- run information, field maps in *.gdf format that contain coordinates and the corresponding values of the field component at the specific locations, and a batch file that runs the solvers.

The main code contains a configuration section, where technical details about accuracy and time step size are defined. It also includes a section with the characteristics that define the beam used for the simulations, which in this case is a Gaussian distribution of electrons for the gun. However, for the Wien filter a propagation-resultant distribution must be used since it is located a few meters downstream of the electron gun. This is

achieved by simulating the beam interactions as it traverses the different steering and focusing elements located along the beam path, which produces a distribution file with information about the particle locations, as well as energies. This was produced independently and provided for its use in the corresponding simulation. An additional section of the *.ini file is used to load the previously obtained field maps into GPT. It is relevant to mention that these field map files must possess a defined structure where the coordinates and field components are separated into columns, properly defined by a column header. In the case where multiple files are loaded, it is important that the two files share the same coordinate structure, step size and dimensions. The field map files must be converted to GPT native (*.gdf) format using a batch file that calls the “ascitogdf” GPT routine before being loaded.

After the main code is executed, GPT creates a *.gdf solution file that must be further processed to produce relevant output files. This is achieved by using a batch file to call a different set of GPT codes. For example: GDFTrans for trajectories, GDFa for emittances, or GDF2a to convert solution files into worksheet type files. After the main code produces all solution files, the data must be processed and analyzed. The GDF2a routine is used to convert GPT solution files into *.csv or *.txt files for further processing and visualization using Python or Excel. The following are the relevant parameters for our experiments obtained from GPT along with a brief description:

- Transverse vertical and horizontal average beam position: For the electron gun, it has been reported [6] and further confirmed by our simulations [26] that a relevant vertical deflection on the beam path is present in the existing -130 kV photogun design and further exacerbated by the introduction of the electrostatic shield. This

is due to the asymmetry introduced by the inverted gun design itself and by the height and length of the shield. Therefore, it is relevant to characterize the deviation by analyzing the vertical average beam position. For the Wien filter, it is reported in the literature that a vertical deviation exists in the current design [12], [4]. Therefore, beam dynamics simulation tools were implemented to explore the deviation due to the asymmetric Lorentz force and its relevance in the implementation of the proposed changes to upgrade it for 200 keV beam energy.

- Beam spot size: In both the electron gun and the Wien filter regions, the beam envelope (beam size along the beam path) were analyzed as these are related to beam quality loss and beam scraping on vessel walls.
- Transverse vertical and horizontal normalized beam emittance: This is a particularly relevant beam dynamics parameter for beam transport in the injector, which is a measure of the electron bunch volume in 3-dimensional phase space and thus is a good measure for the dispersion of the particles [Buon 1993], since to maintain good beam quality, phase space dilution must be kept to a minimum. The energy normalized emittance was used in these simulations, since it remains constant unless dissipative processes exist [Wiedeman 2015]. GPT handles beam dynamics through position and momentum coordinates, so the statistical definition of emittance, also known as the root mean square (rms) emittance, was used.
- Average beam kinetic energy and energy spread: For the Wien filter, it has been reported that a change in kinetic energy is present in the current device even when theoretical values of the electromagnetic fields are used that were produced with ideality assumptions regarding perfect overlap of the electric and magnetic fields

[9]. Therefore, a study of the variation in kinetic energy as the electron beam traverses the device is needed to provide a more complete description of the device on beam dynamics.

- Electron bunch length: As the electrons experience acceleration or deceleration in both the electron gun and the Wien filter, the “head” of the electron bunch has a different energy than the “tail”, thus “stretching” or “compressing” each electron bunch. Beam dynamics effects related to kinetic energy variations inside the Wien filter were also explored with simulations.

3. 4. 2. 1 Electron gun

As the electron beam traverses the cathode anode gap, the interaction of electrons with the electric field results in trajectory modifications due to the Lorentz force. Since the net effect of the force is a function of time, position, and beam parameters, for a simple model CST EM Studio particle tracking module was used to simulate single electrons launching from five positions along a vertical axis on the surface of the photocathode face with null initial kinetic energy for the three models: existing CEBAF design, first iteration and second iteration. As shown in the Figure 28 insert, the launch positions correspond to $y = 0, \pm 2 \text{ mm}, \pm 4 \text{ mm}$. Simulated beam position monitors (BPMs) were located at a distance of 39.54 cm (referred to as BPM201) and 90.74 cm (BPM203) along the z-direction from the photocathode face, which correspond to the physical experiment instrument locations. Then the electron position was recorded as it traverses the location of the simulated BPMs and plotted as a dot in (Figure 29).

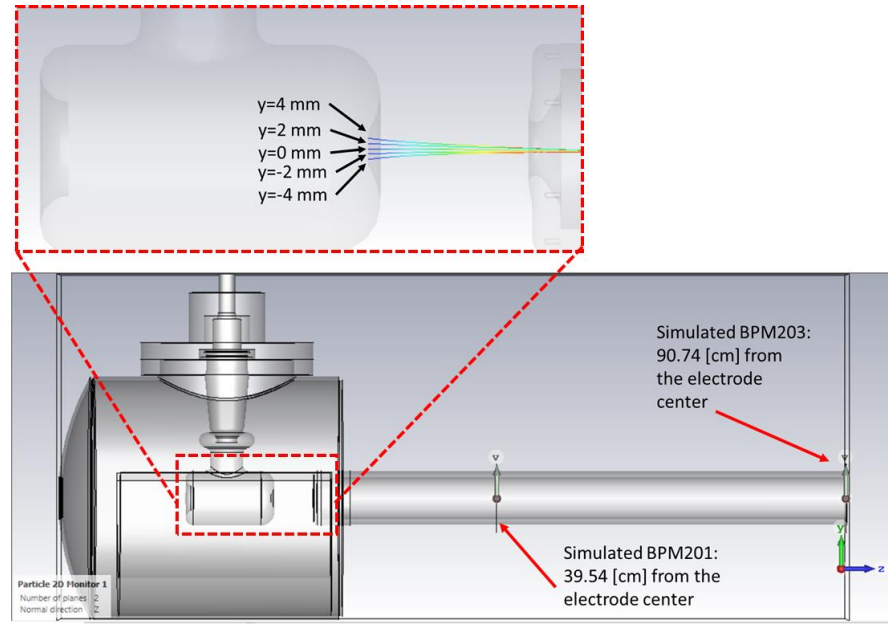


Figure 28: Location of the first and second beam position monitors used in the simulation. The inset shows an example of electron launch positions along the vertical axis on the photocathode surface.

It is relevant to mention that these simulations were conducted in the absence of trajectory and focus correcting devices implemented in the physical machine, the reason being that the focus of these tests are to characterize the intrinsic beam deflection, which can later be used to infer the necessary parameters to correct the deviation. Another relevant result identified by these simplified simulations was that in the absence of trajectory correction and focusing devices, the second BPM would not provide useful information, as the beam trajectory deviation exceeds the BPM limits.

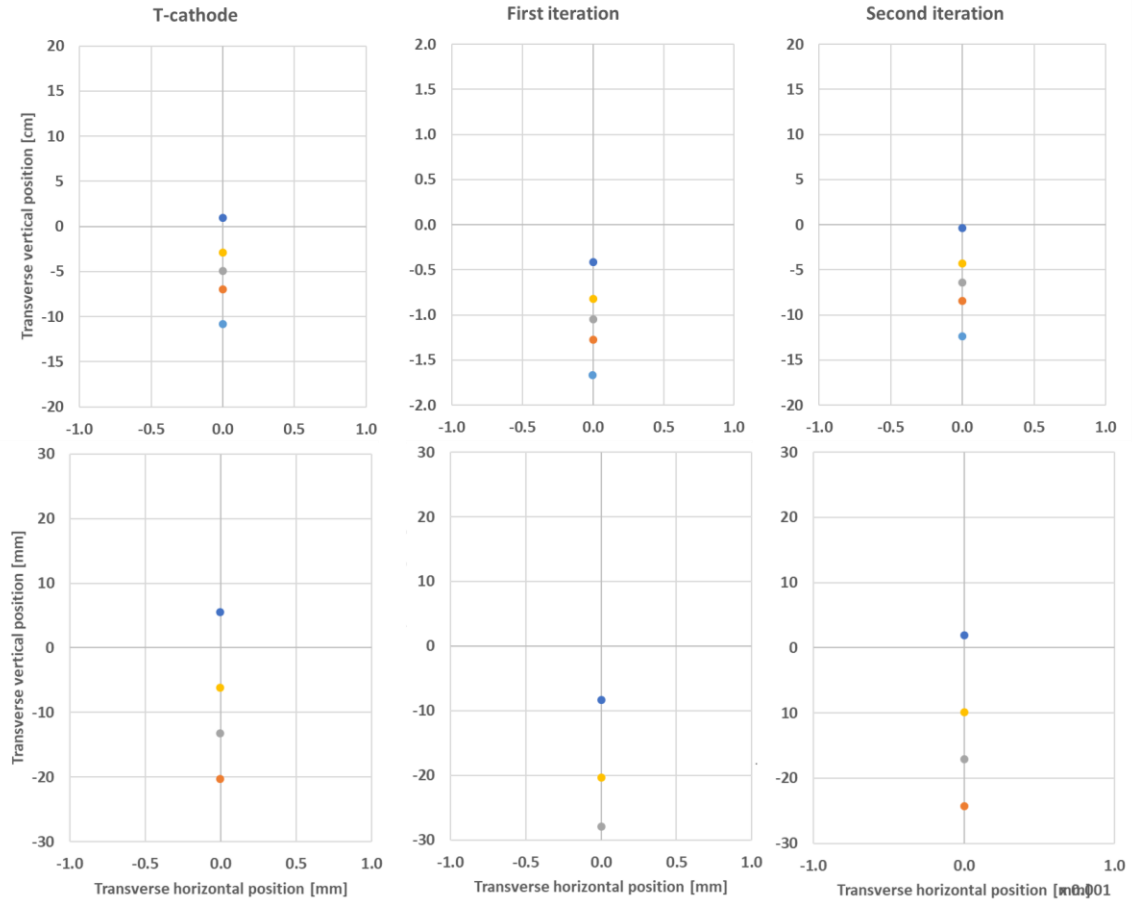


Figure 29: Simulated position of individual electrons on the first (top) and second (bottom) beam position monitors (BPMs). The color code corresponds to each launch position on the vertical axis of the photocathode surface, being $y=2$ mm (orange), 0 mm (gray), -2 mm (yellow), and -4 mm (blue).

For this simple model, the trajectory deviations for single electrons were compared against the original T-cathode design and are shown in Table 1 and Table 2 as factorial increase. The cells that show a ‘-’ symbol indicate that the particle trajectory is lost due to impact with the beamline walls.

Table 1: Trajectory deviation factor at first beam position monitor.

Position on vertical axis [mm]	First iteration	Second iteration
-4	4.22	0.35
-2	2.83	1.47
0	2.12	1.29
2	1.82	1.21
4	1.54	1.14

Table 2 : Trajectory deviation factor at second beam position monitor.

Position on vertical axis [mm]	First iteration	Second iteration
-4	1.51	0.34
-2	3.30	1.60
0	2.11	1.29
2	-	1.19
4	-	-

It is clear that the first and second iteration cathode shield models, even in the absence of collective beam effects, worsen the vertical deviation of the electron trajectory, as discussed in section 2.1. Nevertheless, these results show an advantage of implementing the second iteration model, as the impact on particle trajectory is significantly less than

with the first iteration, while considering that it is the focus of this research to maintain the cathode geometrical features that positively impact field emission.

Additionally, for the $y=0, \pm 2$ mm launch positions, the full single-particle trajectories were traced and compared for three cathode models. Figure 30 shows that at the anode position (represented by the red dotted line), the second iteration design impact in the vertical trajectory deflection is $\sim 16\%$ stronger compared to the T-cathode for the three vertical-axis launch locations, again significantly decreasing the observed effect introduced by the first iteration model.

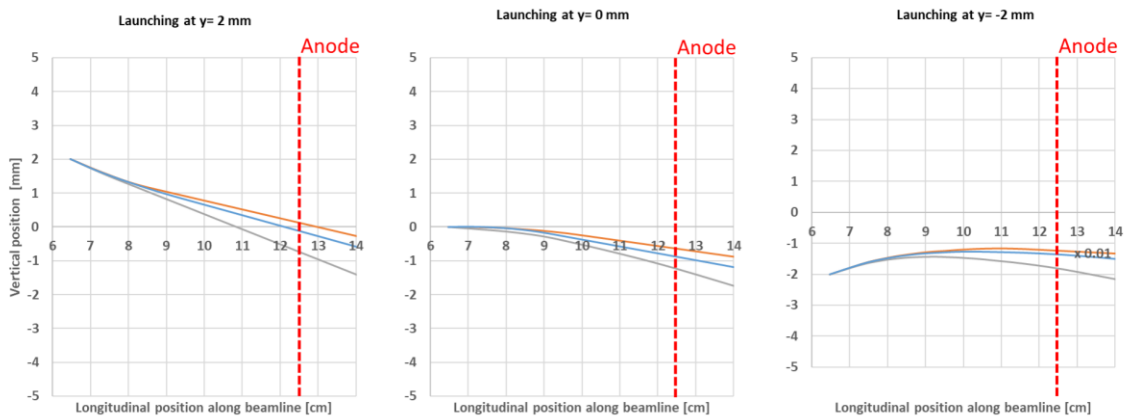


Figure 30: Simulated trajectories of individual electrons from three launch locations along the vertical axis on the photocathode surface: (left) $y= -2$ mm, (middle) $y=0$, and (right) $y= 2$ mm. The color code corresponds to the (orange) existing CEBAF T-cathode, (gray) First iteration, and (blue) second iteration of shielded cathodes.

In order to include realistic parameters that closely resemble those used in the machine and thus capture a more realistic effect on beam trajectory, GPT was used to produce beam dynamics simulations, in which an initial electron distribution with initial

energy $E_0 = 0.195 \text{ eV}$, mean transverse energy $MTE = 0.130 \text{ eV}$, and an initial emittance $\varepsilon_{xy} = 0.1790 \text{ um}$ was used. A Gaussian particle distribution was produced centered at the photocathode face origin and radius $xy_{rms} = 0.32 \text{ mm}$, with a bunch length of 50 ps and a charge of -12 pC . As the simulations are produced, the initial particle distribution is left to interact with the 3-dimensional electric field map generated in the previous sections and corresponding to each of the three models respectively. Subsequently, the data files produced by the simulations were post processed and plotted. The figures of merit are the average particle position, beam spot size, and normalized emittance.

Figure 31 shows the average vertical position resulting from the beam dynamics simulations, where the vertical deflection at the anode location is increased by $\sim 54\%$ for the first iteration model and $\sim 23\%$ for the second iteration model, showing the impact of using the realistic beam characteristics and demonstrating the improvement of the second iteration model. It is relevant to mention that the source of discrepancy with the single-electron model lies in the inclusion of a full beam description included by the use of GPT.

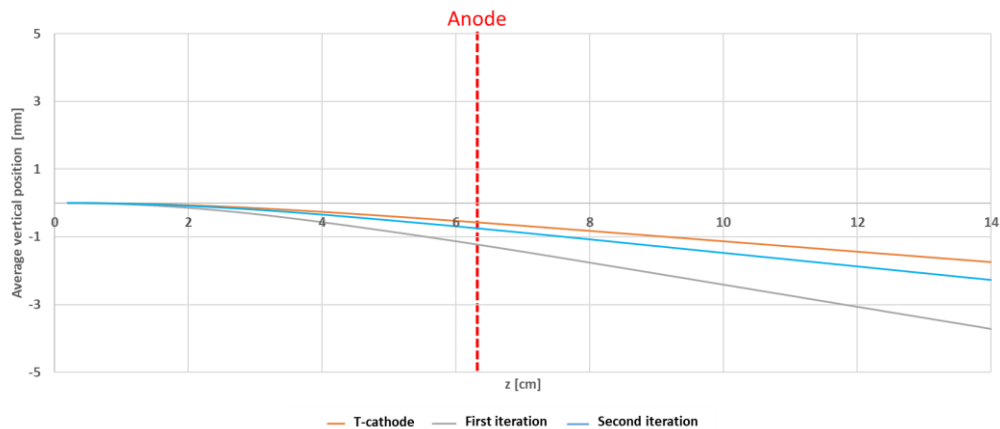


Figure 31: Transverse vertical average beam position results of beam dynamics simulations. The color code corresponds to existing T-cathode (orange), first iteration model (gray), and second iteration (blue).

Another metric for beam quality is the emittance normalized to beam energy, which is a measure of the increase in phase space volume of the electron bunches that comprise the beam. It is relevant for our experiments to ensure that any modifications to the cathode geometry do not introduce an increase in the emittance at the exit of the injector beyond an empirical limit of 20%. It is shown in Figure 32 that according to our simulations the changes introduced by adding the electrostatic shield in the second iteration model increase the present model emittance value by $\sim 9\%$ in comparison to an increase of $\sim 36\%$ for the first iteration model. The results also show that the implementation of the second iteration model introduces an increase in spot size of $\sim 4\%$ in comparison to a $\sim 19\%$ increase due to the first iteration larger electrostatic shield. Internal communications within the Injector group already report difficulties at correcting the electron beam trajectory for the first iteration design, even at a lower energy of 130 keV, requiring the use of beam deflectors to their maximum capacities and making the process of trajectory restoring cumbersome.

Even though operators have not found these undesired effects while producing a beam with the second iteration model, further studies are in needed to fully characterize the deviation as a function of correction parameters.

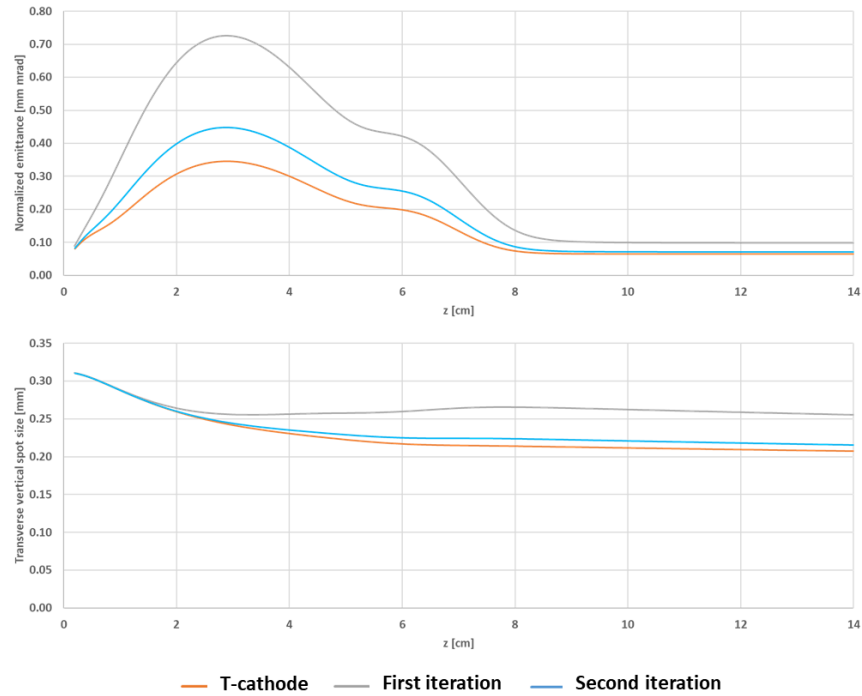


Figure 32: Beam dynamics simulation results of normalized transverse emittance (top) and spot size growth (bottom). The color code corresponds to the (orange) existing CEBAF T-cathode, (gray) First iteration, and (green) second iteration of shielded cathodes.

The trajectory deviation, emittance and spot size growth are better understood by the coupling of the transverse vertical Lorentz force exacerbated by the implementation of the electrostatic shield, and the longitudinal force induced by the Pierce geometry which is designed to produce an electrostatic field that accelerates the electrons away from the

photocathode surface and into the beam line, as shown in Figure 33. It is relevant to notice that the emittance growth in the $0\text{ cm} < z < 6\text{ cm}$ interval is an artifact of the computational method used by GPT [25] due to the coupling of transverse and longitudinal forces. Nevertheless, the value obtained after the coupling vanishes reflects the proper dynamics.

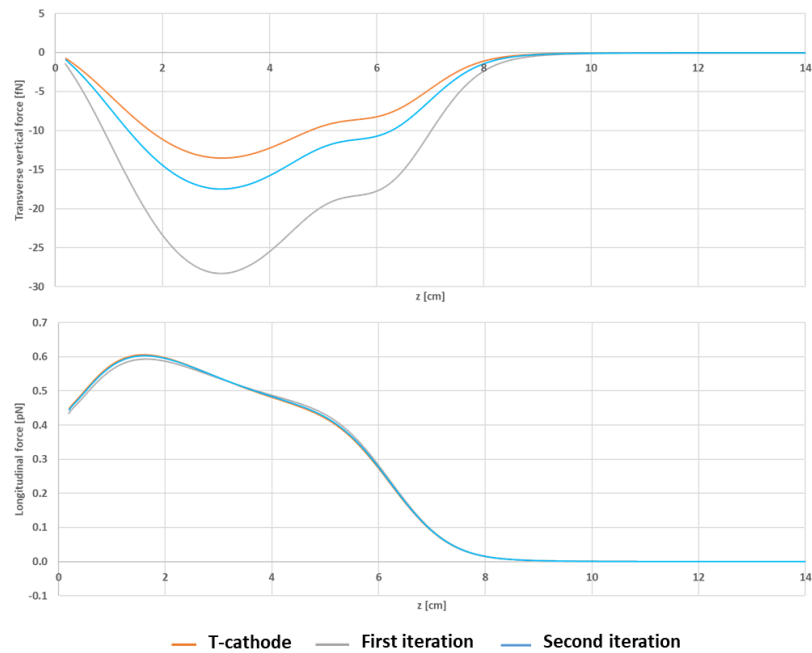


Figure 33: Transverse vertical (top) and longitudinal (bottom) electrostatic forces.

An additional simulation was performed in order to obtain data to cross compare with the trajectory deviation experimental results, in which the previously described electron distribution was used in combination with the field maps in absence of trajectory and focusing correction devices to produce readings of average vertical location as a proxy

for the beam position monitor (BPM) located at 39.5 cm from the photocathode face. The simulation was produced by setting the particle emission center at locations along the vertical axis on the photocathode face corresponding to $-6 \text{ mm} < y < 6 \text{ mm}$ in steps of 1 mm. The average vertical position readings by the simulated BPM were plotted as a function of emission location in Figure 34. These results show that as expected, the presence of the electrostatic shield increases the beam vertical deviation by $\sim 23\%$, compared to the deviation introduced by the existing T-cathode. The validation of these results is further discussed in section 3.7.

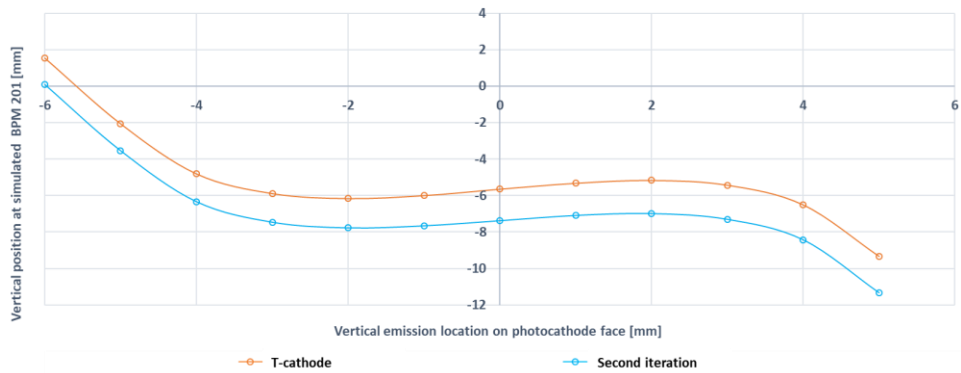


Figure 34: Vertical position readings at a simulated BPM at 39.5 cm from the photocathode face for the existing CEBAF (orange) and second iteration (blue) models.

3. 4. 2. 2 Wien filter

The Pulsar Physics General Particle Tracer (GPT) [25] software was employed to analyze the impact of the proposed modifications on the dynamics of an electron bunch as it traverses the electromagnetic fields inside the device. The 3D electric and magnetic field files are read independently by GPT. Two files were obtained from the electrostatic and magnetostatic simulation results using the post processing tools, one containing the electric

field components (E_x , E_y , E_z) and a separate file containing the magnetic field components (B_x , B_y , B_z). For each one, the values of the fields must be obtained at the same spatial coordinates (x , y , z). The files generated for the existing CEBAF 130 keV Wien filter were produced independently using Opera [31] and used as benchmarks. Then the electric field was simulated with CST EM Studio for the upgrade 200 keV Wien filter. In all cases, the fields were obtained in a 0.8 cm X 0.8 cm X 50.0 cm box with an interpolation step size of 0.1 cm.

For the existing 130 keV the corresponding values of electric and magnetic fields that hold the equilibrium condition and produce a 100° spin rotation were calculated using the theoretical framework described in Appendix A.4 and are listed in

Table 3. These values are obtained by assuming ideal conditions such as equal effective lengths and perfect overlap between the profile of electric and magnetic fields on the device's central axis. These values were used to obtain the potential per plate parameters to set up the electromagnetic field simulations. An initial beam dynamics simulation test aimed at researching the absence of proper beam transmission along the device when the theoretical values for the electromagnetic fields were used, and it was produced using a test electron beam generated with a 1000 electron Gaussian distribution with 250 micron rms transverse profile and a 20 ps rms bunch length. Results show that interaction with the electromagnetic field configuration for the 130 keV filter results in a beam trajectory deviation along the transverse vertical direction, due to non-zero net force arising from $\frac{E}{B} < v$ at the outermost region of the fringe field and $\frac{E}{B} > v$ at the innermost

region, concurring with the observations reported in [4], [9], and [12]. As shown in Figure 35, using the theoretical field values results in an asymmetric total force (green trace) that deviates the beam trajectory in the vertical direction as the electrons traverse the entry fringe field region near $z = -0.20$ m. Moreover, as the beam propagates, the kinetic energy increases due to the non-zero net force; thus, the “kick” is exacerbated along the device until the beam reaches the exit fringe region; at this time, the total force contribution is not enough to allow the trajectory to recover.

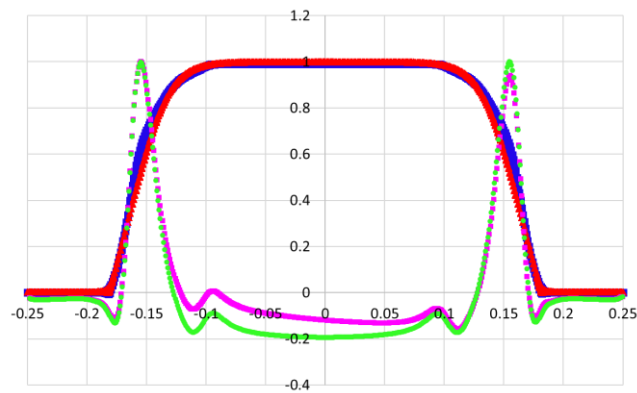


Figure 35: Simulated electric (blue) and magnetic (red) fields. The theoretical values of the electric field result in an asymmetric total force (purple), while reducing the electric field restores its symmetry (green). All plots are normalized to their maximum values.

During the 130 keV Wien filter beam optics optimization phase it was found empirically that while maintaining the magnetic field unmodified, a reduction of the theoretical electric field by $\sim 0.95\%$ succeeded in restoring the beam trajectory by

symmetrizing the total force (shown in Figure 35 as a green trace), thus compensating for the change in kinetic energy introduced by the coupling between the transverse and longitudinal forces resulting from the fringe region asymmetry. The re-symmetrized force is shown in Figure 35 as a purple trace.

After benchmarking the existing 130 keV Wien filter, beam dynamics simulations were performed for the 200 keV upgrade. In order to simulate an electron beam with parameters closer to those in the actual injector, thus improving the result quality, the beam parameters file at the Wien filter entry aperture was obtained using a Gaussian distribution of 867 particles with 250 micron rms transverse profile and 22 ps rms longitudinal profile. The file was produced independently by a member of the Injector Group dedicated to produce so-called “lattice” simulations. In order to do so, the initial particle distribution is propagated through simulated upstream trajectory correction and focusing elements until it reaches the location of the Wien filter. At this point, the file is created with the resulting particle distribution spatial coordinates (x , y , z) and corresponding momenta (p_x , p_y , p_z). Subsequently, this file was imported as an input to GPT. The magnetic field file from the baseline simulation was scaled to obtain the corresponding 13 mT at the plateau. The electric field was simulated per the theoretical value using CST, then reduced by $\sim 1.1\%$ in order to restore the beam trajectory. The corresponding parameters are shown in

Table 3.

Table 3: Electric and magnetic field magnitudes needed for $\pi/2 + 10\%$ maximum spin rotation for the present injector energy (130 keV) and for the upgrade injector energy (200 keV).

	130 KeV	200 keV
$ \mathbf{E} $ MV/m	1.6	2.7
$ \mathbf{B} $ mT	9.1	13

A comparison between the beam dynamics simulation results of the 200 keV upgrade and 130 keV existing Wien filters is shown in Figure 36, following the digest shown in [4] where the average position of the electron beam along the vertical axis (a) shows a difference of 23.4% in the vertical trajectory deflection at the center of the device. The normalized transverse emittance (b) shows a 47% increase (at the device center) by implementing the proposed upgrade, yet it recovers to the original value at the exit aperture. As expected, the non-zero net force results in a change in the average kinetic energy (c) that increases inside the device but has a net zero change in both cases. There is a 10% decrease in the net vertical spot size (d) for the upgrade, which corresponds to a focusing, while results show a net defocusing of 21% for the existing Wien model. The bunch length (e) increased as the beam traverses the device, about 0.7% for both cases. The energy spread (f) shows a reduction of $\sim 81\%$ for the proposed upgrade. The results show that the existing Wien filter can successfully operate with the desired 200 keV energy beam to provide 100° spin rotation by operating at 62.9% higher bias and 42.8% stronger magnetic

field and implementing the modifications described in section 3.3: 40 kV rated HV feedthroughs, longer MACOR mounting insulators, and modified HV spring guide contacts. The increase in vertical beam deflection at the higher 200keV beam energy, one of our main interests due to the possibility of beam scraping, is expected to be manageable, as the maximum deflection of ~ 1.5 mm at the device center remains well below the 7.5 mm limit imposed by the 15 mm electrode-electrode gap. The behavior of the normalized emittance, kinetic energy, and bunch length show no significant variation respect to the present 130 keV design, which is encouraging. Nevertheless, these results, in combination with the decrease observed in the spot size and energy spread, will undergo validation as part of injector commission phase at Jefferson Lab.

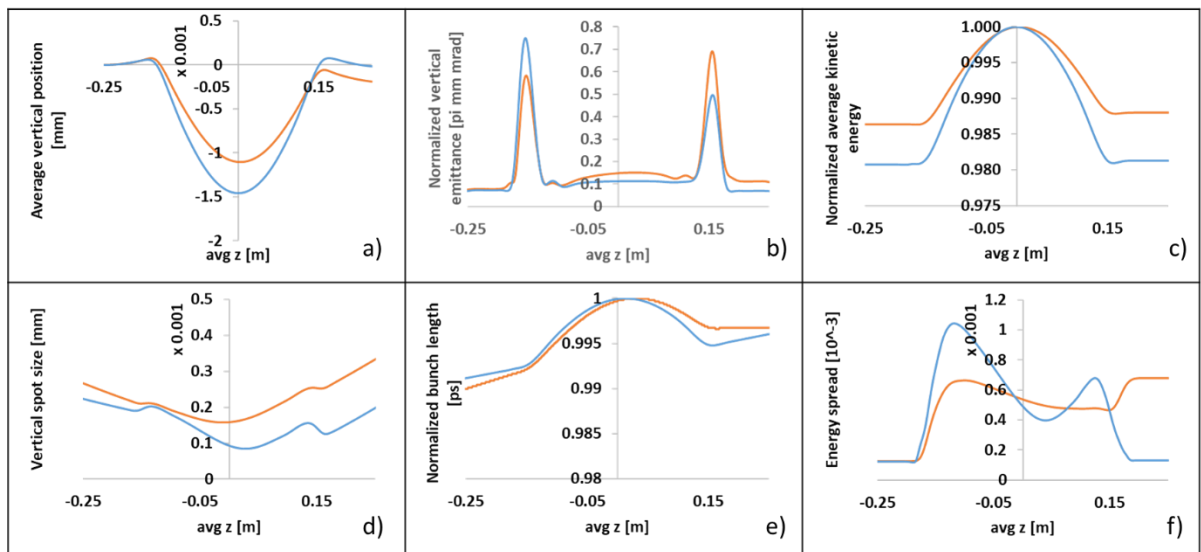


Figure 36: Beam dynamics GPT results for the 130 keV CEBAF (orange) and 200 keV upgrade (blue). Based on the great digest shown in [4].

The electrode gap reduction electrostatic simulations shown in section 3.4 required analysis of the resulting beam dynamics in order to ensure proper device operation. The combined effects of gap, beam vertical deflection and spot size were analyzed to determine whether those remain within the beam envelope limits that reduce the risk of beam scraping the electrode plates or magnetic mirror apertures. Moreover, the emittance and bunch length results provide information that could be subjected to verification in future experiments. The electric field map for each case was imported along with its corresponding magnetic field map as in the previous case, where the magnitude values that preserve the Wien condition at the device's middle region were obtained per the theoretical framework in Appendix A.4 and are shown in Table 4. The particle distribution utilized is the same as in the previous section, resulting from the propagation of an initial distribution along the beam line instruments to the Wien filter entrance.

Table 4: Voltage per plate values corresponding to each inter-plate gap distance, calculated using the theoretical framework described in Appendix A. 4.

Electrode distance gap [mm]	Voltage per plate [kV]
15	20.2
13	17.5
11	14.8

The results of GPT beam dynamics simulations are shown in Figure 37, corresponding to the three electrode-electrode gap dimensions, namely 15 mm, 13 mm, and 14 mm. The transverse vertical beam deflection (a) shows a ~45% reduction between

the 15 mm and 13 mm cases, and a ~85% absolute reduction between the 15 mm and the 11 mm gaps, with a change in the deviation direction. The change in normalized emittance (b) is negligible (<1%) for the three gap distances at the device exit. The average kinetic energy shows a decrease of ~0.8% between the 15 mm and 13 mm, and a decrease of ~2.2% between 15 mm and 11 mm gaps. There is a net focusing effect on spot size (d) of ~10% for all models, showing negligible variation between them. The beam bunch length (e) shows a negligible difference between models, with a 0.4% reduction for the three cases when comparing the entrance and exit regions of the device. Finally, results show a negligible energy spread (f) between models at the device exit region. Even though the electrode gap modifications were not part of the final implementation, they represented relevant considerations during the decision making process, in addition to working as viable alternatives in case field emission or vacuum instabilities prevent the operation of the electrodes at the desired voltage, since it allows us to obtain the same spin rotation and considerably similar beam dynamics, while applying lower voltage to the electrodes.

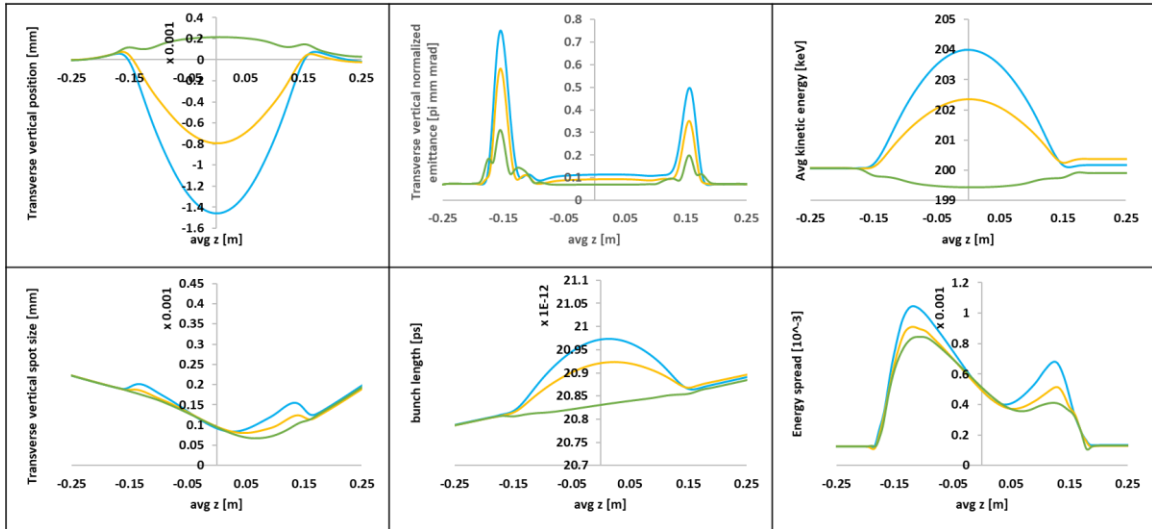


Figure 37: Beam dynamics GPT results for the 200 keV proposed upgrade for 15 mm (blue), 13 mm (yellow), and 11 mm (green) gaps. Based on the digest shown in [4].

Finally, the beam dynamics results for the asymmetrically biased electrode plates shown also in section 3.4 were also obtained. As described in the electrostatic simulation section, an asymmetric bias of +20 kV and -15 kV was set on each of the high voltage electrode plates with a gap distance of 13 mm. The resulting electric field map was obtained with CST and then imported along the corresponding magnetic field map (properly scaled) into GPT. The electron distribution that comprises the beam is the same as in the two previous cases. As previously discussed, the test was designed to provide yet another alternative to device operation, in the eventuality that one of the electrode plates was unable to operate at the maximum voltage.

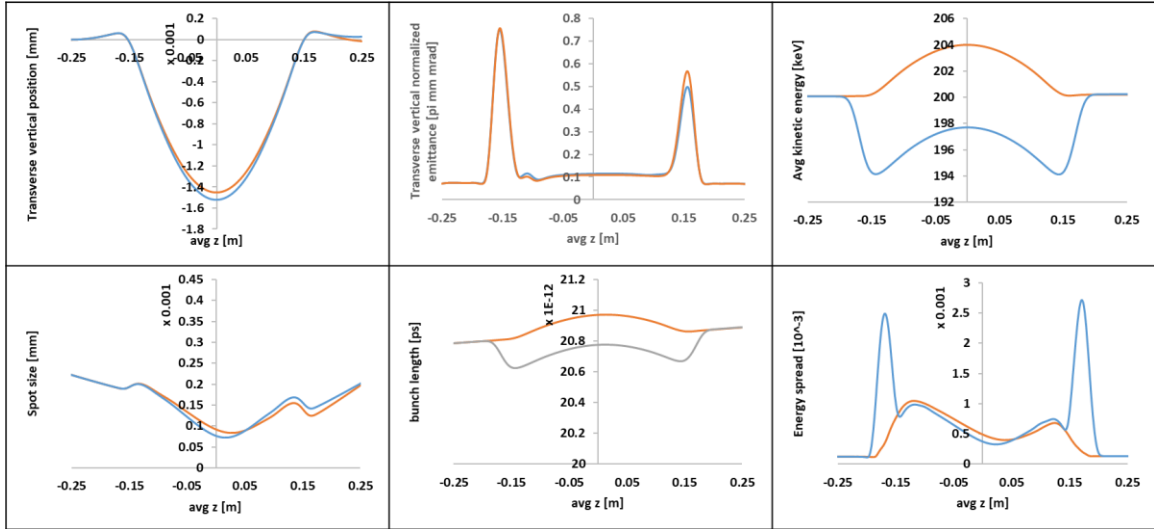


Figure 38: Beam dynamics GPT results for the 200 keV proposed upgrade for symmetric bias (orange), and asymmetric bias (blue). Based on the digest shown in [4].

The results show clear differences in bunch length, kinetic energy and energy spread behavior at the central axis of the device, yet the net effect (i.e. comparing the entry and exit points of the device) is negligible in these cases. Moreover, the spot size shows no significant variation, and the transverse vertical deflection shows an increase of 4.5% when applying an asymmetric bias, which is again well below the device geometrical limits of 6.5 mm due to the 13 mm electrode-electrode gap. These final results proved to be the more viable option in case one of the electrodes perturbs the vacuum conditions.

3.5 Hardware implementation

Based on conclusions from the simulations for both electron gun and Wien filter, new components or component modifications were acquired from vendors or fabricated by the Jefferson Lab machine shop. An intermediate step in close collaboration with the

Design Department was necessary due to the previously mentioned defeaturing process, in which geometrical features irrelevant to the electrostatics were removed and must be re-introduced in order to produce construction drawings. The finished metallic parts were polished to a mirror-like finish to minimize the likelihood of field emission related to surface imperfections. A process referred to as “tumbler polishing” was used, in which the parts were placed inside a plastic cylinder in the presence of a polishing agent (i.e. corn cob or abrasive cones) [27]. The cylinder was then fixed inside a tumbler machine which rotates the cylinder and the components inside it around an axis for approximately 1 hour. The new mounting insulators, 0.004 m longer than those used in the Wien 130 keV version, were machined out from MACOR. The electrodes and all new internal components were cleaned in an ultrasonic bath of concentrated degreaser diluted in distilled, deionized water for ~1 hour and then thoroughly rinsed in distilled, deionized water. The Wien filter test setup was assembled in a cleanroom class 1000 following the respective protocols (i.e. gloved hands, previously cleaned tools and fasteners in ultrasonic bath using diluted Micro-90 degreaser followed by rinse by de-ionized water and 2-propanol, cleaning of working surfaces using 2-propanol and lint-free disposable towels, sticky mat at clean room entrance). Two 11 l/s ion pumps were attached to each end by means of vacuum crosses fitted with borosilicate viewports. One of the crosses was connected to a turbo pumping station. After vacuum was established, a leak checking process was performed with a residual gas analyzer (RGA). As gaseous helium was dispersed methodically around the vacuum chamber, the RGA spectrum was closely observed for He (4 amu) peaks that would indicate helium entering the vacuum chamber. Once vacuum integrity was assured, the assembly was baked at 200° C for ~36 hrs. This process is performed to allow for

desorption of water from the metallic surfaces, in order to further improve the vacuum and reach ultra-high vacuum conditions of $\sim 10^{-9}$ Torr after cooling off to room temperature, necessary to mitigate field emission. Then, one of the high voltage feedthroughs was connected to a positive 30kV DC, 1 mA power supply while the opposite feedthrough was connected to a similar power supply but with negative bias.

The Wien filter magnetic coil was made of 26 turns of #13 square wire and enclosed between the vacuum chamber and the steel shell. The coil was powered with a variable +/- 15 A DC power supply. Additionally, two Geiger-Mueller LM712 tube radiation detectors from LND, Inc. were placed on each end of the Wien filter setup on the external side of the borosilicate viewports. The devices were monitored through the Experimental Physics and Industrial Control System (EPICS) [28] in an independent, shielded control room. At this point, the high voltage characterization process may begin. The implemented cathode electrode with electrostatic shield, and the upgraded Wien filter are shown in Figure 39.



Figure 39: -200 kV photoelectron gun cathode electrodes with electrostatic shield. The first iteration (top left), second iteration (top right), and 200 keV Wien filter (bottom).

To obtain data to validate the simulations of electron beam deviation, an additional set of experimental runs was performed. The cathode electrode was installed in the photogun vacuum chamber, the system was vacuum-baked following a similar protocol to that described for the Wien filter. Once it had cooled down to room temperature and vacuum characterized, it was high voltage processed. Then a photocathode was activated and installed. Separated from the electron gun vacuum chamber with a mechanically operated isolation valve, an adjacent vapor deposition chamber with an internal carousel holds a series of molybdenum pucks to which a III-V GaAs wafer is affixed using indium foil and covered with a tantalum cup that is pinched in place using tweezers. The deposition

chamber holds a cesium (Cs) source that is fed externally by an independent power supply. An oxidizer source (NF₃) is connected to a leak valve to allow for controlled flow of the gas to the vacuum chamber. An ohmic heating rod is located at the bottom of the chamber and used to desorb surface contaminants from the semiconductor surface. To produce high electron yield per incident photon (quantum efficiency or QE) the GaAs photocathode surface must be activated to negative electron affinity through a process of intermittent deposition of Cs and the oxidizer. As the process is carried, a 780 nm laser is shined on the wafer surface through a quartz window, and the photocurrent produced is measured by means of a picoammeter connected in series with an anode ring located inside the chamber. Once the process is completed, the photocathode is transported to the electron gun vacuum chamber by mechanic manipulators. The activated photocathode is placed inside the cathode electrode, where an internal structure of sapphire rollers and leaf springs presses the molybdenum puck in place, exposing only the photocathode surface to the cathode-anode gap. During beam production, the photoelectron gun is isolated from the deposition chamber. The voltage, current, radiation monitors, and a 780 nm drive laser are controlled and monitored through EPICS in an adjacent radiation-shielded control room equipped with operational safety systems. In order to produce the electron beam, and having previously cleared all safety protocols, the laser beam passes through remote controlled Pockels cells to “chop” the continuous wave beam into 250 micro-second long pulses at a rate of 2 Hz. This configuration is called Viewer Limited mode, producing low average current beam thus preventing the beam viewer phosphor screen saturation and potential damage to the instrumentation or the beamline walls. As the electron beam is produced, beamline trajectory correction and focusing magnets are normally configured to produce a

beam trajectory centered on every BPM and focusing element, but as this test is designed to study the uncorrected beam trajectory to assess deviation, the solenoid focusing elements were in the off state. The path of the electron beam is monitored remotely through two beam position monitors located downstream from the source. This process was repeated for the T-cathode and the second iteration cathode electrode. In the following section the procedure to obtain the relevant data and its processing is described in detail.

3. 6 High voltage characterization

In both the photoelectron gun and the Wien filter, the device was monitored and controlled remotely via the EPICS interface. The applied high voltage in the cathode electrode and the Wien filter electrode plates was monitored separately. The vacuum chamber pressure was obtained by monitoring the current draw on the ion pump power supplies, as vacuum pressure vessel volume is related to electrical current generated by ionized residual gas in the ion pump electrodes. Geiger-Müller tube radiation monitors located around the Wien filter vacuum chamber and electron gun vacuum chamber were used to monitor radiation coming from each device in counts per second. All signals were monitored in real time with strip tools on the screen and automatically registered and stored in files.

The metallic electrodes must be conditioned in order to operate at the designed bias without field emission. Imperfections on the metal surfaces due to inadequate polishing, material defects or even unwanted particulate material during assembly can result in field emission (Appendix A.5). This phenomena manifests as vacuum degradation, resulting from desorption of gas from the device surfaces by the emitted electrons or by ionization

of residual gas species in the vacuum chamber, and it is correlated to the presence of radiation if the emitted electrons are energetic enough to create x-rays that penetrate the device's metallic shell. Without careful control of these processes, cascading effects further exacerbate the undesired conditions inside the vacuum chamber to the point of power supply over-current trip or even device catastrophic failure. Therefore, the voltage is slowly increased while carefully monitoring all signals, and depending on the nature of the response, the voltage is further increased or left to soak for hours. The response of field emitter burn out varies, but in general it shows a very distinctive signal footprint, in which vacuum increases with radiation response, and then suddenly decreases to background levels together with radiation levels. These vacuum spikes and radiation monitor response set the conditions for HV processing.

The process is completely equivalent in the case of the electron gun as with the Wien filter, with the difference that each plate is HV processed separately by keeping the opposed plate at ground bias. Then both electrode plates are processed together by incrementing the bias voltage in both at the same time. In both cases, after achieving operational voltage +10%, the device is left to soak for days. Upon successful high voltage characterization, the device is deemed fully functional and ready to use.

Multiple instances of HV processing were performed during the multi-year program, for each cathode electrode (T-cathode, first and second iterations) and for the Wien filter. As an example, Figure 40 (top) shows a screen capture of the EPICS monitor during HV processing the second iteration of the shielded cathode electrode. From top to bottom, it is noticeable that as the high voltage (first trace) increases, the current drawn from the power supply (second trace) shows spikes correlated with the presence of

radiation response from the monitors (third to seventh traces) even presenting power supply overcurrent trips. Similarly, Figure 40 (bottom) shows the processing of the Wien filter with both electrode plates biased (first and second traces) and the subsequent vacuum response recorded by the current monitors on the ion pumps (third and fourth traces). In this case the response from the radiation monitors (fifth and sixth traces) shows background level readings, as the x-rays produced are not energetic enough to penetrate the metallic vacuum chamber.

Naturally, the EPICS output is not optimal for assessing differences between results, so all the data captured must be selected and post processed in order to provide an intelligible comparison of device performance, as presented in the following section.

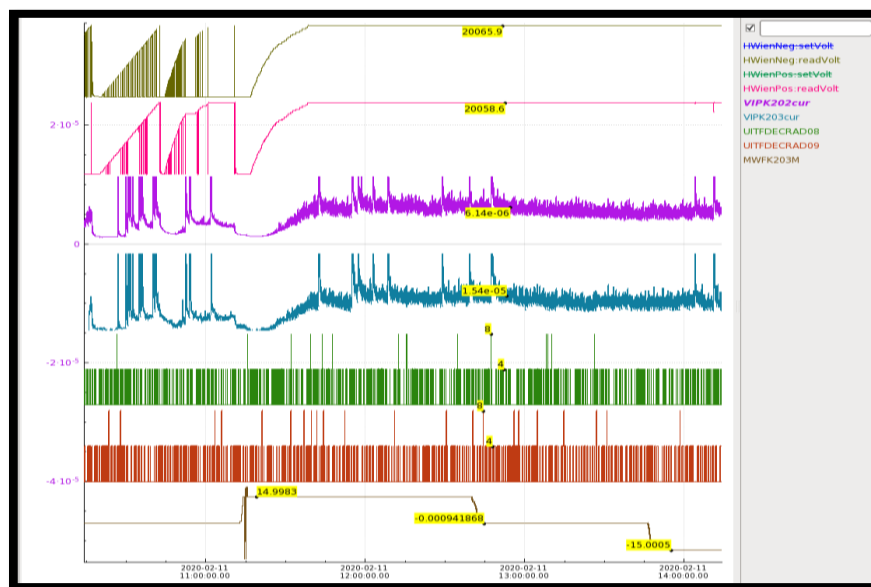
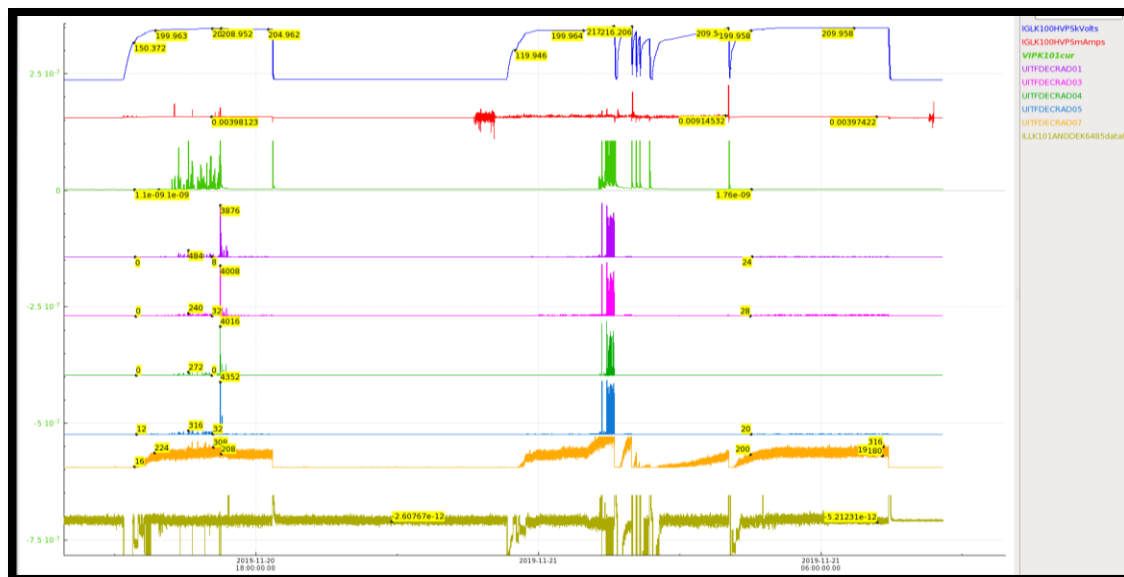


Figure 40: Example of HV characterization of cathode electrode (top) and Wien filter (bottom) showing raw epics monitor. On the top figure the relevant signals are the first and second trace show the cathode bias voltage and the power supply current draw. The third to seventh traces show radiation monitor response. On the bottom figure the relevant traces are the first and second showing the bias voltage applied to the electrode plates, the third and fourth showing ion pump current response, and the fifth and sixth showing radiation monitor response.

3. 7 Data processing and analysis

The iterative nature of the experiments requires intermediate data processing and analysis steps, where the information learned in a previous step was used as input for modifications to the next iteration until the final device design was reached or for troubleshooting. The methodology developed as a result of this dissertation work created a “paper trail” that provided relevant information to verify or troubleshoot each design iteration and created a database of results that can be improved in the future. Excel was also used for typical data processing or when the number of tests was small. Programmed Excel sheets enabled the creation of visualization plots of the EM interpolation results on specific device regions such as the insulator interface, cathode anode gap, Wien filter electrode-electrode gap, GPT statistics visualization, and EPICS log files (see Figure 16, Figure 18, Figure 29 - Figure 38).

Some of the tests produced large amounts of data that needed to be processed, so Python code was implemented to efficiently manipulate them. For the electron gun HV processing it is relevant to produce condition history plots that show the accumulated time for a cathode to be deemed ready for beam operations, ideally free of measurable field emission. In these experiments the radiation monitor response is correlated with field emission, as the emitted electrons impact the walls of the vacuum chamber, thus producing x-rays through the process of bremsstrahlung. In order to produce visualization plots, large sections of data were removed when the photogun high voltage power supply tripped off due to over-current surpassing the manually set limit, or when high voltage processing was paused overnight. This was achieved in the Jupyter Lab runtime environment by converting the data files to a database format that is handled with Python-3 Pandas library. Then pairs

of data points corresponding to subsequent time steps are compared to one another to verify whether the photogun power supply tripped (or was turned on); in such a case a marker was created on the data that allowed the location of data points and their use as inputs in the code to cut-and-stitch data sets, automatically generating the proper plots with file names and axis titles. Figure 41 shows a high voltage conditioning history of the CEBAF 130 kV T-cathode electrode produced with this method, in which the presence of field emission in a series of power supply trips required the use of a more aggressive approach, in which krypton gas was leaked into the vacuum chamber, allowing the cathode to withstand higher bias voltages [33]. The resulting processed plot shows that after 20 accumulated hours of processing (1200 minutes), the photogun cathode electrode still presented some field emission.

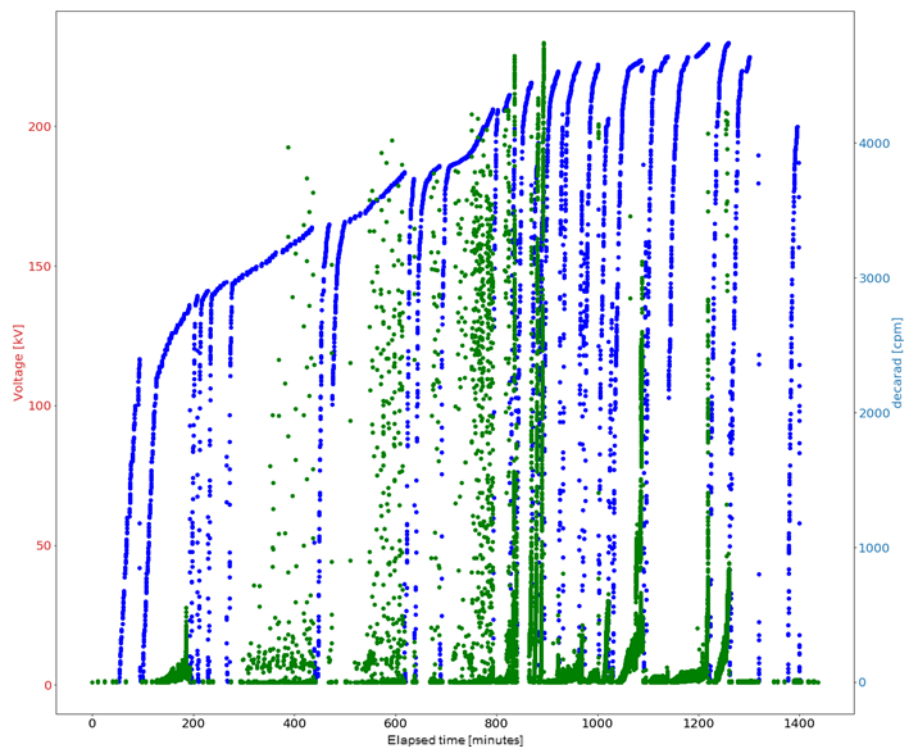


Figure 41: High voltage conditioning history (Elapsed time in minutes) of CEBAF 130 kV T-cathode electrode showing bias voltage (blue), and the signal from one of the Geiger-Müller x-ray monitors near the photogun (green).

It is difficult to make an exact comparison in high voltage performance between cathode electrodes due to external factors that can alter the time it takes for processing and the conditioning voltage required to achieve the target operational voltage without field emission. For example, variations in material properties, polishing methods and assembly can result in undesired dust particulates or nanometer size scratches that lead to field emission and are difficult to process out during high voltage conditioning. The HV processing results for the second iteration cathode electrode are shown in Figure 42 after it was first installed in an experimental testbed accelerator, in which krypton processing was also performed, in order to optimize readiness time. It is worth noting that to ensure the

systematization of the experiments, the results shown in Figure 41 and Figure 42 were performed at the same experimental testbed, and the shown signals were obtained from the same power supply and the same radiation detector for both cathodes. Figure 42 shows the successful processing of the second iteration cathode electrode after 29 accumulated hours (1750 minutes). This is an encouraging result, although more experiments are needed to conclusively relate the performance to the cathode geometric modifications and many instances of processing should be performed in order to provide enough statistical data to compare the performance of both cathodes.

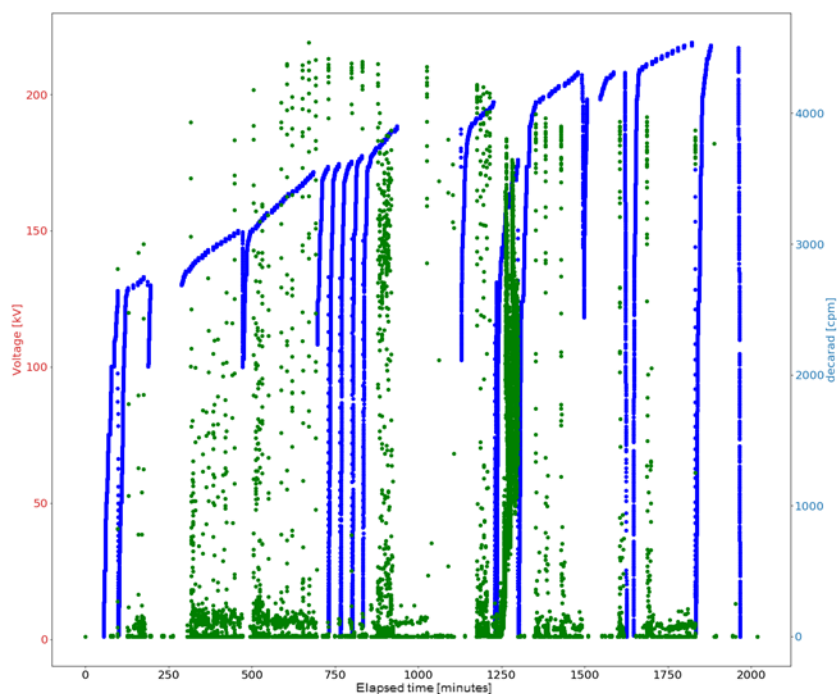


Figure 42: High voltage conditioning history (Elapsed time in minutes) of the second iteration electrode with triple-point-junction shield showing bias voltage (blue), and the signal from one of the Geiger-Müller x-ray monitors near the photogun (green).

In the Wien filter case, a similar code was used which filtered unwanted data from the EPICS files and can combine the results of two different HV processing files (corresponding to each electrode plate) in order to analyze the behavior of both electrode plates as a system. Figure 43 shows the behavior of a preliminary test in which even after processing both electrode plates, the vacuum level showed a significant increase. A series of experimental tests was produced with the objective of isolating the origin of the response, in combination with simulations described in section 3.4 to allow for proper device operation in the occurrence of faulty electrode plates. Upon disassembly of the device, visual inspection identified welding and surface imperfections as possible sources of vacuum instability and low level field emission. As mentioned in section 3.3, the original high voltage electrodes were designed as an assembly of multiple parts brazed together. Moreover, the Rogowski profile consisted of a series of flat plates of increasing lengths resulting in a faceted profile that required further surface finishing by hand polishing. Based on the electrostatic simulations, new high voltage electrodes were designed with a smooth spline transition profile and were manufactured from single-piece stainless steel slabs. Subsequently, the new electrodes were tumbler-polished substituting the manual, labor-intensive process previously used. The new parts were thoroughly cleaned per the process discussed above prior to device re-assembly. Bias voltage was applied first to one of the electrodes while maintaining the opposite electrode at ground potential. Then the test was repeated with the opposite electrode (Figure 44 left). Subsequently, both electrodes were biased at the same time but with opposite polarities and the vacuum response recorded Figure 44 (right). In contrast with the vacuum response to applied voltage shown in Figures 43 and 44, the lack of vacuum activity with applied voltage shown in Figure 44 is a direct

benefit of the proposed implementations derived from the simulations, satisfactorily concluding the contributions of this work to the CEBAF Wien filter upgrade design, implementation and testing.

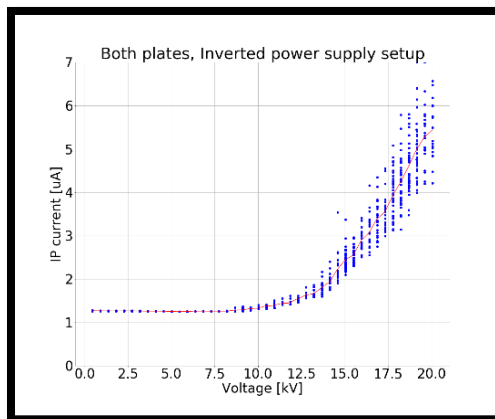


Figure 43: Example of a HV characterization of the Wien filter vacuum response as a function of applied voltage at both electrode plates at unison.

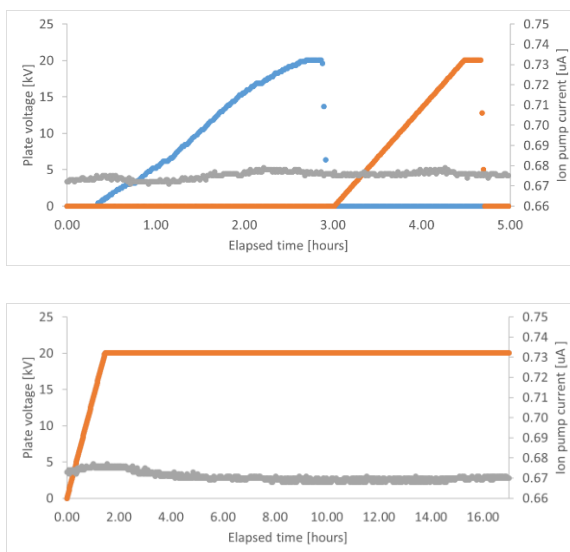


Figure 44: Wien filter HV characterization after device re-assembly. As each plate is energized by keeping the opposite plate at ground (left), and as both electrode plates are biased together (right), the device presents practically no vacuum degradation.

Finally, beam-based measurements were necessary to understand the beam deflection in the cathode-anode gap and to validate the electrostatic simulations shown in section 3.4. An additional set of experimental runs was performed in order to obtain data for the deviation of the electron beam. One process to measure beam deflection consists of propagating low average beam current with the laser train pulses set to Viewer Limited (VL) mode (described in section 3.4) from the photocathode along the keV (low energy) beam line to a beam dump without correcting for the trajectory. In this manner, the intrinsic beam deflection induced by the asymmetric anode-cathode geometry was studied using two BPMs located on the beam line at 39.54 cm (BPM201) and 90.74 cm (BPM203) downstream of the photocathode surface for measuring the beam position as the position of the laser was scanned along the horizontal and vertical axis lines on the photocathode surface. In preparation for the experiment, the BPMs linear response region, beyond which current saturation on the device produces unreliable position readings, was verified for both BPMs. An electron beam in VL mode was produced and its trajectory scanned along the horizontal and vertical axis of the second BPM by means of varying the current applied to horizontal and vertical steering magnetic dipoles located on the beam line. Due to the location of the steering coils, it was only possible to scan the full response range for BPM203. Then it was assumed that the region is the same as the BPM201, since the manufacturing is identical. Figure 45 shows that for both horizontal and vertical directions, the linear response falls in the $[-6\text{mm}, 6\text{mm}]$ interval for BPM203, so the readings from BPM203 and BPM201 are reliable in this interval.

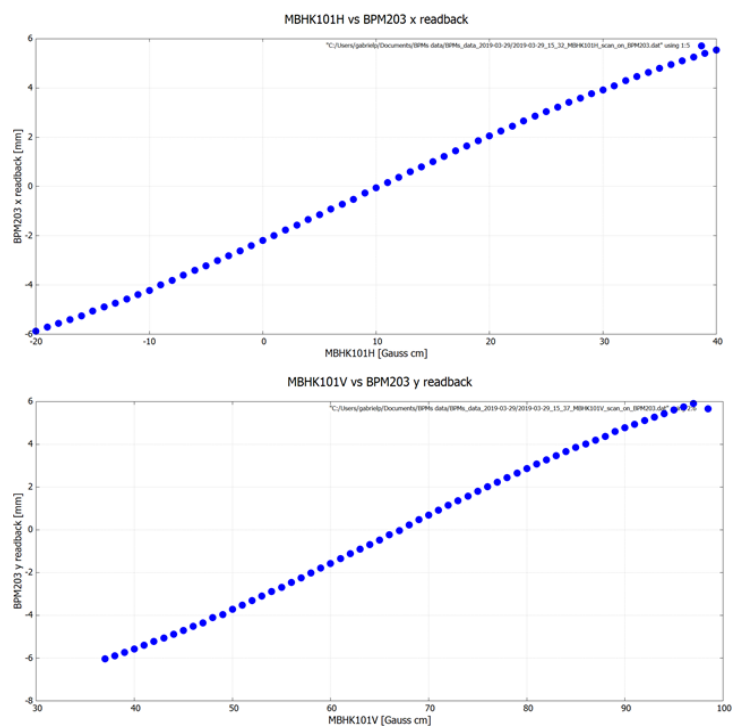


Figure 45: Beam position readings from a BPM located at 90.74 cm from the photocathode surface as a function of magnetic field strength.

After the linear response region was verified, the beam position was measured at the closest beam position monitor (BPM201), but in this case, the location of the incident laser (used to produce electron emission) was scanned along the vertical axis on the photocathode surface by means of an XY-stage position controller operated through the graphical user interface (GUI) of EPICS. It is relevant to mention that the second monitor (BPM203) was not used for these experiments since the beam deflection exceeded the monitor response, as predicted by the single-electron simulations described in section 3.4.

Since the objective of this measurement was to address the impact of the cathode shield on the beam trajectory, the experiment was repeated for the existing CEBAF T-cathode and the version with a small shield, referred to before as the second iteration

cathode. Figure 46 shows a comparison between the simulated and the experimental raw data, showing two main results. As previously reported in the literature [6] and as corroborated by the simulation results, the vertical trajectory deflection already existed in the T-cathode design (introduced by the vertical gun inherent asymmetry), and it is exacerbated by the presence of the electrostatic shield as shown before in Figure 34. However, misalignments existing in the physical machine result in exacerbated positional variation. The possible sources of these variations are the uncertainties in the precise locations of the BPMs, laser beam position, and photocathode position with respect to the beamline longitudinal axis.

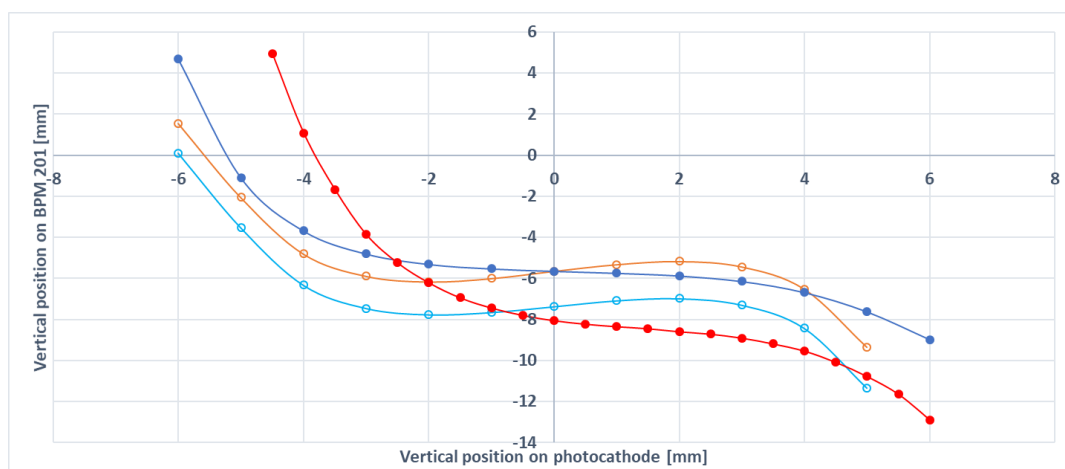


Figure 46: Vertical position on a BPM as a function of beam source position on the photocathode. The t-cathode simulated (orange trace) and raw experimental data (red trace), and the second iteration simulated (turquoise) and raw experimental data (blue trace) are shown.

The variations introduced by taking into account the uncertainties in alignment of the two cathodes must be further studied, but a second experimental data collection run seems unlikely to happen due to time constraints in the laboratory operation schedule. Nevertheless, to elaborate on the mismatch between experimental and simulated results, another set of beam dynamics simulations were produced to explore a parameter space of BPM readings in the presence of misalignments. This was accomplished by introducing offsets to the beam emission location that corresponds to a laser beam position mismatch on the photocathode surface and to the BPM location which corresponds to a relative position mismatch between the BPM, the photocathode and the beam line longitudinal axis. Figure 47 shows the vertical beam position as measured by the BPM for the existing T-cathode. In this case, the original simulated results (orange trace) are graphed along with a 1.5 mm offset (green trace) and a 3 mm offset (black trace) on the emission location, in addition to the experimental raw data (blue trace). It is clear that within the acceptable range of deviations, there is still no match with the experimental results. However, assuming a BPM position mismatch of 2.4 mm in the vertical direction combined with a 1.5 mm photocathode center deviation (red trace), a resemblance is found with the 3 mm simulated offset (black trace).

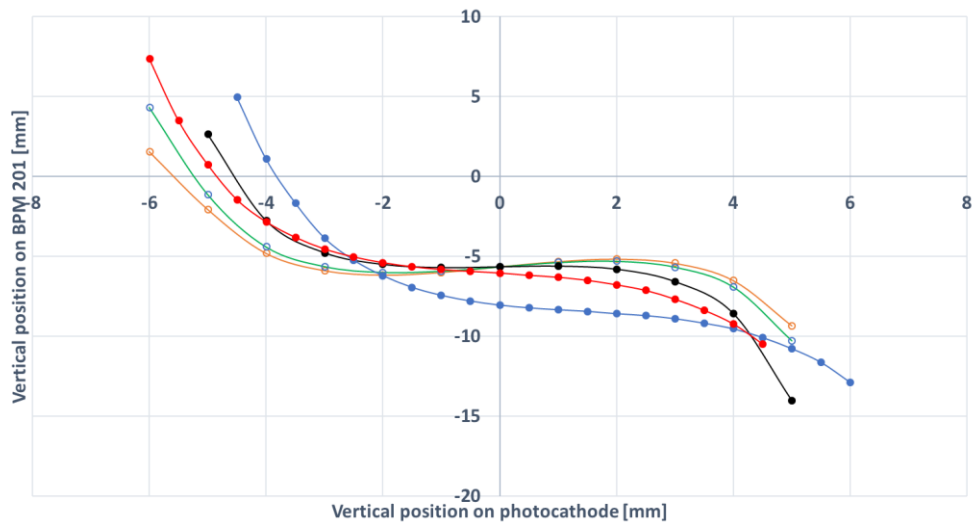


Figure 47: Vertical position on a BPM as a function of beam source position on the photocathode for the t-cathode. Simulated original (orange), 1.5 mm emission location offset (green), 3 mm emission location offset (black), matched offset experimental (red) and raw experimental data (blue) are shown.

Similarly, for the second iteration cathode electrode with a small electrostatic shield, Figure 48 shows the original simulated results (turquoise), and simulated emission location offsets of 1.5 mm offset (green trace) and a 3 mm (black trace), in addition to the experimental raw data (blue trace). For this case, a subtraction of a BPM position mismatch of 1.72 mm in the vertical direction (red trace) was enough to find resemblance with the 3 mm simulated offset (black trace).

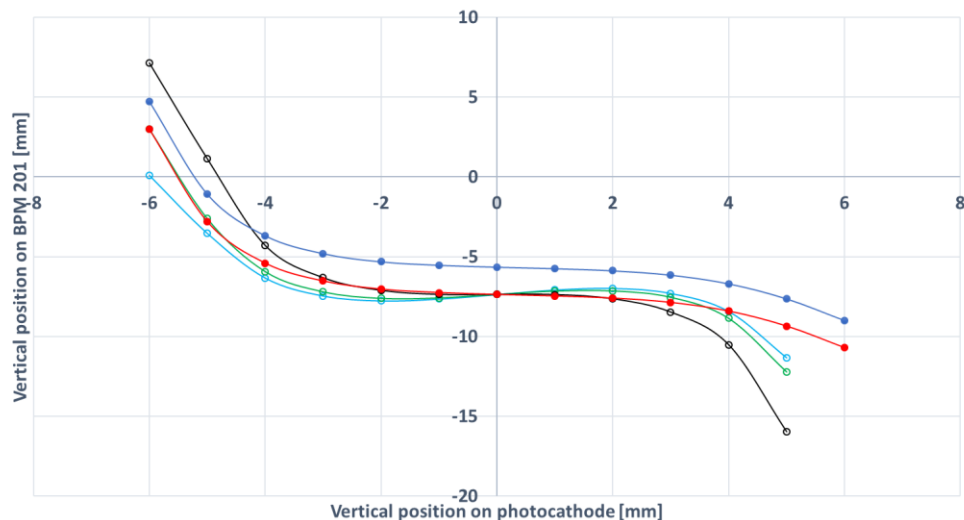


Figure 48: Vertical position on a BPM as a function of beam source position on the photocathode for the second iteration cathode. Simulated original (orange), 1.5 mm emission location offset (green), 3 mm emission location offset (black), matched offset experimental (red) and raw experimental data (blue) are shown.

The simulation results shown in section 3.4 clearly show that in an ideal case, the implementation of the electrostatic shield results in an increment of $\sim 23\%$ in the vertical deviation of the electron beam. The necessity of introducing additional offsets to the experimental data, particularly in the regions $-3 \text{ mm} > x > 3 \text{ mm}$ along the photocathode vertical position where the found agreement deviates, could be related to several factors that pertain to the machine assembly process and could be negatively impacted by the unavoidable removal and reinstallation procedures to test the cathode electrodes. The exploration of such factors could be the object of further studies; however, beam time opportunities during beam operations are scarce as these are highly valuable for the laboratory's experimental agenda. Furthermore, in practice the photocathode surface is rarely completely activated; in turn, a mechanical mask is used during activation that limits

the emission area to subsections of the region where agreement between simulations and experimental data was found.

CHAPTER 4

DISCUSSION AND FUTURE WORK

A methodology was developed to devise solutions for robust operation of the CEBAF polarized photoelectron gun and Wien filter energy upgrades by electrostatic modeling, prototype implementation and experimental characterization. Increasing the operating voltage from nominal -130 kV to -200 kV are expected to aid in providing lower beam emittance, better transmission through injector apertures, and improved photocathode lifetime. The desire to increase the photogun operating voltage led to the design of an electrode with triple-point-junction electrostatic shield which minimizes the electric field at the delicate insulator-metal-vacuum interface and linearizes the potential across the insulator, thus reducing the risk of arcing along the ceramic insulator. After a first design iteration presented an undesired impact in the dynamics of the electron beam [26], improvements motivated by these results led to a second design iteration which proved successful, aiming to reduce the impact on beam trajectory in the cathode-anode gap while preserving the benefits of the previous design.

The photoelectron gun prototype with the devised electrostatic shielding was built and installed at a test bed injector where its high voltage response was successfully characterized, showing a behavior well within established expectations, deemed operational after 1750 minutes with no measurable field emission. A validation procedure of detailed beam dynamics simulations was performed by characterization of the experimental results of 200 keV electron beam deviation as a function of laser beam position on the photocathode surface, in the absence of trajectory and focus correction. Relative agreement was found between simulated and experimental data when introducing

position corrections that could be related to instrumentation and assembly deviations, yet further experiments are needed to establish the exact source of the found discrepancies. Nevertheless, the information obtained during the development of these experiments proved to be useful in determining correction and steering mechanisms for the proposed modification. In praxis, the combined results of this research work resulted in the successful operation of the device, demonstrating nearly 500 hours of polarized beam delivery at the required -200 kV, making it the only polarized photoelectron source in the world to deliver beam at such voltage.

The ongoing development of particle accelerators around the world, such as the Electron Ion Collider (EIC) and the International Linear Collider (ILC), require the production of even higher voltage sources, capable of robust operation for long periods of time, so future work on photoelectron sources is required. These include exploring the material and geometry of insulators that contribute to charge drainage to prevent charge accumulation and linearize the potential even further. Further work in studying the coupling between cathode and anode shapes, spacing and tilt will improve the understanding of electric field heterogeneity in inverted-insulator design photoelectron guns. The development of custom-element codes for the existing beam dynamics simulation software would provide valuable insight in the process of ion-creation and back bombardment, paramount in maintaining the precious semiconductor lifetime. And naturally, advances in semiconductor research are necessary to produce high QE and high polarization photocathodes to withstand the conditions inside the photogun vacuum chamber. Furthermore, materials and practices to achieve extreme-high vacuum such as

surface coatings to reduce outgassing [29] need to be developed to improve photoelectron gun vacuum vessels.

Based on the electrostatic simulation results from this work, the Wien filter upgrade prototype was built. The implementation of the methodology developed in this document allowed for identification of sources of undesired behavior, leading to the successful characterization of the proposed upgrades that allowed the device to operate at the higher voltage specifications. An exploration of solutions that aid in minimizing gradient in field emission prone components were presented, including an exploration in the reduction of the inter-electrode gap, geometry modification of high electric field gradient regions, the impact of material properties of fasteners to the electrostatics, and the asymmetrical application of bias voltage to the individual electrodes. These electrostatic studies, in combination with the detailed beam dynamics results on trajectory deviation and correction, normalized emittance, spot size, and energy spread, provide a valuable and novel addition to the body of knowledge in the operation of Wien filters as spin rotators, so a scientific paper containing the findings of a Wien filter compatible with a 200 keV electron beam is being prepared to be submitted on a peer reviewed journal for publication and is undergoing an internal review process.

The Wien filter design originally from SLAC has proven to be robust and capable of surpassing its operation parameters with modifications, yet its implementation at even higher electron beam energies would require further work on optimization of the high voltage electrodes Rogowski profile and of the magnetic yoke, to reduce fringe region mismatch effects that result in trajectory deviation and beam quality loss. Naturally, vacuum improvement processes and practices would allow the reduction of detrimental

field emission effects. Furthermore, the inclusion of ion-production analysis tools in the beam dynamics simulation would provide a better understanding on phenomena related to photocathode ion back-bombardment and detrimental effects on QE lifetime, paramount for highly demanding parity-violation experiments.

The presented work enabled the operation of the world's first 200keV high polarization photoelectron gun and a Wien filter capable of rotating the spin angle of a 200 keV electron beam to a maximum of 100° . Both instruments not only fulfill the robust operational and beam quality requirements imposed by the CEBAF energy injector upgrade but also build upon widespread use of state-of-the-art polarized photoelectron sources and provide valuable information for the international accelerator community in the face of the increasingly stringent beam requirements for future nuclear physics programs as the EIC [18] and the ILC [17] collaborations.

4. 1 Summary and conclusions

A methodology was developed and implemented to devise solutions for robust operation of the CEBAF polarized photoelectron gun and Wien filter energy upgrades by electrostatic modeling, prototype implementation, experimental characterization, and extensive beam dynamics simulations.

The correlation between the geometry of the triple point shielding electrode and the beam deflection along the cathode-anode gap was found and described. This could be implemented in future optimization algorithms to minimize electron beam deflection and provide the highest operating voltage without field emission and without insulator arcing.

The combined results of this research work resulted in the successful operation of the photoelectron gun demonstrating over 500 hours of polarized beam delivery at the required -200 kV, making it the only polarized photoelectron source in the world to deliver a beam at such voltage.

This work enabled the operation of the world's first 200keV Wien filter, capable of rotating the spin angle of a 200 keV electron beam to a maximum of 100° .

Both instruments not only fulfill the robust operational and beam quality requirements imposed by the CEBAF energy injector upgrade but also build upon widespread use of state-of-the-art polarized photoelectron sources and provide valuable information for the international accelerator community in the face of the increasingly stringent beam requirements for future nuclear physics programs as the EIC and the ILC.

4. 2 Outlook and future work

The completion of this work provides an exciting outlook for future engineering students, as many of the aspects regarding optimization could be improved and further implemented in projects leading to the implementation of even higher-energy polarized electron sources. The information presented in this work could be used to implement evolution algorithms that use specific parameters (i.e. metallic part curvature, maximum surface electric field, and maximum permitted beam deviation) to explore cathode geometries that withstand >300 kV without field emission and minimize beam deflection, and Wien filter spin rotator high voltage plates and magnet coils that improve the overlap of the electric and magnetic field profiles, thus minimizing the impact of these discrepancies on the quality of the electron beam. The results presented in this work also

reveal the necessity of further design modifications in order to achieve the stringent requirements of future nuclear physics experiments, where explorations on insulator geometry and materials are paramount to allow the photoelectron source to achieve even higher energies without breakdown. An extensive dedicated study of in-situ beam production using the upgraded photoelectron source and Wien spin rotator would offer future physics and engineering graduate students a great opportunity to develop their academic careers while providing vital information for the accelerator physics community. Moreover, topics related to the GaAs semiconductor photocathode, material physics regarding alloys used in the construction of cathodes and vacuum chambers, coatings and surface preparation to improve vacuum conditions, as the development of computer codes to monitor and analyze device response, are not only fundamental in accelerator science, but could also have a high impact in the development of scientific and technological advancements that have historically propelled society towards a better future.

4.3 Publications

As part of this research work, the following results have been published in refereed journals and Conference Proceedings:

Electrostatic design and conditioning of a triple point junction shield for a –200 kV DC high voltage photogun. Review of Scientific Instruments 89, 104703 (2018); <https://doi.org/10.1063/1.5048700>. G. Palacios-Serrano, F. Hannon, C. Hernandez-Garcia, M. Poelker, and H. Baumgart.

Compact –300 kV dc inverted insulator photogun with biased anode and alkali-antimonide photocathode. Phys. Rev. Accel. Beams 22, 113401 – Published 13 November 2019. C. Hernandez-Garcia, P. Adderley, B. Bullard, J. Benesch, J. Grames, J. Gubeli, F. Hannon, J. Hansknecht, J. Jordan, R. Kazimi, G. A. Krafft, M. A. Mamun, M. Poelker, M. L. Stutzman, R. Suleiman, M. Tiefenback, Y. Wang, S. Zhang, H. Baumgart, G. Palacios-Serrano, S. Wijethunga, J. Yoskowitz, C. A. Valerio Lizarraga, R. Montoya Soto, and A. Canales Ramos.

New Simulations for Ion-Production and Back-Bombardment in GaAs Photoguns. The 18th International Workshop on Polarized Sources, Targets, and Polarimetry, PSTP201923-27 September, 2019. Knoxville, Tennessee. Josh Yoskowitz, J. Grames, J. Hansknecht, C. Hernandez-Garcia, G. A. Krafft, M. Poelker, R.Suleiman, G. Palacios-Serrano, S. Wijethunga, S. B. Van Der Geer.

Simulation Study of the Emittance Measurements in Magnetized Electron Beam. 10th International Particle Accelerator Conference. Melbourne, Australia (2019). S.A.K. Wijethunga, M.A. Mamun, F.E. Hannon, G.A. Krafft, J. Benesch, S. Zhang, G. Palacios-Serrano, R. Suleiman, M. Poelker, J.R. Delayen.

200 keV Wien filter for the CEBAF 12 GeV update. (Unpublished manuscript.)
2020. G. Palacios-Serrano, P. Adderley, H. Baumgart, J. Benesch, D. Bullard, J. Grames, C. Hernandez-Garcia, A. Hofler, M. Poelker, and M. Stutzman.

REFERENCES

- [1] M. J. Alguard, J. E. Clendenin, R. D. Ehrlich, V. W. Hughes, J. S. Ladish, M. S. Lubell, K. P. Schüllerab, G. Baum, W. Raith, R. H. Miller, W. Lysenko, "*A source of highly polarized electrons at the Stanford Linear Accelerator Center,*" Nucl. Instrum. Methods 163, (1979).
- [2] G.D. Cates, V. W. Hughes, R. Michaels, H. R. Schaefer, T. J. Gay, M. S. Lubell, R. Wilson, G. W. Dodson, K. A. Dow, S. B. Kowalski, K. Isakovich, K. S. Kumar, M. E. Schulze, P.A. Souder, D. H. Kim, "*The bates polarized electron source,*" Nuclear Instruments and Methods in Physics Research Section A: Accelerators, Spectrometers, Detectors and Associated Equipment, Volume 278, Issue 2, 1989, Pages 293-317 ISSN 0168-9002.
- [3] W. Hartmann, D. Conrath, W. Gasteyer, H. J. Gessinger, W. Heil, H. Kessler, L. Koch, E. Reichert, H. G. Andresen, T. Kettner, B. Wagner, J. Ahrens, J. Jethwa, F. P. Schäfer, "*A source of polarized electrons based on photoemission of GaAsP,*" Nuclear Instruments and Methods in Physics Research Section A: Accelerators, Spectrometers, Detectors and Associated Equipment, Volume 286, Issues 1–2, 1990, Pages 1-8, ISSN 0168-9002.
- [4] B. Steiner, W. Ackermann, W. F. O. Muller and T. Weiland, "*Wien filter as a spin rotator at low energy,*" 2007 IEEE Particle Accelerator Conference (PAC), Albuquerque, NM, 2007, pp. 170-172, doi: 10.1109/PAC.2007.4440148.
- [5] C. K. Sinclair, P. A. Adderley, B. M. Dunham, J. C. Hansknecht, P. Hartmann, M. Poelker, J. S. Price, P. M. Rutt, W. J. Schneider, and M. Steigerwald, "*Development of a high average current polarized electron source with long cathode operational lifetime,*" Phys. Rev. ST Accel. Beams 10, 023501 (2007).
- [6] P. A. Adderley, J. Clark, J. Grames, J. Hansknecht, K. Surles-Law, D. Machie, M. Poelker, M. L. Stutzman, and R. Suleiman, "*Load-locked dc high voltage GaAs photogun with an inverted-geometry ceramic insulator,*" Phys. Rev. ST Accel. Beams 13, 010101 (2010).
- [7] William T. Diamond, "*New perspectives in vacuum high voltage insulation. I. The transition to field emission,*" Journal of Vacuum Science & Technology A 16, 707 (1998).
- [8] J. Grames, R. Suleiman, P. A. Adderley, J. Clark, J. Hansknecht, D. Machie, M. Poelker, and M. L. Stutzman, "*Charge and fluence lifetime measurements of a dc high voltage GaAs photogun at high average current,*" Phys. Rev. ST Accel. Beams 14, 043501 (2011).
- [9] K. Tsuno & D. Ioanovicu. Advances in Imaging and Electron Physics 176. Academic Press (2013). ISBN: 978-0-12-408142-0.

- [10] C. K. Sinclair, E. L. Garwin, R. H. Miller, and C. Y. Prescott. "*A high intensity polarized electron source for the Stanford Linear Accelerator,*" AIP Conference Proceedings 35, 424 (1976).
- [11] J. Grames, "Unique electron polarimeter comparison and spin-based energy measurement," PACS2001. Proceedings of the 2001 Particle Accelerator Conference (Cat. No.01CH37268), Chicago, IL, USA, 2001, pp. 2392-2394 vol.3, doi: 10.1109/PAC.2001.987392.
- [12] V. Tioukine, K. Aulenbacher. "*Operation of the MAMI accelerator with a Wien filter based spin rotation system,*" Nuclear Instruments and Methods in Physics Research A 568 (2006).
- [13] V. Bargmann, Louis Michel, and V. L. Telegdi. "*Precession of the Polarization of Particles Moving in a Homogeneous Electromagnetic Field,*" Phys. Rev. Lett. 2, 435, 1959.
- [14] Fowler Ralph Howard and Nordheim L. "*Electron emission in intense electric fields,*" Proc. R. Soc. Lond. A 119: 173–181, 1928.
- [15] K. Aulenbacher, Ch. Nachtigall, H. G. Andresen, J. Bermuth, Th. Dombo, P. Drescher, H. Euteneuer, H. Fischer, D. v. Harrach, P. Hartmann, J. Hoffmann, P. Jennewein, K. H. Kaiser, S. Köbis, H. J. Kreidel, J. Langbein, M. Petri, S. Plützer, E. Reichert, M. Schemies, H. - JSchöpe, K. -H. Steffens, M. Steigerwald, H. Trautner, Th. Weis, "*The MAMI source of polarized electrons,*" Nucl. Instrum. Methods. A 391, 498 (1997).
- [16] C. Hernandez-Garcia, M. Poelker, and J. Hansknecht, "*High voltage studies of inverted-geometry ceramic insulators for a 350 kV dc polarized electron gun,*" IEEE, Trans. Diel. Elec. Insul., vol. 23, no. 1, 418 (2016).
- [17] J. E. Clendenin, A. Brachmann, K. Ioakeimidi, R. E. Kirby, T. Maruyama, R. H. Miller, J. W. Wang, and F. Zhou. "*Low Emittance Guns for the ILC Polarized Electron Beam,*" AIP Conference Proceedings 915, 1067 (2007).
- [18] John Skaritka, Erdong Wang, Ferdinand Willeke, Robert Lambiase, Wei Lui, Vadim Ptitsyn, Omer Rahman. "*Conceptual design of a Polarized Electron Ion Collider at Brookhaven National Laboratory,*" Proceedings, 17th International Workshop on Polarized Sources, Targets, and Polarimetry (PSTP2017).
- [19] M. Salomaa, H.A. Enge. "*Velocity selector for heavy-ion separation,*" Nuclear Instruments and Methods, Volume 145, Issue 2, 1977, Pages 279-282, ISSN 0029-554X.

- [20] J. M. Grames, C. K. Sinclair, J. Mitchell, E. Chudakov, H. Fenker, A. Freyberger, D. W. Higinbotham, M. Poelker, M. Steigerwald, M. Tiefenback, C. Cavata, S. Escoffier, F. Marie, T. Pussieux, P. Vernin, S. Danagoulian, V. Dharmawardane, R. Fatemi, K. Joo, M. Zeier, V. Gorbenko, R. Nasseripour, B. Raue, R. Suleiman, and B. Zihlmann. “*Unique electron polarimeter analyzing power comparison and precision spin-based energy measurement*,” Phys. Rev. ST Accel. Beams 7, 042802 – Published 19 April 2004.
- [21] MOLLER Collaboration. arXiv:1411.4088 [nucl-ex], (2014).
https://moller.jlab.org/moller_root/
- [22] Solidworks <https://www.solidworks.com>
- [23] H. Miller, “*Surface flashover of insulators*,” IEEE Transactions on Electrical Insulation, vol. 24, no. 5, 765 (1989).
- [24] CST Studio Suite, “CST Microwave Studio,” 2019. <http://www.cst.com>
- [25] Pulsar Physics General Particle Tracer <http://www.pulsar.nl/gpt>
- [26] G. Palacios-Serrano, F. Hannon, C. Hernandez-Garcia, M. Poelker, and H. Baumgart. “Electrostatic design and conditioning of a triple point junction shield for a -200 kV DC high voltage photogun,” Review of Scientific Instruments 89, 104703 (2018); doi: 10.1063/1.5048700.
- [27] C. Hernandez-Garcia, D. Bullard, F. Hannon, Y. Wang, and M. Poelker. “*High voltage performance of a dc photoemission electron gun with centrifugal barrel-polished electrodes*,” Review of Scientific Instruments 88, 093303 (2017).
- [28] Experimental Physics and Industrial Control System. Argonne National Laboratory. <https://epics.anl.gov/license/index.php> retrieved November 2020.
- [29] Marcy L. Stutzman, Philip A. Adderley, Md Abdullah A. Mamun, and Matt Poelker, “*Nonevaporable getter coating chambers for extreme high vacuum*,” Journal of Vacuum Science and Technology A: Vacuum, Surfaces, and Films, 36 (2018).
- [30] K. Halbach, Lawrence Livermore National Laboratory Technical Report No. UCRL-17436, 1967.
- [31] Opera Electromagnetic and Electromechanical Simulation.
<http://www.operafea.com/>
- [32] H. C. Miller, “*The effect of doping on the voltage holdoff performance of alumina insulators in vacuum*,” IEEE Trans. Electr. Insul. Vol. 20 No. 3, 505 (1985).

- [33] M. BastaniNejad, A. A. Elmustafa, E. Forman, J. Clark, S. Covert, J. Grames, J. Hansknecht, C. Hernandez-Garcia, M. Poelker, R. Suleiman, “*Improving the Performance of Stainless-Steel DC High Voltage Photoelectron Gun Cathode Electrodes via Gas Conditioning with Helium or Krypton*”, Nuclear Instruments and Methods in Physics Research A 762 135 (2014).
- [34] Martin Reiser, “*Theory and Design of Charged Particle Beams*”. WILEY-VCH Verlag GmbH & Co. KGaA, Weinheim (2008); ISBN:978-3-527-4074
- [35] J. R. Pierce, “*Rectilinear Electron Flow in Beams*”, Journal of Applied Physics 11, 548 (1940); <https://doi.org/10.1063/1.1712815>
- [36] A. Harrison, “*A computer study of uniform-field electrode*”, Br. J. Appl. Phys. 18 1617 (1967).
- [37] W. B. Herrmannsfeldt, “*EGUN: An electron optics and gun design program*”, United States: N. p., 1988. Web. doi:10.2172/6711732.
- [38] W. B. Herrmannsfeldt, “*Developments in electron gun simulation*”, Physica Scripta, Volume 71, Issue , pp. 28-33 (1997).
- [39] W. Anders, I. Bazarov, L. Cultrera, D. Dimitrov, D. H. Dowell, B. Dunham, J. W. Lewellen, A. Nuewmann, M. Poelker, T. Rao, S. Schreiber, J. Smedley and T. Tsang, edited by T. Rao and D. H. Dowell, “*An engineering guide to photoinjectors*”, Ch 8. (2013). ISBN-13, 978-1481943222
- [40] B. M. Lewis, H. T. Tran, M. E. Read and R. L. Ives, “*Design of an electron gun using computer optimization*”, IEEE Transactions on Plasma Science, vol. 32, no. 3, pp. 1242-1250, (2004). doi: 10.1109/TPS.2004.827572
- [41] Förster, P., Schöps, S., Enders, J., Herbert, M., & Simona, A., “*Freeform shape optimization of a compact DC photo-electron gun using isogeometric analysis*”, (2020). ArXiv, abs/2012.04372.

APPENDIX A
MODEL EQUATIONS

A. 1 Electrostatics

In order to describe our problem, we use the widely established macroscopic Maxwell's electromagnetic field equations:

$\nabla \cdot \mathbf{E} = \frac{\rho}{\epsilon}$	$\nabla \times \mathbf{E} = -\frac{\partial \mathbf{B}}{\partial t}$
$\nabla \cdot \mathbf{B} = 0$	$\nabla \times \mathbf{B} = \mu \mathbf{j}_f + \mu\epsilon \frac{\partial \mathbf{E}}{\partial t}$

For the electrostatics problem, the absence of a magnetic field, and the time-independent electric field yield:

$\nabla \cdot \mathbf{E} = \frac{\rho}{\epsilon}$	$\nabla \times \mathbf{E} = 0$
---	--------------------------------

Additionally, we know that the electric field generated by a charge distribution located at \mathbf{r}' and measured at \mathbf{r} is given by Coulomb's law:

$$\mathbf{E}(\mathbf{r}) = -\nabla \frac{1}{4\pi\epsilon_0} \int d^3r' \frac{\rho(\mathbf{r}')}{|\mathbf{r} - \mathbf{r}'|}$$

where one can define:

$$\varphi(\mathbf{r}) = \frac{1}{4\pi\epsilon_0} \int d^3r' \frac{\rho(\mathbf{r}')}{|\mathbf{r} - \mathbf{r}'|}$$

Therefore, we can write the differential equation that associates both results:

$$\mathbf{E}(\mathbf{r}) = -\nabla\varphi(\mathbf{r}).$$

CST EM Studio relies on the finite element method (FEM) to solve the differential equation system resulting from this representation of Maxwell's field equations. Even though the specific information on the calculations is not publicly available, it is established [John A. Sokolowski & Catherine M. Banks] that in FEM the 3D models that represent the geometry of the device and its material properties are converted to a tetrahedral node and mesh representation. The differential equations in the physical model and node interactions are then solved through an iterative process. Therefore, it is relevant to note that the characteristics of our electrostatics problem place it in the boundary value category; thus, the additional boundary equations are relevant for obtaining the solution:

$\hat{\mathbf{n}} \cdot (\mathbf{E}_1 - \mathbf{E}_2) = \frac{\sigma(\mathbf{r}_s)}{\epsilon}$	$\hat{\mathbf{n}} \times (\mathbf{E}_1 - \mathbf{E}_2) = 0$
--	---

where $\hat{\mathbf{n}}$ is the normal vector pointing out of the boundary surface and $\mathbf{E}_1, \mathbf{E}_2$ are the electric fields at two opposite sides divided by the boundary.

A. 2 Particle tracking

As established by the theoretical framework of relativistic dynamics, the equations of motion for a particle of charge q in the presence of electromagnetic fields are described by the Lorentz equation:

$$\mathbf{F} = q(\mathbf{E}(z) + \mathbf{v}(z, t) \times \mathbf{B}(z))$$

where the force is expressed as the total time derivative $\mathbf{F} = \frac{d\mathbf{p}}{dt}$ of the relativistic momentum $\mathbf{p} = m_e \gamma \mathbf{v}(z, t)$ and $\gamma = \frac{1}{\sqrt{1 - \frac{v^2}{c^2}}}$ is the Lorentz factor. Therefore, the system

of ordinary differential equations to solve in an explicit form (dropping the z and t dependences to simplify notation) are:

$$m_e \frac{d}{dt}(\gamma \mathbf{v}_x) = q(E_x + (B_z \mathbf{v}_y - B_y \mathbf{v}_z)),$$

$$m_e \frac{d}{dt}(\gamma \mathbf{v}_y) = q(-E_y - (B_z \mathbf{v}_x - B_x \mathbf{v}_z)),$$

$$m_e \frac{d}{dt}(\gamma \mathbf{v}_z) = q(E_z + (B_y \mathbf{v}_x - B_x \mathbf{v}_y)).$$

An additional complication arises since the equation of motion cannot be solved for each individual particle by itself due to Coulomb type interactions between particles. All of these characteristics make our problem a perfect candidate to apply our knowledge of mathematical methods. Even better, the routines are available to us through the well-established Global Particle Tracer (GPT) software that recurs to solve a version of the equation of motion that couples all macro-particle coordinates as a function of time. In order to solve the resulting equation of motion, a 5-th order Runge-Kutta method is implemented [25].

In Runge- Kutta methods for solving ODEs with initial values, the solution is approximated by introducing k_i intermediate steps where the derivative is evaluated for every full time step Δt iteration, so the solution can be written as:

$$y(t + \Delta t) = y(t) + \sum_{i=1}^6 c_i k_i + O(\Delta t^6)$$

where $k_i = \Delta t f(t + a_i \Delta t, y + \Delta t \sum_{j=1}^{i-1} b_{ij} k_j)$ and the coefficients can be obtained from a Butcher tableau and are readily described in [25].

A. 3 Emittance

A particularly relevant beam dynamics parameter for our experiment is the normalized beam emittance, which is a measure of the volume in 3-dimensional phase space of the electron bunch that comprises the beam and thus is a good measure for the dispersion of the particles [Buon 1993]. This is an important characteristic for us since to maintain good beam quality one should keep the phase space dilution to a minimum. In our experiment, the presence of a Pierce type accelerating structure at the tip of the cathode electrode and the asymmetrical nature of the electromagnetic fields require us to closely monitor the changes in emittance related to the changes we propose in both the electron source and the Wien filter. We use the energy normalized emittance because it remains constant unless dissipative processes exist [Wiedeman 2015].

In our simulations the electromagnetic fields are generated in 3-dimensional space as files that contain position coordinates and the corresponding values of the fields, so our powerful GPT set of codes presents again a perfect choice. For theoretical calculations, the emittance derivation from Hill's equations is most useful; however, GPT handles beam dynamics through position and momentum coordinates, so the statistical definition, also known as the root mean square (rms) emittance for each transverse coordinate is used [Buon 1993]:

$$\epsilon_x = \gamma \sqrt{\langle x^2 \rangle \langle x'^2 \rangle - \langle x x' \rangle^2},$$

$$\epsilon_y = \gamma \sqrt{\langle y^2 \rangle \langle y'^2 \rangle - \langle y y' \rangle^2}$$

where GPT handles the expectation values as averages weighted by the number of elementary particles each macro-particle represents [25].

A. 4 Electron spin rotation in Wien filter electromagnetic field

The characteristic energy of our experiment requires the use of special relativity to treat the motion of charged particles in an electromagnetic field. It has been established that a particle with charge q , mass m , and quantum spin \mathbf{s} present an intrinsic magnetic moment $\mu = \frac{ge}{2mc} \mathbf{s}$. The Thomas-Bargmann-Michel-Telegdi (BMT) equation provides a widely implemented framework for analyzing the electron beam dynamics of such particles in the Wien filter [4], [11], [12], where independently generated homogeneous electromagnetic fields preserve the trajectory of the particles traveling longitudinally across the device ($\mathbf{v} = v_z \hat{\mathbf{z}}$) and rotate the spin angular moment. The change of the angle between the spin vector and the direction of motion in the particle rest frame in terms of the external electric and magnetic fields is given by [Jackson 1975]:

$$\frac{d\theta}{dt} = \frac{e}{mc} \left[a(\hat{\mathbf{n}} \times \hat{\boldsymbol{\beta}}) \cdot \mathbf{B} + \left(\frac{(1+a)\beta^2 - 1}{\beta} \right) \hat{\mathbf{n}} \cdot \frac{\mathbf{E}}{c} \right]$$

where $\hat{\mathbf{n}}$ is perpendicular to β , $a = \frac{g-2}{2} = 1.159652 \times 10^{-3}$ is the electron magnetic moment anomaly, g is the electron gyromagnetic factor, and β the velocity normalized to the speed of light. For our case, the electromagnetic fields are orthogonal to each other and to the particle momentum, and the trajectory preservation requires:

$$\mathbf{F} = q(\mathbf{E} + \mathbf{v} \times \mathbf{B}) = 0,$$

Therefore, with $\mathbf{E} = E_y \hat{\mathbf{y}}$ and $\mathbf{B} = -B_x \hat{\mathbf{x}}$ we get the (Wien) equilibrium condition

$\frac{E_y}{B_x} = v_z$. Moreover, our configuration reduces the change in spin vector angle to a form that

elucidates that for the energies in our experiment it is the electric field contribution in the particle rest frame that dominates the change in spin angle [11]:

$$\frac{d\theta}{dt} = \frac{e}{mc} \left[-aB_x + \left(\frac{(1+a)\beta^2 - 1}{\beta} \right) E_y \right]$$

Additionally, if we further simplify this equation using the approximation that for electrons $g \simeq 2 \rightarrow a \ll 1$, we can integrate to obtain an expression that allows us to find the magnitudes E_y and B_x :

$$\theta = \frac{eL}{mc\beta\gamma^2} \left[\frac{E_y}{v_z} \right] = \frac{eL}{mc\beta\gamma^2} B_x$$

where $\gamma = \frac{1}{\sqrt{1-\beta^2}}$ is the relativistic correction, and the characteristic lengths are assumed equal:

$$L_{effE} = \frac{\int_0^L E(0,0,z) dz}{E_{max}}, L_{effB} = \frac{\int_0^L B(0,0,z) dz}{B_{max}}.$$

A. 5 Field emission

In all of our experiments, cold metallic surfaces are subjected to high electric fields in vacuum. It has been widely established [7] that these conditions may result in an undesired emission of electrons that can lead to equipment damage or in the worst case, catastrophic failure. Given the characteristics of our experiments, we focus our attention on three main precursors of the phenomena:

By means of the quantum mechanical formalism, the resultant current density produced by the emission of electrons described as a Fermi-Dirac distribution, in the presence of a high electric field is given by:

$$J = A \frac{E^2}{\phi} e \left(-B \frac{\phi^{3/2}}{E} \right)$$

where $A = \frac{q}{16\pi h t_y^2}$ and $B = \frac{4\sqrt{2m}}{3h} v_y$ vary with h_y and v_y as functions of the potential barrier geometry¹.

For this document, the relevance is on the effect of the electric field, which results in a lowering of the potential barrier, thus creating a triangular potential that allows electrons with a momentum perpendicular to the metal surface to be emitted towards vacuum via quantum tunneling.

The previously described formalism is relevant when dealing with smooth surfaces, namely with a homogeneous topology, but the manufacturing processes of our devices introduce inhomogeneities. Thus, it is important to notice that the irregularities on the surface might create sharp protrusions at a small scale, where the electric field is given by [7] $E = \frac{V}{kr}$. This is relevant since the field on the sharp tips is enhanced by the geometry, giving place to more field emission or even explosive emission events which in turn releases material that can be further ionized, worsening the vacuum conditions by creating an avalanche effect.

It is worth noticing that the surface work-function can be modified by the adsorption of species found in the vacuum chamber (CO, CO₂) or by desorption of gas in the anode. Nevertheless, the strict measures taken for the preparation of electron gun surfaces (discussed in the following sections) place this secondary issues beyond the scope of this work.

¹ To a good approximation. K. Jensen (2018) provides a rigorous derivation of Fowler-Nordheim's equation for metals.

APPENDIX B

PERMISSION TO USE FIGURES

This appendix is for obtained permissions to use figures of other studies.

RightsLink Printable License

<https://s100.copyright.com/App/PrintableLicenseFrame.jsp?publisherID...>

ELSEVIER LICENSE TERMS AND CONDITIONS

Jan 28, 2021

This Agreement between Mr. Gabriel Palacios Serrano ("You") and Elsevier ("Elsevier") consists of your license details and the terms and conditions provided by Elsevier and Copyright Clearance Center.

License Number	4997970569485
License date	Jan 28, 2021
Licensed Content Publisher	Elsevier
Licensed Content Publication	Nuclear Instruments and Methods
Licensed Content Title	A source of highly polarized electrons at the stanford linear accelerator center
Licensed Content Author	M.J. Alguard, J.E. Clendenin, R.D. Ehrlich, V.W. Hughes, J.S. Ladish, M.S. Lubell, K.P. Schüler, G. Baum, W. Raith, R.H. Miller, W. Lysenko
Licensed Content Date	Jul 1, 1979
Licensed Content Volume	163
Licensed Content Issue	1
Licensed Content Pages	31
Start Page	29

End Page	59
Type of Use	reuse in a thesis/dissertation
Portion	figures/tables/illustrations
Number of figures/tables /illustrations	1
Format	both print and electronic
Are you the author of this Elsevier article?	No
Will you be translating?	No
Title	ELECTROSTATIC DESIGN AND CHARACTERIZATION OF A 200 keV PHOTOGUN AND WIEN SPIN ROTATOR
Institution name	Old Dominion University
Expected presentation date	Mar 2021
Portions	Figure 1
Requestor Location	Mr. Gabriel Palacios Serrano 1512 Hampton blvd. Apt 4. NORFOLK, VA 23517 United States Attn: Mr. Gabriel Palacios
Publisher Tax ID	98-0397604
Total	0.00 USD

AIP PUBLISHING LICENSE
TERMS AND CONDITIONS

Jan 28, 2021

This Agreement between Mr. Gabriel Palacios Serrano ("You") and AIP Publishing ("AIP Publishing") consists of your license details and the terms and conditions provided by AIP Publishing and Copyright Clearance Center.

License Number 4997970937019

License date Jan 28, 2021

Licensed Content
Publisher AIP PublishingLicensed Content
Publication AIP Conference ProceedingsLicensed Content Title A high intensity polarized electron source for the stanford linear
acceleratorLicensed Content
Author C. K. Sinclair, E. L. Garwin, R. H. Miller, et al

Licensed Content Date Dec 1, 1976

Licensed Content
Volume 35

Licensed Content Issue 1

Format	Print and electronic
Portion	Figure/Table
Number of figures/tables	1
Title	ELECTROSTATIC DESIGN AND CHARACTERIZATION OF A 200 keV PHOTOGUN AND WIEN SPIN ROTATOR
Institution name	Old Dominion University
Expected presentation date	Mar 2021
Portions	Figure 4
Requestor Location	Mr. Gabriel Palacios Serrano 1512 Hampton blvd. Apt 4. NORFOLK, VA 23517 United States Attn: Mr. Gabriel Palacios
Total	0.00 USD

ELSEVIER LICENSE
TERMS AND CONDITIONS

Jan 28, 2021

This Agreement between Mr. Gabriel Palacios Serrano ("You") and Elsevier ("Elsevier") consists of your license details and the terms and conditions provided by Elsevier and Copyright Clearance Center.

License Number 4997971225036

License date Jan 28, 2021

Licensed Content
Publisher Elsevier

Licensed Content
Publication Nuclear Instruments and Methods in Physics Research Section A:
Accelerators, Spectrometers, Detectors and Associated Equipment

Licensed Content Title The bates polarized electron source

Licensed Content
Author G.D. Cates, V.W. Hughes, R. Michaels, H.R. Schaefer, T.J. Gay, M.S. Lubell, R. Wilson, G.W. Dodson, K.A. Dow, S.B. Kowalski, K. Isakovich, K.S. Kumar, M.E. Schulze, P.A. Souder, D.H. Kim

Licensed Content Date Jun 1, 1989

Licensed Content
Volume 278

Licensed Content
Issue 2

RightsLink Printable License

<https://s100.copyright.com/App/PrintableLicenseFrame.jsp?publisherID...>

Start Page	293
End Page	317
Type of Use	reuse in a thesis/dissertation
Portion	figures/tables/illustrations
Number of figures/tables/illustrations	1
Format	both print and electronic
Are you the author of this Elsevier article?	No
Will you be translating?	No
Title	ELECTROSTATIC DESIGN AND CHARACTERIZATION OF A 200 keV PHOTOGUN AND WIEN SPIN ROTATOR
Institution name	Old Dominion University
Expected presentation date	Mar 2021
Portions	Figure 6
Requestor Location	Mr. Gabriel Palacios Serrano 1512 Hampton blvd. Apt 4. NORFOLK, VA 23517 United States Attn: Mr. Gabriel Palacios

RightsLink Printable License

<https://s100.copyright.com/App/PrintableLicenseFrame.jsp?publisherID...>

Publisher Tax ID	98-0397604
Total	0.00 USD

ELSEVIER LICENSE
TERMS AND CONDITIONS

Jan 28, 2021

This Agreement between Mr. Gabriel Palacios Serrano ("You") and Elsevier ("Elsevier") consists of your license details and the terms and conditions provided by Elsevier and Copyright Clearance Center.

License Number	4997971429124
License date	Jan 28, 2021
Licensed Content Publisher	Elsevier
Licensed Content Publication	Nuclear Instruments and Methods in Physics Research Section A: Accelerators, Spectrometers, Detectors and Associated Equipment
Licensed Content Title	A source of polarized electrons based on photoemission of GaAsP
Licensed Content Author	W. Hartmann,D. Conrath,W. Gasteyer,H.J. Gessinger,W. Heil,H. Kessler,L. Koch,E. Reichert,H.G. Andresen,T. Kettner,B. Wagner,J. Ahrens,J. Jethwa,F.P. Schäfer
Licensed Content Date	Jan 1, 1990
Licensed Content Volume	286
Licensed Content Issue	1-2
Licensed Content Pages	8
Start Page	1

RightsLink Printable License		https://s100.copyright.com/App/PrintableLicenseFrame.jsp?publisherID...
End Page	8	
Type of Use	reuse in a thesis/dissertation	
Portion	figures/tables/illustrations	
Number of figures/tables/illustrations	1	
Format	both print and electronic	
Are you the author of this Elsevier article?	No	
Will you be translating?	No	
Title	ELECTROSTATIC DESIGN AND CHARACTERIZATION OF A 200 keV PHOTOGUN AND WIEN SPIN ROTATOR	
Institution name	Old Dominion University	
Expected presentation date	Mar 2021	
Portions	Figure 2	
Requestor Location	Mr. Gabriel Palacios Serrano 1512 Hampton blvd. Apt 4. NORFOLK, VA 23517 United States Attn: Mr. Gabriel Palacios	
Publisher Tax ID	98-0397604	
RightsLink Printable License		https://s100.copyright.com/App/PrintableLicenseFrame.jsp?publisherID...
Total	0.00 USD	

ELSEVIER LICENSE
TERMS AND CONDITIONS

Jan 28, 2021

This Agreement between Mr. Gabriel Palacios Serrano ("You") and Elsevier ("Elsevier") consists of your license details and the terms and conditions provided by Elsevier and Copyright Clearance Center.

License Number	4997980612617
License date	Jan 28, 2021
Licensed Content Publisher	Elsevier
Licensed Content Publication	Nuclear Instruments and Methods in Physics Research Section A: Accelerators, Spectrometers, Detectors and Associated Equipment
Licensed Content Title	Operation of the MAMI accelerator with a Wien filter based spin rotation system
Licensed Content Author	V. Tioukine, K. Aulenbacher
Licensed Content Date	Dec 1, 2006
Licensed Content Volume	568
Licensed Content Issue	2
Licensed Content Pages	6
Start Page	537

End Page	542
Type of Use	reuse in a thesis/dissertation
Portion	figures/tables/illustrations
Number of figures/tables /illustrations	1
Format	both print and electronic
Are you the author of this Elsevier article?	No
Will you be translating?	No
Title	ELECTROSTATIC DESIGN AND CHARACTERIZATION OF A 200 keV PHOTOGUN AND WIEN SPIN ROTATOR
Institution name	Old Dominion University
Expected presentation date	Mar 2021
Portions	Figure 1
Requestor Location	Mr. Gabriel Palacios Serrano 1512 Hampton blvd. Apt 4. NORFOLK, VA 23517 United States Attn: Mr. Gabriel Palacios
Publisher Tax ID	98-0397604
Total	0.00 USD

VITA

Gabriel G. Palacios Serrano
 Department of Electrical & Computer Engineering
 Old Dominion University
 Norfolk, VA 23529

Education

- PhD in Electrical and Computer Engineering. May 2021. *Old Dominion University*, Norfolk, VA.
- MS in Physics. May 2017. *Old Dominion University*, Norfolk, VA.
- BS in Engineering Physics. August 2014. *Universidad Autónoma Metropolitana*, Azcapotzalco, México.

Publications

- REFEREED JOURNAL PUBLICATIONS
 1. (Pending submission) G. Palacios, P. Adderley, H. Baumgart, J. Benesch, D. Bullard, J. Grames, C. Hernandez-Garcia, A. Hofler, D. Machie, M. Poelker, M. Stutzman and R. Suleiman. “**A 200 keV Wien filter for the CEBAF 12 GeV upgrade**”. (2021)
 2. C. Hernandez-Garcia, P. Adderley, B. Bullard, J. Benesch, J. Grames, J. Gubeli, F. Hannon, J. Hansknecht, J. Jordan, R. Kazimi, G. A. Krafft, M. A. Mamun, M. Poelker, M. L. Stutzman, R. Suleiman, M. Tiefenback, Y. Wang, S. Zhang, H. Baumgart, G. Palacios-Serrano, S. Wijethunga, J. Yoskowitz, C. A. Valerio Lizarraga, R. Montoya Soto, and A. Canales Ramos. “**Compact –300 kV dc inverted insulator photogun with biased anode and alkali-antimonide photocathode**”. *Physical Review Accelerators and Beams* 22,113401 (2019). <https://doi.org/10.1103/PhysRevAccelBeams.22.113401>
 3. G. Palacios-Serrano, F. Hannon, C. Hernandez-Garcia, M. Poelker, and H. Baumgart. “**Electrostatic design and conditioning of a triple point junction shield for a –200 kV DC high voltage photogun**” *Review of Scientific Instruments* 89, 104703 (2018). <https://doi.org/10.1063/1.5048700>.
 4. A. Robledo, A. Garcia-Villareal, G. Palacios, A. Vera, H. Sobral. “**Characteristics of the discharge of a charged dielectric in low-pressure air**”. *Journal of Electrostatics*, Volume 76, Pages 152–158. (2015). <http://dx.doi.org/10.1016/j.elstat.2015.05.021>
- Three refereed international conference proceedings, two Jefferson Lab technical reports, two books, and ten presentations at international conferences and universities.